82p

N63-10336

CODE 1

NASA TN D-1439

NASA TN D-1439

TECHNICAL NOTE

D-1439

CAVITATION AND NONCAVITATION PERFORMANCE OF

AN 80.6° FLAT-PLATE HELICAL INDUCER

AT THREE ROTATIONAL SPEEDS

By Donald M. Sandercock, Richard F. Soltis,
and Douglas A. Anderson

Lewis Research Center
Cleveland, Ohio

NATIONAL AERONAUTICS AND SPACE ADMINISTRATION

WASHINGTON November 1962

NATIONAL AERONAUTICS AND SPACE ADMINISTRATION

TECHNICAL NOTE D-1439

CAVITATION AND NONCAVITATION PERFORMANCE OF AN 80.6° FLAT-PLATE HELICAL INDUCER AT THREE ROTATIONAL SPEEDS

By Donald M. Sandercock, Richard F. Soltis,
and Douglas A. Anderson

10336

SUMMARY

A flat-plate helical inducer with a tip helix angle of 80.6° was operated at three rotor speeds in water in order to obtain the performance of this type of inducer and to observe any scale effects associated with a change in speed. The test rotor had three blades, a tip diameter of 5 inches, and a hub-tip radius ratio of 0.5. Both hub and tip radii were held constant across the rotor. Similar inlet flow conditions were maintained at the three different speeds by operating at constant values of normalized net positive suction head.

The performance results are presented as overall performance and as radial distributions of both flow conditions (at rotor inlet and outlet) and selected blade-element performance parameters. In addition to indicating performance levels, the radial distributions describe the type of flow patterns occurring across the rotor and show the radial variations of flow conditions a succeeding blade row, or pump, would have to accept over a range of operating conditions. To supplement the measured performance results, photographs of the flow at various operating conditions are presented. The applicability of the simple radial equilibrium condition to flow conditions at the rotor exit is investigated. For noncavitating operation, changes in speed did not measurably affect the head-coefficient - flow-coefficient characteristic curve, but did affect the efficiency. Under cavitating conditions, both the head-rise coefficient and efficiency changed as speed varied.

INTRODUCTION

The use of the cavitating inducer to realize the advantages of high-suction-speed pumps has found wide acceptance for liquid-rocket-engine application. Reference 1 notes some of the advantages of utilizing the cavitating inducer, while reference 2 points out some of the

problems encountered in gaining an understanding of both the hydrodynamic and thermodynamic effects on the flow across such an impeller when pumping the fluids utilized in actual space-vehicle applications.

One type of inducer under study at the Lewis Research Center is the flat-plate helix. It is simple to fabricate and has proven its ability to pump fluids under cavitating conditions. Reference 3 presents the measured performance of a flat-plate helical inducer with a 78° helix angle at the tip. A small portion of the data obtained in this latter investigation (ref. 3) indicated that the dropoff in performance due to cavitation effects varied with blade speed; however, since both speed and cavitation number were varied, it was not possible to separate the individual effects. Other investigators have reported similar findings (see ref. 4).

This report exhibits the performance characteristics of a flat-plate inducer with an 80.6° helix angle at the tip. In this investigation the question of speed effects was further pursued by operating the inducer over a speed range of 2 to 1 under both cavitating and noncavitating conditions. Thus, the results shown herein serve the dual purpose of

(1) Presenting the performance of a helical inducer with a tip helix angle of 80.6°

(2) Providing an example of scale effects caused by a variation in speed for a limited range of blade speed and/or Reynolds number

The data are presented in the form of overall performance and as radial distributions of flow conditions and selected blade-element performance parameters. Performance plots are arranged to emphasize the effects of speed on the measured performance. The agreement between the radial distributions of measured axial velocities and those calculated by assuming the existence of simple radial equilibrium, as defined by

$$\frac{\partial h}{\partial r} = \frac{V_{\theta}^{2}}{gr} \tag{1}$$

is investigated for various modes of operation. (Symbols are defined in appendix A.)

APPARATUS AND PROCEDURE

Test Rotor

The test rotor used in this investigation was a flat-plate helix with a tip angle (i.e., the angle between the blade mean line and the axial direction) of 80.6°. The impeller had a tip diameter of 4.956 inches and a hub- to tip-diameter ratio of 0.5, both of which were maintained constant across the rotor. The three blades had constant thickness from inlet to outlet along a constant-radius helical path and a linear variation of thickness radially from 0.10 inch at the tip to 0.15 inch at the hub. The tangential spacing of the three blades combined with the given axial depth (i.e., the chord length) to give a solidity at the tip of 2.361. Significant geometric features of this rotor are listed in table I. The rotor was machined from the 400 series stainless steel. Both leading and trailing edges were sharpened to a wedge shape symmetrical about the blade centerline. A photograph of the rotor is shown in figure 1.

Test Facility

This investigation was conducted in the Lewis water tunnel, a closed-loop-pump test facility. It is the same system as described in reference 3; consequently, a detailed description will not be repeated herein. A schematic diagram of the test setup is shown in figure 2(a) and a photograph of the facility in figure 2(b).

Instrumentation and Procedure

The detailed rotor performance was obtained from radial surveys of flow conditions approximately 1 inch upstream of the rotor leading edge and 1 inch downstream of the rotor trailing edge. Both the test procedure and the instrumentation (including cameras) are the same as those used and discussed in reference 3. Photographs of the total-pressure claw probe (measures total pressure and angle) and the static-pressure wedge probe (measures static pressure and angle) are shown in figure 3. The estimated maximum measurement errors due to instrumentation were:

Inlet total pressure, P_1, lb/sq in.	±0.25
Inlet dynamic velocity head, $P_1 - p_1$, lb/sq in.	±0.25
Head rise across the inducer, ΔP, lb/sq in.	±1.75
Outlet dynamic velocity head, $P_2 - p_2$, lb/sq in.	±0.25
Angle, deg	±0.50
Rotor speed, percent	±0.10
Venturi flow, percent	±1.0

All test operations were conducted at a constant water temperature of approximately 80° F and an air content of less than 3 parts per million by weight.

Calculations

The equations used to calculate both the inducer overall and blade-element performance are presented in appendix B.

In the calculation of inlet flow angle an error in the zero angle of the inlet total-pressure claw probe was discovered; consequently, the inlet angles presented are those obtained from the static wedge probe. In general, the static wedge probe is not as sensitive as the claw probe to changes in flow angle, and its measured values are used for checking purposes. However, the inlet angles presented are believed to be within ±2° of true flow angles except for measurements taken in the vicinity of reverse flow regions where differences between angles measured by claw and static wedge as high as ±15° have been observed.

Some measure of the reliability of the data may be obtained from figure 4, which compares the integrated weight flows at the rotor inlet and outlet measuring stations with the flow measured by the Venturi meter. At the rotor inlet the integrated flows compare very favorably with the measured Venturi flows; the maximum difference was ±5 percent and the majority of the test points compared within ±2 percent. At the exit measuring station the comparison is not as favorable; figure 4 shows a maximum difference of ±15 percent, but most integrated values lie within ±7 percent of the measured Venturi values. The comparisons shown herein display approximately the same range of values as those obtained in an investigation of a 78° inducer and those reported in reference 3. Factors contributing in some degree to the difficulty of obtaining accurate flow measurements at the rotor outlet are advanced in reference 3.

Blade-Element Parameters

The presentation and analysis of data are based on the belief that the blade row overall performance can be described by a summation of the performance occurring across individual blade elements along the radius. The first requirement is the definition of a blade element. A blade element is defined as a portion of the blade that lies along a surface of revolution generated by a streamline. The definition is usually simplified by the assumption that the streamline occurs across the blade in a straight line. Furthermore, to alleviate complications in the data taking and computing procedures, this definition of a blade element is assumed to apply under all operating conditions. For simplicity, then, a

blade element as used herein is assumed to lie along a cylindrical surface. As mass flow shifts occur across the blade row, the assumed blade elements will deviate increased amounts from streamline flow.

The worth of an inducer is measured by the amount of fluid it can pass and the head it can develop under cavitating conditions. The primary performance parameters, then, would be head rise, flow, and some measure of the degree of cavitation at the various modes of operation. The efficiency of the flow process is generally secondary in importance.

Along a streamline (blade element) the head rise produced by the rotor depends upon the work input (ideal head rise) and the losses incurred in the flow around the blade. For an axial-flow rotor the energy input is obtained chiefly through a change in tangential velocity (see eq. (B2)), which is a function of the turning done on the fluid and the axial-velocity change (or outlet axial velocity for the case of no inlet whirl). Consequently, it is the combination of turning and axial velocity that results in a given value of ideal head rise. This point is stressed because streamline curvature downstream of the blade trailing edge resulting from mass-flow redistributions means that the velocity diagrams computed at the blade outlet measuring station will be different from those that exist at the blade trailing edge. Although along a true streamline the ideal head rise computed from either set of velocity diagrams would be the same, a different combination of turning angle and axial velocity would exist.

The fluid turning accomplished by the blade element is studied by means of incidence and deviation angles, defined by

$$i = \beta_1' - \gamma \tag{2}$$

and

$$\delta = \beta_2' - \gamma \tag{3}$$

Thus the turning angle $\Delta\beta'$ becomes

$$\Delta\beta' = \beta_1' - \beta_2' = i - \delta \tag{4}$$

The blade angle γ for a flat-plate helical blade may be obtained from

$$\tan \gamma = \frac{r}{r_t} \tan \gamma_t \tag{5}$$

The radial distribution of axial velocity must satisfy both radial equilibrium and continuity requirements. Some of the qualitative effects of

loss on the radial distribution of axial velocity may be seen from the theoretical results of reference 5.

As a measure of the blade loading the diffusion factor D, defined by equation (B10) and developed in reference 6, is used. This parameter is computed from inlet and outlet velocity diagrams and could have a varied meaning as the true streamlines deviate from the assumed blade elements. In order to establish similarity of the cavitating conditions on the blade, the cavitation number k (eq. (B9)) is employed. For a given blade shape, decreasing k values are associated with increased amounts of cavitation. To simplify the construction of outlet velocity diagrams, measured outlet flow angles are presented. These may be used in conjunction with the axial velocity (computed from the outlet flow coefficient) and blade speed to reconstruct the diagram. Accordingly, the following selected flow and element performance parameters have been presented for a variety of cavitating and noncavitating operating conditions:

(1) Head-rise coefficient, ψ

(2) Efficiency, η

(3) Ideal (no loss) head-rise coefficient, ψ_i

(4) Relative total-pressure loss coefficient, $\bar{\omega}$

(5) Flow coefficient, φ

(6) Deviation angle, δ, deg

(7) Cavitation number, k

(8) Outlet flow angle, β_2, deg

(9) Incidence angle, i, deg

RESULTS AND DISCUSSION

For expediency, the presentation and discussion of the noncavitating and cavitating performance is given in separate sections. Since the curves presented are, in general, self-explanatory, only the significant features are discussed. One of the principal methods of studying cavitation has been by means of visual observations and photographs. In order to aid the reader in visualizing the flows under discussion, photographs of the flow taken over a range of inlet conditions and speed are shown first.

Visual Studies

The sequences of photographs presented for comparison will follow the same pattern used in succeeding sections to present performance data; that is, the emphasis will be placed on comparing the flow at the different speeds under similar operating conditions - approximately the same flow coefficient and normalized net positive suction head (see eq. (B17)). Less attention is given to changes in performance as H_{sv} is lowered for a given value of speed and flow coefficient. The latter type of operation is covered more fully in reference 3, and the same stages of cavitation are generally encountered by all inducers of this type. In brief, as the inlet pressure (or H_{sv}) is lowered from some relatively high value at which no cavitation can be observed, several stages of cavitation are generally identified. These include:

(1) Cavitation inception

(2) Unsteady cavitation

(3) Cavitation breakdown

A discussion of cavitation conditions identifying each of these stages is given in reference 3.

For identification purposes in the discussion, a specific comparison will have a sequence number and/or figure number, while a particular photograph will be identified by means of the run number on the photograph. For orientation purposes, figure 5 presents a photograph of the rotor in which inlet flow direction and direction of rotation of the rotor are indicated. The rotor is seen by the camera from the same relative position from which flow conditions shown in succeeding figures were photographed.

Figure 6 presents photographs of the flow at three speeds and an $(H_{sv})_N$ of 160 feet. Figure 6(a) shows operation at a high flow, while figure 6(b) depicts flow conditions at a low flow. At both operating points cavitation along the blade surface and in the tip vortex are occurring. This then represents operation past the inception point (where visible bubbles first appear) but not yet at the unsteady region. No significant differences in type of cavitation with speed are noted for these operating conditions. In figure 6(b) the tip vortex cavitation appears slightly more dense and solid at the lowest speed (i.e., N = 7500 rpm), but these photographs were obtained at slightly different inlet flow geometries (i.e., flow coefficients) as indicated. Two observations made from these photographs are:

(1) The blade surface cavitation appears as a solid set of streamers or as a sheet, which hugs the blade surface. This is typical for operation in cold water.

(2) As the flow coefficient is decreased (hence the blade loading is increased), the tip vortex cavitation stands out an increasing distance into the inlet flow region.

Figure 7 shows the changes observed as the H_{SV} is lowered at a constant speed and approximately the same flow coefficient. At the high inlet pressure (i.e., H_{SV} = 160 ft) some blade surface and tip vortex cavitation occurs in the blade leading-edge region with the tip vortex cavitation extending some distance into the inlet flow region. At the lower H_{SV} operation (i.e., H_{SV} = 65 and 60 ft) both tip vortex and blade surface cavitation are heavy and extend a considerable distance into the blade passage. In both cases the cavitation was steady, and these two latter cases would be considered operating in the cavitation breakdown stage. At H_{SV} = 65 and 60 feet (runs 33 and 36, for instance), note that in the blade leading-edge region the tip vortex appears to flow along the blade tip (as in runs in fig. 6(a)) as compared to run 28, which indicates a shifting of blade loading rearward along the blade chord.

Figure 8 presents photographs of cavitation obtained at the three speeds for a constant $(H_{SV})_N$ and flow coefficients of approximately 0.1. A comparison in terms of flow coefficient shows that at the lower flow coefficient (i.e., at higher blade loading) the tip vortex cavitation seems to extend more nearly across the blade passages. A comparison in terms of speed indicates:

(1) At the two higher speeds (i.e., 15,000 and 11,250 rpm) there was no observable variation in the type of cavitation photographed.

(2) At the two higher speeds the tip vortex cavitation appears to be denser and to cover a greater portion of the blade passage width than was observed for the low-speed operation in a region midway between blade leading and trailing edges.

(3) At the low speed (i.e., 7500 rpm) the cavitation in the tip vortex extends a greater distance along the blade passage length from the blade leading edge than observed at either of the higher speeds.

In the photographs shown, the blade surface cavitation is often obscured by the tip vortex cavitation, especially in the middle and latter portions of the blade passage. Visual observations of cavitation indicate that, in general, the growth of the blade surface cavitation follows in some

relative fashion the growth of the more easily distinguished tip vortex cavitation.

Figure 9 compares cavitation as photographed at the three blade speeds for a normalized H_{sv} value of 60 feet and two flow coefficients. The discussion of figure 8 would appear to be equally applicable to figure 9. The principal difference between the two figures seems to be the increased denseness of the cavitation in the rear portions of the blade passage in figure 9 and the slight increase in the extent of blade passage at which cavitation appears. It is indicated in reference 3 that under certain operating conditions an unsteady type of cavitation is encountered. Under these conditions, the vapor formation appears to pulsate in a blade passage, or to occur in alternating blade passages. For a three-bladed impeller, this implies that the cavitation zone would move circumferentially around the rotor in a manner similar to rotating-stall zones observed in axial-flow compressors. This effect is observed primarily through vapor formation in the tip vortex. Test conditions covered to obtain the performance data presented herein did not include operation with unsteady cavitation; however, at a lower speed (e.g., 5500 rpm) this type of cavitation was photographed and is presented here for interest. Figure 10 shows a sequence of six photographs in which the same blade passage first contains cavitation and then is free of it in succeeding photographs. In this sequence each succeeding photograph shows the same blade passage approximately 4 revolutions later.

Noncavitating Performance

Performance described as noncavitating implies that the flow around the blades is free of cavitation. Experience has shown that such a flow could be attained only at very high inlet pressures, or H_{sv} values. As the inlet pressure is reduced, visible formation of vapor will usually appear first in the core of the vortex resulting from blade tip clearance flows and then in the accelerated flow region around the blade leading edge. However, no observable effect on the measured performance generally appears until the blade cavitation reaches some point along the blade in the vicinity of the leading edge of an adjacent blade.

In this investigation it was desirable to limit the inlet pressure to 160 feet at the high speed. Preliminary tests (at lower speeds) covering a range of inlet pressures showed that, at a normalized value of 160 feet, no observable decline in performance due to cavitation had occurred. For this reason, the latter conditions are presented herein as noncavitating performance even though the photographs obviously show both tip vortex and blade surface cavitation occurring at these conditions. The tip cavitation number at $N = 15,000$ rpm and $H_{sv} = 160$ feet is approximately 0.094. A check of the cavitation performance of flat-plate inducers reported in reference 7 also indicates that at $k = 0.09$

the impeller performance has not yet suffered any appreciable deterioration due to cavitation.

Overall performance. - Figure 11 presents the overall performance by showing head coefficient and efficiency as a function of flow coefficient. The values of both head coefficient and efficiency represent mass-averaged results, and data at all three speeds are included. The curve (fig. 11(b)) shows the nearly linear, inverse relation typical for this type of inducer. The range of flow covered was limited by flow losses around the test loop at the maximum flow and by excessive rig vibrations (for prolonged operation) at the minimum flow point. At present, no significance is attached to the fact that the minimum flow coefficient differed with speed, since no exact procedure was observed to set this operating condition. Over the range of flow and speed presented, the data indicate that similarity laws for predicting head rise and flow would operate satisfactorily.

The level of efficiency $\bar{\eta}$ attained at various flow coefficients $\bar{\varphi}$ shows differences with blade speed. At all operating conditions the highest efficiency was recorded at the highest speed; however, only in the high-flow-coefficient region is a consistent trend of efficiency with speed noted. Since all the fluid properties, blade geometry, clearances, and ranges of inlet flow geometry (flow coefficient) are the same for each speed, the Reynolds number would appear to be the basic parameter affecting the flow. In this investigation the range of Reynolds number (based on impeller tip speed and blade chord at the tip) varied from 1.85×10^7 to 3.70×10^7. These data then indicate that for this type of impeller and Reynolds number range the similarity laws relating power input could not be directly applied.

Reference 8, which reports the observed performance across a rotor with cambered circular arc blades, states that no measurable change in overall efficiency with speed was observed. The two operating speeds used represent a range of Reynolds number of 2 to 1 (i.e., $Re = 1.06\times10^6$ to 2.12×10^6). At these two speeds the head-rise coefficient also showed no effect of speed. Based on these two investigations, it would appear that an increase in Reynolds number for a given rotor would not affect the head-rise coefficient, and either would not affect the overall efficiency or would increase it.

Blade-element data. - The blade-element data are presented as radial distributions of selected blade-element performance parameters plus certain flow conditions at the blade inlet and outlet. Figure 12 shows the changes in distribution as the inlet flow coefficient is varied. The performance presented was obtained at the highest speed (viz., N = 15,000 rpm) and at three different flow coefficients covering the range of operation.

At the highest flow, the inlet flow coefficient (fig. 12(b)) shows a decreasing value from hub to tip. This distribution reflects the radial-pressure-gradient requirements imposed by the flow around the inlet hub fairing. At the mean flow coefficient the level of velocity decreases, but approximately the same gradient exists. During operation at the lowest flow coefficient the observed gradient of inlet flow coefficient increases. In reference 3 this tendency of pressure gradient to increase as inlet flow coefficient is lowered persisted until zero inlet axial velocities in the tip region (reverse flow regions) were measured. In reference 3 several probable sources of this disturbance to the inlet flow were advanced. The first of these is the action of the rotor vanes on the inlet meridional flow. As the inlet flow is decreased, the radial gradient of energy addition (increasing toward the tip) is also increased, and severe mass-flow redistributions across the rotor result. Thus there are steep gradients of flow coefficient at the blade outlet with zero values and possible reverse-flow areas indicated in the hub region, while the opposite type flow and gradients are noted at the inlet to the rotor. References 9 and 10 elaborate further on these effects. A second cause of disturbance in the tip region at the blade inlet might be derived from the tip vortex resulting from flow across the tip clearance of the blades. It can be seen from the series of photographs presented that cavitation occurring in this vortex extends increasing distances into the inlet flow region as the inlet flow coefficient is reduced (as blade loading is increased). A third source may lie in the three-dimensional flows taking place under these flow conditions. It has been estimated that the amount of blade boundary-layer fluid transported radially during the flow across an inducer-type blade may be many times that transported by the lower inlet angle and smaller chord blades typical of an axial-flow compressor rotor. A better understanding of this flow phenomenon may be necessary in order to explain this inlet radial flow distribution.

The amount of inlet whirl indicated by the inlet absolute flow angle (fig. 12(d)) is small ($\pm 3^{\circ}$) over the range of flow conditions covered in these curves. As noted earlier, in these tests the inlet flow angles were obtained from the static wedge probe, which does not have quite as good accuracy or response as the claw-type probe generally utilized.

The radial distribution of the head-rise coefficient (fig. 12(f)) is typical of that produced by the flat-plate helical inducer, that is, an increasing value of head rise from hub to tip and an increased gradient as flow coefficient is decreased. The ideal head-rise (energy input) distribution (fig. 12(h)) displays similar but exaggerated gradients compared to the measured head-rise variations. The reason for these gradients can be demonstrated by the construction of typical velocity diagrams at the hub and tip blade elements, which demonstrate the relative sensitivity of ideal head rise to a change in inlet flow coefficent.

The ideal head rise is affected by some combination of deviation angle (fluid turning) and outlet flow coefficient. Radial distributions

of deviation angle and outlet flow coefficient obtained at the blade exit measuring station are shown in figures 12(i) and (e), respectively. The radial variations of outlet flow coefficient demonstrate the changing requirements of radial equilibrium with inlet flow coefficient, which results in zero axial velocities (reverse flow areas) in the hub region at the blade outlet. Reference 7 reports similar results from visual observations of tufts mounted on the downstream hub casing and notes that separation of flow from the hub appears to begin approximately midway through the blade passage. The deviation angles, in general, decrease in value from hub to tip with negative values computed in the tip regions. Negative deviation angles imply fluid turning greater than that associated with perfect guidance by the blades. The data presented herein show that computed negative deviation angles are obtained at all rotor speeds, and similar results are reported in reference 3 for a 78° helical inducer. In all cases the measured flow conditions at the blade inlet and outlet implied significant mass-flow redistributions were taking place. In reference 3 a simple procedure for transferring the velocity diagram as computed at the blade outlet measuring station to the blade trailing edge along some assumed streamline was outlined. The results of the calculations indicated that very small shifts in streamline location in the blade tip region would result in positive deviation angles at the blade trailing edge.

The deviation-angle radial distributions, in general, follow the incidence-angle variations. Such a distribution might be anticipated from the deviation-angle rules, which show that deviation angle is primarily a function of camber angle, for instance, (from ref. 11)

$$\delta = m\,\Delta\gamma\sqrt{\frac{1}{\sigma}} \tag{6}$$

where m is some function of blade stagger angle. The flat-plate inducer, of course, has no camber, and all turning of the fluid is accomplished by incidence angle; this fact suggests the substitution of this parameter for camber in equation (6). Because the deviation angles were computed from measurements taken 1 inch downstream of the blade trailing edge, quantitative comparisons of the measured values with those computed from deviation-angle rules were not attempted.

Under all operating conditions the radial distribution of loss coefficient (fig. 12(j)) shows similar trends, a relatively low value from the hub to the mean section and a very sharp increase in loss coefficient from the mean to the tip region. If the losses measured across a blade element resulted primarily from a blade-profile type of loss, it would be anticipated that the level of loss at any given blade element would follow the trend of blade loading - expressed herein as the diffusion factor D. At no element is a consistent trend of loss with D evident (fig. 12(k)). In fact, the loss level at the radial station 30 percent

of passage height from the tip is up to 10 times larger than that measured at the radial station 70 percent of passage height from the tip, even for approximately the same value of D (i.e., blade loading). For the flat-plate helical inducer radial transport of blade boundary layer, losses associated with secondary flows, tip clearances, and so forth, assume added importance and must be understood more clearly before a prediction of inducer loss can be attempted.

The variation of efficiency with radius (fig. 12(l)) shows sharp decreases in efficiency from the mean to the tip region (inverse of the loss coefficient distribution). The dependency of efficiency on work input as well as loss is demonstrated in the efficiency curves. In general, the variation of loss coefficient at any given element is not very large, except at the hub elements; consequently, the level of efficiency and ideal head rise vary in the same direction.

The effects of speed on the noncavitating blade-element performance are presented in figures 13 to 15. Performance at three flow coefficients covering the range of operation was compared. When examining the curves, it should be remembered that at these high inlet angles the performance is very sensitive to changes in flow coefficient (see fig. 11). Thus, an evaluation of performance must consider differences in flow coefficient as well as speed even though the former are usually small.

At the high and mean flows the radial distributions of inlet flow coefficient and incidence angle are similar and close enough in value that inlet flow geometry is maintained. The low-flow runs are located in a region where significant redistributions of inlet mass flow are occurring, and even small differences in the location of the operating point on the characteristic curve show significant changes in the inlet distributions of flow coefficient and incidence angle. Inlet flow angles measured in the tip region at the lowest speed were over 50°. At the mean and highest speed the flow angles were 5° or less. Obviously, at this low-flow condition differences in performance cannot be related entirely to changes in blade speed; consequently, so-called speed effects will be directed to the results obtained at the two higher flows.

The overall performance showed no measurable variation in the overall head-rise coefficient over the speed range covered. Figure 13 shows that similar radial distributions existed at all speeds and that the slight differences in $\bar{\psi}$ occurring because of small variations in $\bar{\varphi}$ are generally reflected at all radii. One primary performance parameter to show an effect with blade speed is total-pressure-loss coefficient. In the hub region no consistent trend with speed can be observed, but from the mean to the tip section an inverse relation between speed and loss coefficient appears.

With the inlet flow geometry and the fluid properties maintained, the Reynolds number is used as the basic parameter on which to base

performance comparisons. Reference 12 reports that cascade data showing the effect of the Reynolds number on the measured losses reveal, in all cases, an increasing trend of loss coefficient with decreasing Reynolds number. The limiting Reynolds number (the value of Reynolds number at which a sharp increase in loss is obtained) based on the blade chord was in the vicinity of 2.5×10^5. The data (ref. 12) were obtained from air cascades of typical blade shapes employed in axial-flow compressors.

Based on the chord length and the blade speed at the rotor tip, the Reynolds number covered in this investigation ranged from 1.85×10^7 for $N = 7500$ rpm to 3.70×10^7 for $N = 15,000$ rpm. At these high values, several orders of magnitude above the transition values determined in reference 12, the effects of the Reynolds number on loss would be anticipated to be small. When the speed is varied from 7500 to 11,250 rpm, the observed changes in $\bar{\omega}$ are small. However, with a further increase in speed to 15,000 rpm, significant decreases in loss coefficient are noted. This latter sharp decrease in loss coefficient would be of the order of magnitude anticipated when operating in a critical, or limiting, Reynolds number range. When compared with the limiting values noted previously (ref. 12), it must be remembered that the data from this investigation were obtained from a flat-blade shape with blade chords 5 to 10 times as large as those for typical axial-flow compressor blades, and in a different fluid.

The complicated loss picture evidenced for this rotating three-dimensional cascade makes any loss analysis very difficult. The Reynolds number could conceivably affect the loss (excluding regions affected by hub and tip casing boundary layer) by affecting, for example,

(1) Profile loss (drag or resistance to flow around the blade profile)

(2) The amount of radial transport of blade boundary layer

(3) Losses associated with this secondary flow along the blade surfaces

Although the separate effects of the Reynolds number could not be established, figures 13 and 14 indicate that this overall level of loss is changing with the Reynolds number and shows the same trends as indicated by the cascade data of reference 12.

The loss data presented thus far indicate the following:

(1) At constant Reynolds number, loss did not show a consistent variation with loading (see fig. 12). The sharp increase in loss from the mean to the tip regions indicates that low-energy boundary-layer fluid from the hub is probably being transported into the tip regions, and losses associated with these secondary flows must be considered.

(2) As the Reynolds number is varied from 2.775×10^7 to 3.70×10^7, except in the hub region, there is a significant decrease in loss as the Reynolds number is increased. This large drop seems to indicate that the Reynolds number range covered may lie in or close to a transition range for this type of blade. Whether these results represent the effects of the Reynolds number primarily on any single type of loss (profile, secondary flow, etc.) could not be determined.

Individual effects of the different loss gradients on deviation angle and outlet axial velocity are not consistently indicated, but the overall result is a reduction of energy input (ideal head rise) at all radii as speed increases. The combination of lower ideal head rise and lower loss as speed is increased results in the same measured head rise at all speeds but at an increased efficiency.

Cavitating Performance

The general method of presenting cavitation performance is to show blade performance at a number of successively lower inlet pressures (H_{sv} or $\bar{k}$) until the performance is some small percentage of its noncavitating value. Over such a range of operation three or four stages of cavitation are generally identified. Both references 2 and 3 discuss this type of investigation more fully. The investigation reported herein was concerned with the effects of speed on cavitation performance. The required time to obtain radial survey data precluded obtaining these comparisons under a large number of stages of cavitation. The two $(H_{sv})_N$ values selected represent operation in the high-suction-specific-speed range (i.e., 24,000 to 27,000) for this type of inducer operating in water. Under these conditions, the performance has decreased from 15 to 40 percent from its noncavitating level. This is a typical area of operation an inducer would be required to work in when coupled with a high-speed pressure-producing pump.

Changes in cavitation performance with speed represent one phase of the more general question of scale effects. Reference 13 defines scale effects on cavitation as departures from the classical similarity relations when size, velocity, and/or properties of the fluid are changed. As generally used with pumps, the classical law of similarity with respect to cavitation takes the form:

$$k = \frac{h_1 - h_v}{\frac{V_1'^2}{2g}} \tag{7a}$$

or, based on blade tip speed and the assumption of no inlet whirl (i.e., $V_{\theta_1} = 0$):

$$k = \frac{2gH_{sv}}{U_t^2\left[\left(\frac{r}{r_t}\right)^2 + \varphi^2\right]} - \frac{\varphi^2}{\left(\frac{r}{r_t}\right)^2 + \varphi^2} \tag{7b}$$

Equation (7a) or (7b) gives a local or blade-element value of cavitation number. When referring to a complete blade, a form of equation (7b) is used in which the tip speed and an average inlet velocity based on measured flow and inlet geometric flow area are substituted. Equation (7b) then becomes

$$\bar{k} = \frac{2gH_{sv}}{U_t^2(1 + \bar{\varphi}^2)} - \frac{\bar{\varphi}^2}{1 + \bar{\varphi}^2} \tag{7c}$$

and this form of cavitation number is designated by $\bar{k}$. Reference 13 examines and tabulates the various phenomena governing scale effects, the resulting similarity laws, and expected scale effects.

It is recognized that the three-dimensional rotating cascade is not an ideal vehicle for studying basic factors governing scale effects. The flow is not subject to exact analysis, and local flow conditions are not measured. However, since the three-dimensional flow conditions represent the actual environment in which a pump rotor operates, scale effects as measured under more simplified and controlled conditions must be correlated with the measured rotor performance results. At least in this latter area the succeeding performance results should be of value.

In the tests reported herein the water temperature (cold water) was maintained constant, the air content was approximately the same, and the same rotor was used for all tests. It is possible that the surface roughness as effected by cavitation damage may have varied slightly at the different speeds as the amount of time the rotor operated under cavitating conditions increased. Under these conditions, the major variable is the velocity. Reference 13 lists a number of parameters using velocity; however, in most investigations the Reynolds number was selected as the basic variable.

The following sections present the data observed under cavitating conditions. The presentation stresses changes in performance as blade speed is varied. In general, the curves are self-explanatory, and only the most significant points are discussed. Because the data cover a limited range of speeds and/or Reynolds numbers and were obtained from a

rotor with a particular blade type and geometry, no attempt is made to generalize scale effects.

Overall performance. - Figure 16 compares the overall performance under cavitating conditions at the three rotor speeds. Head-rise coefficient and efficiency are presented as functions of flow coefficient for several values of normalized suction head. Noncavitating performance is included for comparative purposes. The head-rise coefficient and efficiency represent mass-averaged values, while the flow is that measured by the Venturi meter. Normalized net positive suction head values of 65 and 60 feet represent operation in the 24,000 to 27,000 range of suction specific speed.

It is obvious from this figure that, while speed had no measurable effect on this head-flow characteristic curve under noncavitating conditions, it does visibly affect the cavitation performance of the inducer. At $(H_{sv})_N$ values of 65 and 60 feet the head-flow characteristic curves at blade speeds of 15,000 and 11,250 rpm show little change. In fact, the performance at 11,250 rpm appears to be slightly superior at the lower $(H_{sv})_N$ value. However, at the lowest speed (i.e., N = 7500 rpm) the head coefficient is lower at all flows than that obtained at the two higher speeds. The slope of the performance curves is approximately the same. Efficiency also shows a definite change with a variation of speed. At both $(H_{sv})_N$ values the efficiency generally shows a consistent trend with speed at all operating conditions; that is, as speed is decreased, the efficiency also decreases. A more significant effect of cavitation on efficiency may be the percentage decrease from the noncavitating value as the degree of cavitation is increased (i.e., as $(H_{sv})_N$ is lowered). In general, at a given operating point (flow coefficient), the percentage decrease in efficiency from the noncavitating value, as $(H_{sv})_N$ is lowered, is approximately the same for N = 15,000 and 11,250 rpm but greater for N = 7500 rpm. Considering operation at a constant speed and flow coefficient, the efficiencies always decrease as $(H_{sv})_N$ decreases.

Blade-element performance. - The blade-element performance is presented as radial variations of the various flow and performance parameters. An effort is again made to separate the effects of speed and cavitation on performance by presenting first a variation with $(H_{sv})_N$ where N is constant and then a comparison of performance at various speeds at constant values of $(H_{sv})_N$ and $\bar{\varphi}$.

Figure 17 presents changes in performance at a constant blade speed of 15,000 rpm and a flow coefficient of approximately 0.10 for $(H_{sv})_N$

values of 160, 65, and 60 feet. Corresponding suction specific speeds are 13,000, 25,580, and 27,131, respectively.

The head-rise-coefficient distribution (fig. 17(f)) shows a dropoff at all radii as $(H_{sv})_N$ is decreased from the noncavitating value. For $(H_{sv})_N$ = 60 feet, the percentage decrease in head rise from a noncavitating value is within a few percent of being a constant value at all radii. Similar results were found in the data reported in reference 3.

The head rise obtained is dependent upon the ideal head rise (fig. 17(h)) and losses (fig. 17(j)). Figure 17 shows that the effect of reducing the net positive suction head on these parameters is to reduce the energy input (ideal head rise) and increase the loss coefficient at all radii. Both of these trends adversely affect the ability of the inducer to produce head rise.

Radial variations of outlet axial velocity (fig. 17(e)) and deviation angle (fig. 17(i)) presented in figure 17 represent flow conditions 1 inch downstream of the blade trailing edge. As the intensity of cavitation is increased (H_{sv} is lowered), the radial equilibrium requirements are relaxed, and the sharp radial gradients of axial velocity are reduced. In reference 3 when this occurred, the dropoff in axial velocity in the tip region at the blade inlet was also alleviated. Although this operating point does not clearly show this, some redistribution of the inlet velocities (fig. 17(b)) is taking place. Negative deviation angles in the tip region are again noted for the flow conditions showing the steep gradients of axial velocity at the rotor outlet. These are believed to result from curvature of streamlines downstream of the rotor as it affects the velocity-diagram calculations. This is discussed more completely in reference 3.

In summary, the effects of lowering H_{sv} on the radial distribution of performance parameters obtained at this operating point parallel those observed from the investigation of a 78° inducer reported in reference 3. At other operating points, variations in performance as H_{sv} is lowered would be expected to follow the trends reported in reference 3. For this reason, the remaining portion of the presentation is devoted to showing any effects of speed on performance at various operating points and $(H_{sv})_N$. Figures 18 to 20 compare the performance at the three blade speeds for a constant $(H_{sv})_N$ of 65 feet and at three operating points covering the range of operation. Figures 21 to 23 present the same comparisons at an $(H_{sv})_N$ of 60 feet. Since the variations of performance parameters with speed are similar at the two values of $(H_{sv})_N$, the two sets of figures will be discussed concurrently.

At all operating conditions, the inlet flow geometry (parts (a) to (d) of figs. 18 to 23) appears to be maintained. The inlet radial distributions of flow coefficient are similar with any small differences in level reflecting the slight differences in overall flow coefficient. The low inlet flow angles (part (d) of figs. 18 to 23) indicate negligible amounts of prerotation are occurring in all cases, and the blade is operating at the same cavitation number (part (c) of figs. 18 to 23). Under classical similarity relations, the form and extent of cavitation at all speeds should be similar.

The radial variations in head-rise coefficient (part (f) of figs. 18 to 23) repeat the results shown by the overall performance curves; that is, although the inlet conditions indicate that similar cavitation conditions exist, the dropoff of head rise due to cavitation effects is affected by the speed at which the rotor operates. They show further that the effects are felt in a similar fashion at all radial locations. For operation at a given $(H_{sv})_N$, the loss coefficient (part (j) of figs. 18 to 23) shows the same relation with speed both in regard to level and radial distribution, as indicated by noncavitating operation. Also, at all speeds, the level of loss coefficient generally shows an increase over the noncavitating value. However, cross-plotting of the data to determine if the percentage increase in $\bar{\omega}$ over the noncavitating value differed with speed proved inconclusive.

As noted earlier in this report and in reference 3, a second effect of cavitation on pump operation was to decrease its capability to add energy to the fluid for a given inlet flow geometry (i.e., flow coefficient). This was observed as a decrease in ideal head rise (part (h) of figs. 18 to 23) as $(H_{sv})_N$ is decreased. At all three speeds this latter observation applies. Also, a cross-check of the various element performance values (figs. 13 to 15 and 18 to 23) generally indicates the following:

(1) At speeds of $N = 15,000$ and 11,250 rpm, the percentage decrease of ψ_i from the noncavitating value was roughly the same for all radii and showed no consistent trend with speed.

(2) At $N = 7500$ rpm, the percentage decrease in ψ_i from the noncavitating level was greater for all radii than that observed at either of the two higher speeds.

The cavitating performance obtained at the three speeds indicates that scale effects (i.e., departures from similarity relations as defined by the cavitation number k) do occur with changes in rotor speed. In investigations of scale effects the effect of time on the vaporization process must be considered. Suggested means of accomplishing this

include the use of a "characteristic" velocity (which does not increase proportionally to the flow velocity), application of bubble growth rates, and employment of heat-transfer rates. As yet, quantitative results useful for further establishment of cavitation similarity relations have not been obtained. Since the results presented herein show that cavitation performance was noticeably improved as speed was increased from 7500 to 11,250 rpm but showed no further gains as speed was increased to 15,000 rpm, it is evident that scale effects due to rotor speed are not predictable from a simple mathematical model. It may further be hypothesized that a critical speed or time exists above which the effects of cavitation on performance do not change. Specifically, care should be exercised when extrapolating anticipated scale effects due to rotor speed.

Radial equilibrium. - In a design system as well as in some analysis problems, some form of the radial equilibrium equation must be solved in order to compute velocity diagrams. The simplest form, and one widely used for incompressible flow, is one known as a simple radial equilibrium expression; it equates the radial static head gradient to the whirling motion of the fluid and neglects any effects due to radial motion of the fluid, and is defined as equation (1). The applicability of the simple radial equilibrium assumption to flow at the outlet of the inducer is investigated by comparison of the distributions of measured axial velocities with those computed by use of the measured values of total pressure and flow angle in equation (1). Figure 24 presents comparisons covering a range of speeds and operating conditions for both cavitating and noncavitating flow. The good correlations obtained indicate that equation (1) is applicable to the flow conditions at the outlet of a flat-plate inducer under all operating conditions. Reference 14 discusses the use of the various forms of the radial equilibrium equation in detail.

SUMMARY OF RESULTS

The experimental data obtained from an 80.6° flat-plate helical inducer operated at three blade speeds (N = 7500, 11,250, and 15,000 rpm) indicated:

Under noncavitating conditions:

1. The overall head coefficient as a function of the flow coefficient characteristic was the same for all blade speeds, as predicted by the similarity relation.

2. Over the range of speed (i.e., the Reynolds number) covered, the overall efficiency varied with rotor speed, although there was no consistent trend at all operating conditions. The highest degree of efficiency occurred at the highest rotor speed (or the highest Reynolds number). This implies that, over the range of test conditions covered in

this investigation, the similarity relation regarding power input would not have been applicable.

3. The radial distributions of loss coefficient and comparison of loss coefficient with a loading parameter indicated the probable importance of secondary motions (specifically, the radial transport of blade boundary layer) in determining the level and distribution of loss. Measured loss coefficients showed a significant variation with speed in the mean and tip regions of the blades with the minimum loss coefficients occurring at the highest rotor speed. Lack of a consistent trend with speed suggests that a transition range of the Reynolds number may have been covered.

4. The variation of energy input with speed was similar to that of loss coefficient, with the net result that the measured head-rise coefficient was the same at all speeds, although the efficiency of the process varied.

Under cavitating conditions:

1. The decrease of overall head coefficient from the noncavitating value under classical similarity conditions (i.e., the average cavitation number is constant) showed differences with rotor speed but not in a generally predictable manner. Similar variations in overall efficiency were also noted.

2. General effects of cavitation were to increase loss coefficient and decrease the energy input, both of which adversely affected the ability of the inducer to produce a head rise.

3. The effects of speed on the head-rise coefficient measured at each individual blade element were similar and showed the same trends as those of overall performance.

4. At all rotor speeds the loss coefficient increased over the noncavitating value as the normalized net positive suction head was decreased. However, the percent increase over the noncavitating value did not demonstrate a consistent trend with speed.

5. At all rotor speeds, the energy addition decreased from the noncavitating value as the normalized net positive suction head was lowered. For $N = 15,000$ and 11,250 rpm operation, the percentage decrease from the noncavitating value was roughly the same at all radii. At $N = 7500$ rpm the percentage decrease was consistently lower than that observed at either of the two higher speeds.

6. The close agreement between the radial distributions of measured axial velocities and those computed from the simple radial equilibrium

expression indicates the latter assumption could be applied to all flow conditions at the blade outlet, both cavitating and noncavitating.

Visual studies indicated the following:

1. As the flow coefficient was decreased (and blade loading increased), the tip vortex extended increasing distances into the inlet flow passage. During noncavitating flow the tip vortex (made visible by cavitation occurring at its core) stood near the blade leading edge. At a given flow coefficient, as cavitation was intensified (the net positive suction head was lowered), the strong tip vortex moved rearward along the blade, which indicated the rearward shifting of blade loading.

2. At the lowest operating speed (N = 7500 rpm), the tip vortex cavitation extended a greater distance along the blade passage from the leading edge than that photographed at either of the higher rotative speeds (viz., 11,250 and 15,000 rpm). In general, the extent of blade surface cavitation followed that of the more easily distinguished tip vortex cavitation.

Lewis Research Center
National Aeronautics and Space Administration
Cleveland, Ohio, August 3, 1962

APPENDIX A

SYMBOLS

D	diffusion factor (defined in eq. (B10))
g	acceleration due to gravity, 32.17 ft/sec^2
H	total head, ft
H_{sv}	net positive suction head, $H_1 - h_v$, ft
h	static head, ft
h_v	vapor pressure, ft
i	incidence angle, deg
k	cavitation number (defined in eq. (B9))
m	function of blade stagger angle
N	rotative speed, rpm
P	total pressure, lb/sq in.
p	static pressure, lb/sq in.
Q	weight-flow rate, gal/min
r	radius, ft
S	suction specific speed, $N\sqrt{Q}/(H_{sv})^{3/4}$
U	rotor speed, ft/sec
V	fluid velocity, ft/sec
β	fluid angle, angle between fluid velocity and axial direction, deg
γ	blade angle, angle between tangent to blade mean camber line and axial direction, deg
δ	deviation angle, deg
η	efficiency

σ solidity, ratio of chord to spacing

φ flow coefficient

ψ head-rise coefficient

$\bar{\omega}$ relative total-pressure-loss coefficient

Subscripts:

h hub

i ideal

m measured

N normalized

S measurement made on static wedge probe

T measurement made on claw total probe

t tip

V refers to Venturi flow measurements

z axial direction

θ tangential direction

1 measuring station at rotor inlet

2 measuring station at rotor outlet

Superscripts:

$-$ average value

$'$ relative to rotor

APPENDIX B

EQUATIONS

The blade-element calculations are the following:

Net positive suction head:

$$H_{sv} = H_1 - h_v \tag{B1}$$

Ideal head rise:

$$\Delta H_i = \frac{U_2 V_{\theta,2} - U_1 V_{\theta,1}}{g}$$

$$= \frac{U_2 V_{\theta,2}}{g} \qquad (V_{\theta,1} = 0) \tag{B2}$$

Head-rise coefficient:

$$\psi = \frac{\Delta H}{\frac{U_t^2}{g}} \tag{B3}$$

Ideal head-rise coefficient:

$$\psi_i = \frac{\Delta H_i}{\frac{U_t^2}{g}}$$

Flow coefficient:

$$\varphi = \frac{V_z}{U_t} \tag{B4}$$

Relative total-pressure-loss coefficient:

$$\bar{\omega} = \frac{H'_{2,i} - H'_2}{\frac{V_1'^2}{2g}} = \frac{\Delta H_i - \Delta H}{\frac{V_1'^2}{2g}} \tag{B5}$$

Incidence angle:

$$i = \beta_1' - \gamma_1 \tag{B6}$$

Deviation angle:

$$\delta = \beta_2' - \gamma_2 \tag{B7}$$

Efficiency:

$$\eta = \frac{\Delta H}{\Delta H_i} \tag{B8}$$

Cavitation number:

$$k = \frac{h_1 - h_v}{\frac{V_1'^2}{2g}} \tag{B9}$$

Diffusion factor:

$$D = 1 - \frac{V_2'}{V_1'} + \frac{\Delta V_\theta'}{2\sigma V_1'} \tag{B10}$$

The overall performance calculations are the following:

Average flow coefficient:

$$\overline{\varphi} = \frac{\overline{V}_{z,1}}{U_t} \tag{B11}$$

Average inlet axial velocity:

$$\overline{V}_{z,1} = \frac{Q_m}{448.8\ \pi\left(r_t^2 - r_h^2\right)} \tag{B12}$$

Mass-averaged inlet total head:

$$\overline{H}_1 = \frac{\int_{r_h}^{r_t} V_{z,1} r_1 H_1 \, dr_1}{\int_{r_h}^{r_t} V_{z,1} r_1 \, dr_1} \tag{B13}$$

Mass-averaged outlet total head:

$$\overline{H}_2 = \frac{\int_{r_h}^{r_t} V_{z,2} r_2 H_2 \, dr_2}{\int_{r_h}^{r_t} V_{z,2} r_2 \, dr_2} \tag{B14}$$

Mass-averaged head-rise coefficient:

$$\overline{\psi} = \frac{g}{U_t^2} \left(\overline{H}_2 - \overline{H}_1\right) \tag{B15}$$

Mass-averaged efficiency:

$$\overline{\eta} = \frac{\int_{r_h}^{r_t} V_{z,2} r_2 \eta \, dr_2}{\int_{r_h}^{r_t} V_{z,2} r_2 \, dr_2} \tag{B16}$$

Maintaining H_{sv}/N^2 constant means that, for any flow coefficient $\overline{\varphi}$, the cavitation number $\overline{k}$ is also maintained. In this investigation all actual H_{sv}'s used were presented in the report as values normalized to a comparable value at $N = 15{,}000$ rpm by the equation

$$\left(H_{sv}\right)_N = H_{sv}\left(\frac{15{,}000}{N}\right)^2 \tag{B17}$$

REFERENCES

1. Ross, C. C., and Banerian, Gordon: Some Aspects of High-Suction Specific-Speed Pump Inducers. Trans. ASME, vol. 78, no. 8, Nov. 1956, pp. 1715-1721.

2. Huppert, M. C., King, W. S., and Strepling, L. B.: Some Cavitation Problems in Rocket Propellant Pumps. Rocketdyne, North Am. Aviation, Inc., 1960.

3. Soltis, Richard F., Anderson, Douglas A., and Sandercock, Donald M.: Investigation of the Performance of a 78° Flat-Plate Helical Inducer. NASA TN D-1170, 1962.

4. Salemann, Victor: Effect of Speed on Hot Water NPSH. Paper presented at ASME Hydraulics Div. Conf., Houston (Texas), Mar. 1960.

5. Montgomery, John C.: Analytical Performance Characteristics and Outlet Flow Conditions of Constant and Variable Lead Helical Inducers for Cryogenic Pumps. NASA TN D-583, 1961.

6. Lieblein, Seymour, Schwenk, Francis C., and Broderick, Robert L.: Diffusion Factor for Estimating Losses and Limiting Blade Loadings in Axial-Flow-Compressor Blade Elements. NACA RM E53D01, 1953.

7. Acosta, A. J.: An Experimental Study of Cavitating Inducers. Paper presented at Second Symposium on Naval Hydrodynamics (Wash., D.C.), Aug. 25, 1958.

8. Crouse, James E., Montgomery, John C., and Soltis, Richard F.: Investigation of the Performance of an Axial-Flow-Pump Stage Designed by the Blade-Element Theory - Design and Overall Performance. NASA TN D-591, 1961.

9. Stepanoff, A. J.: Centrifugal and Axial-Flow Pumps. Second ed., John Wiley & Sons, Inc., 1957.

10. Spannhake, Wilhelm: Centrifugal Pumps, Turbines, and Propellers. The Technology Press, M.I.T., 1934.

11. Carter, A. D. S.: The Low-Speed Performance of Related Airfoils in Cascade. Rep. R-55, British NGTE, Sept. 1949.

12. Members of the Compressor and Turbine Research Division: Aerodynamic Design of Axial-Flow Compressors. Vol. II. NACA RM E56B03a, 1956.

13. Holl, J. William, and Wislicenus, George F.: Scale Effects on Cavitation. 60-WA-151, ASME, 1960.

14. Wu, Chung-Hua, and Wolfenstein, Lincoln: Application of Radial-Equilibrium Condition to Axial-Flow Compressor and Turbine Design. NACA Rep. 955, 1950. (Supersedes NACA TN 1795.)

TABLE I. - BLADE GEOMETRY FOR

80.6° HELICAL INDUCER

Rotor tip diameter, d_t, in.	[a]4.956
Rotor hub diameter, d_h, in.	[a]2.478
Hub-tip ratio	0.5
Radial tip clearance, in.	0.030
Tip clearance ratio[b]	0.024
Number of blades	3
Axial length, in.	2.0
Chord length at tip, in.	12.25
Chord length at hub, in.	6.362
Solidity at tip	2.361
Solidity at hub	2.455
Blade thickness at tip, in.	[c]0.1
Blade thickness at hub, in.	[c]0.15

[a]Constant.

[b]Tip clearance/blade height.

[c]Linear variation.

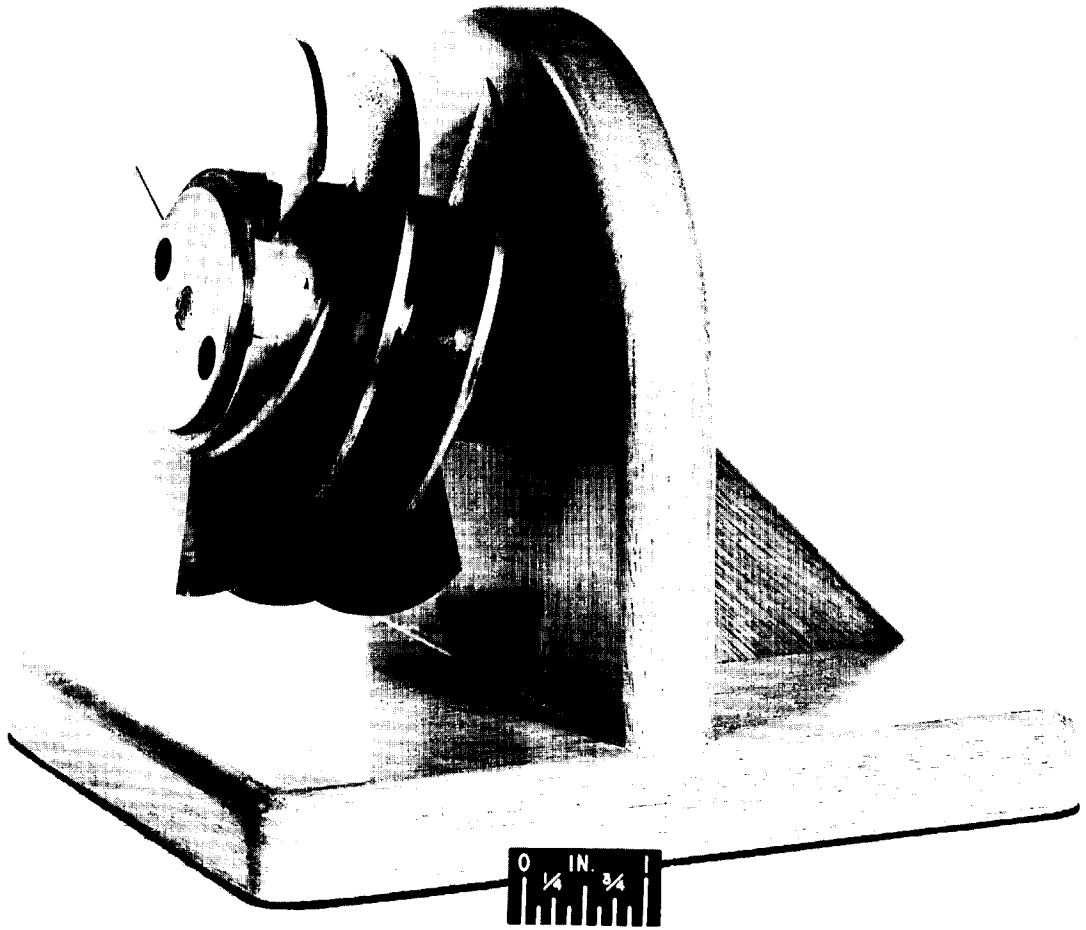

C-49045

Figure 1. - Test rotor.

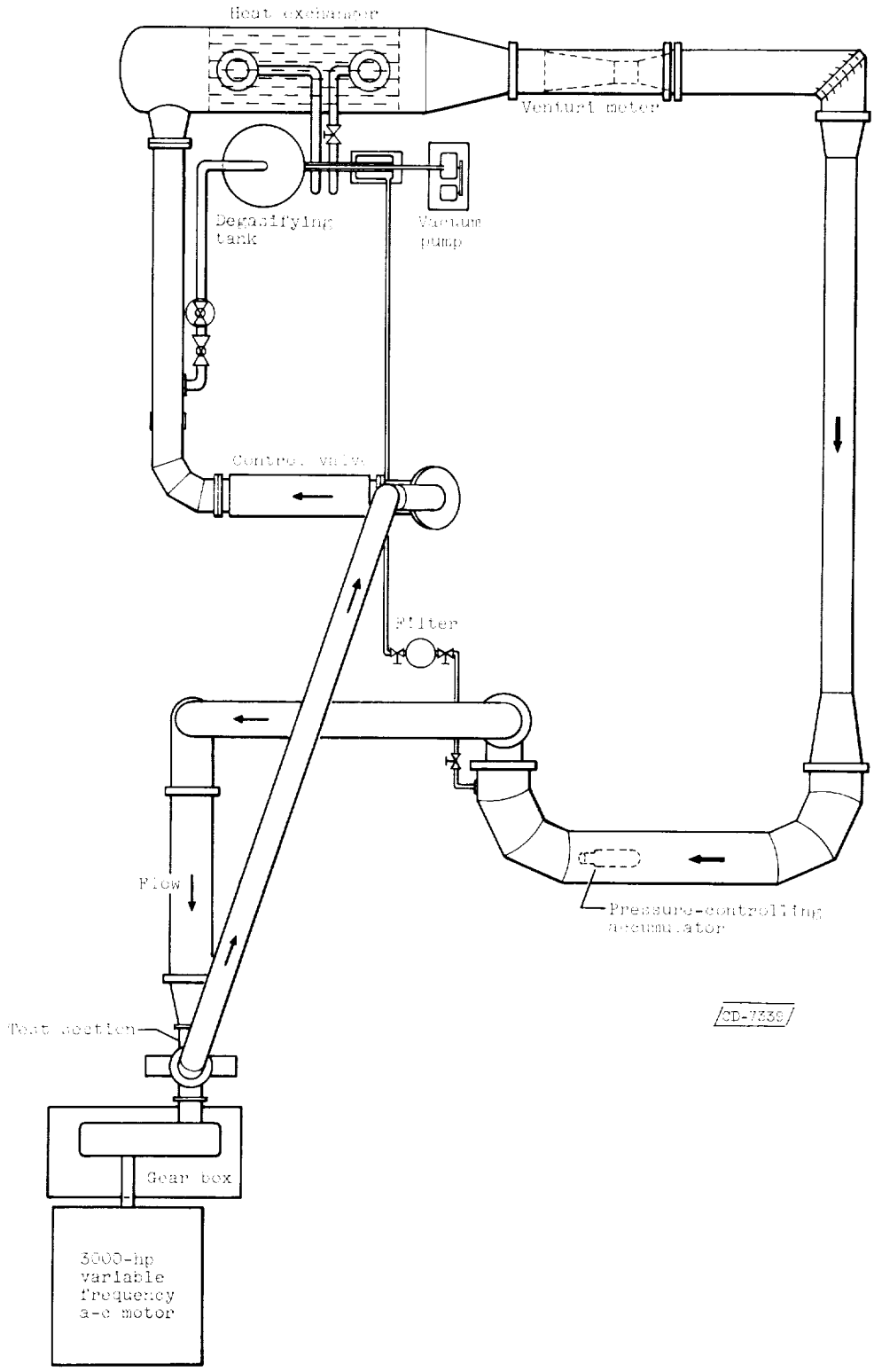

(a) Schematic diagram.

Figure 2. - Test facility.

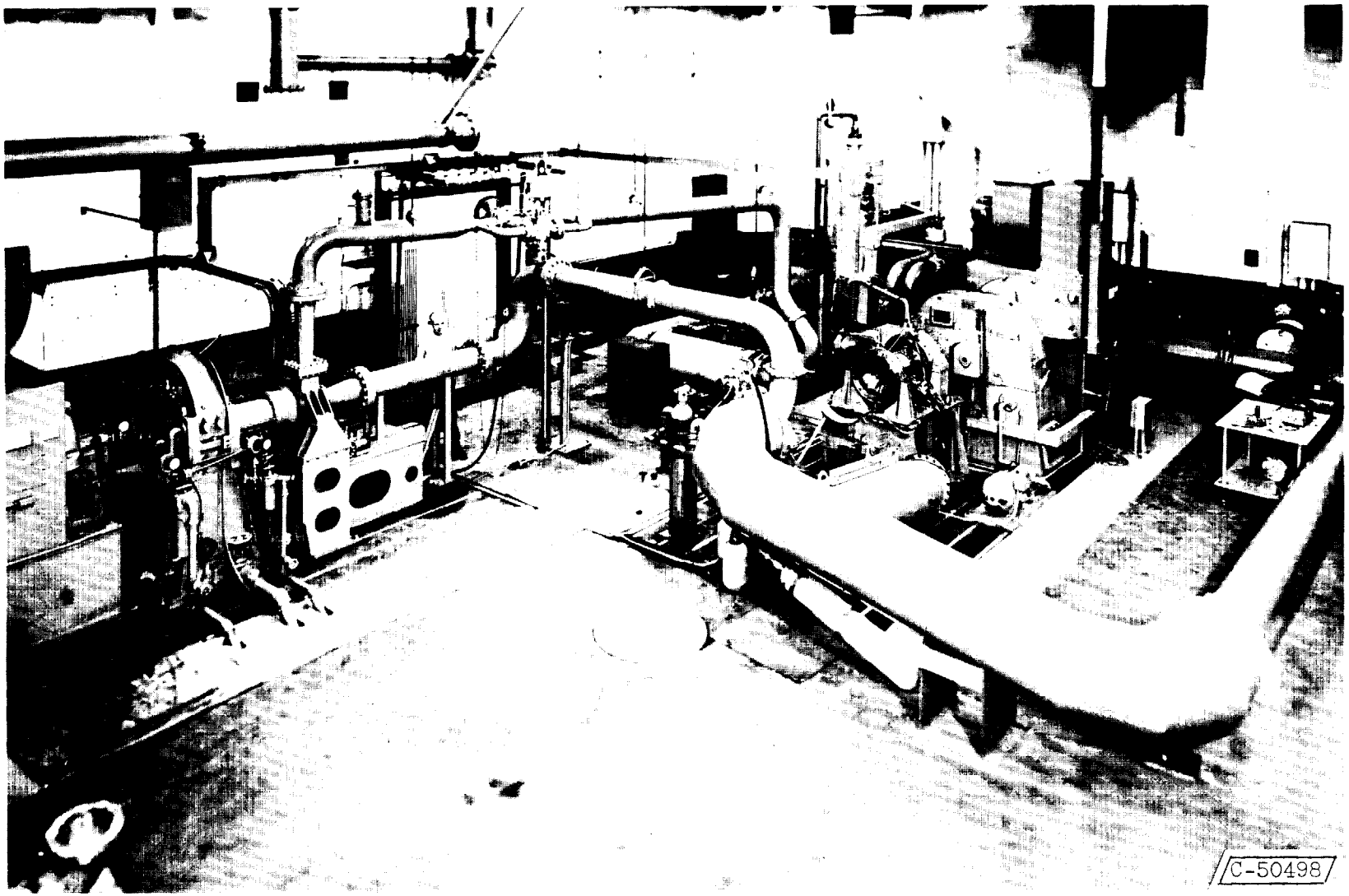

(b) Photograph.

Figure 2. - Concluded. Test facility.

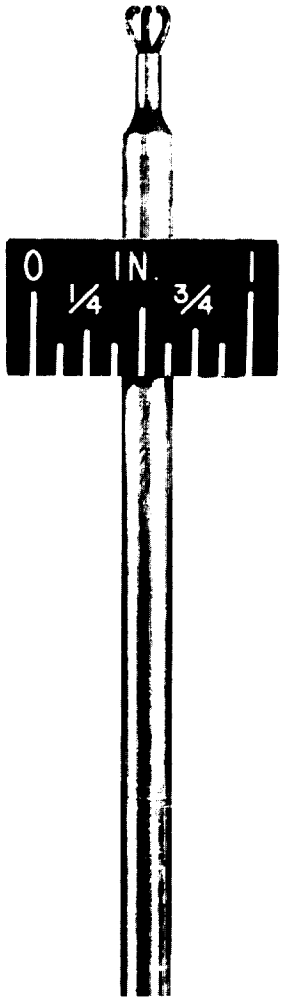

C-55432

(a) Total pressure claw.

Figure 3. - Probes.

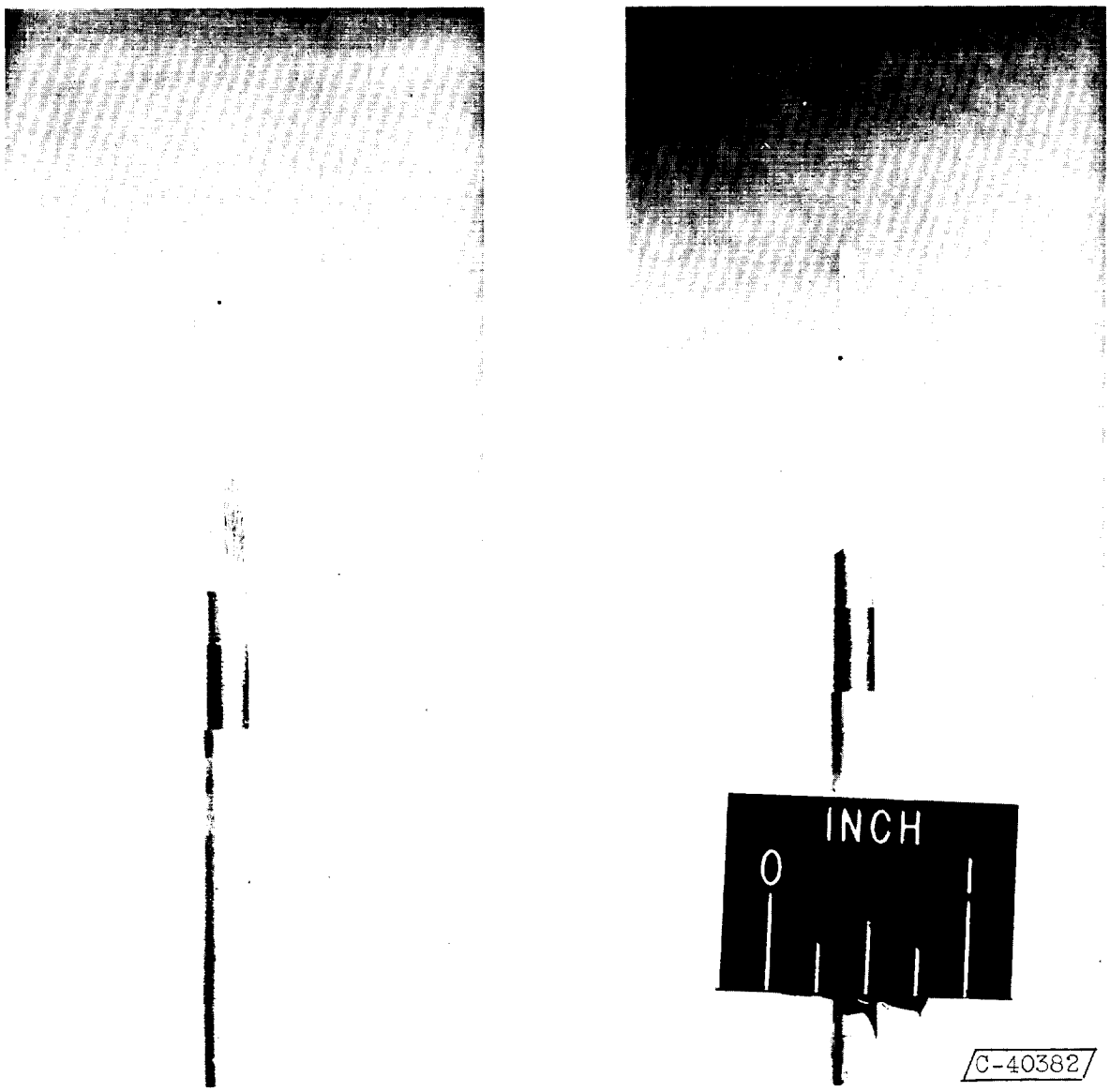

(b) Static pressure wedge.

Figure 3. - Concluded. Probes.

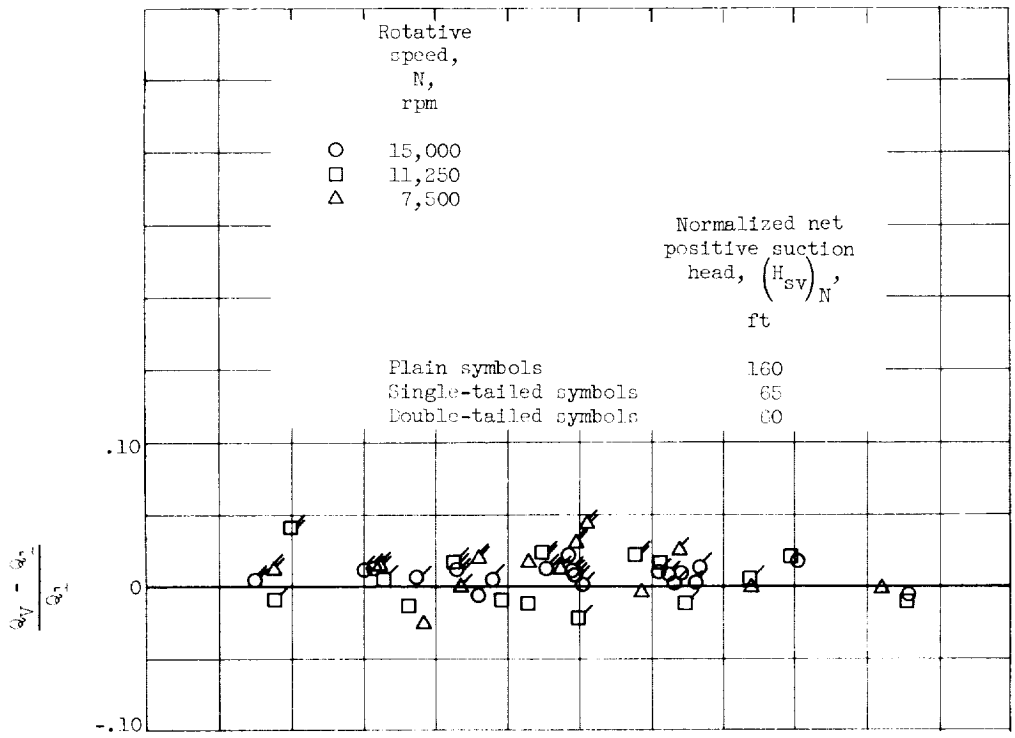

(a) Rotor inlet.

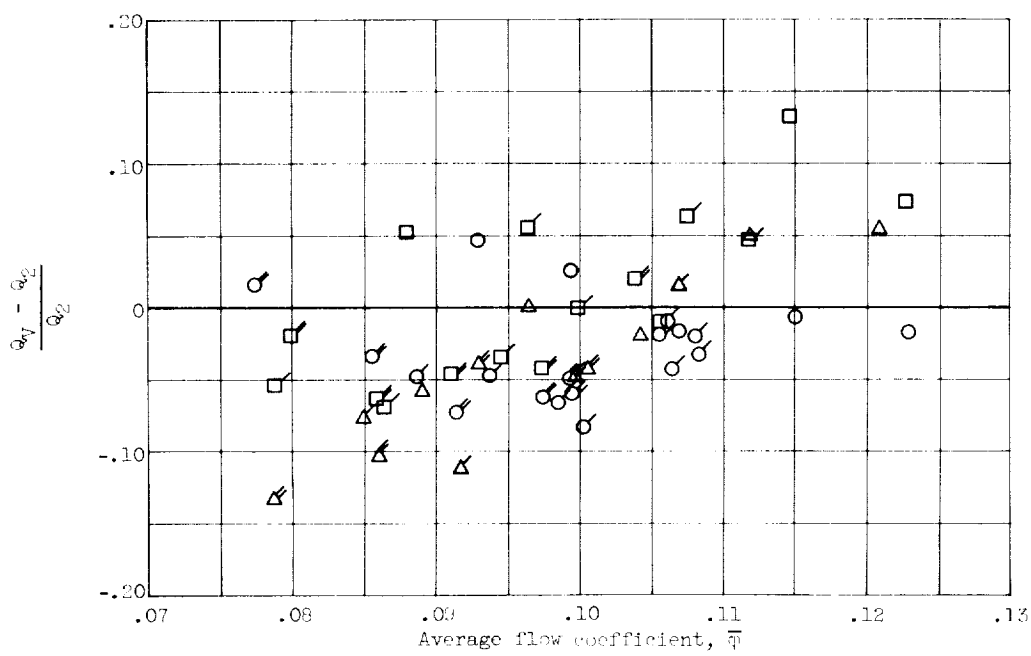

(b) Rotor outlet.

Figure 4. - Comparison of integrated flows with flows measured with venturi meter.

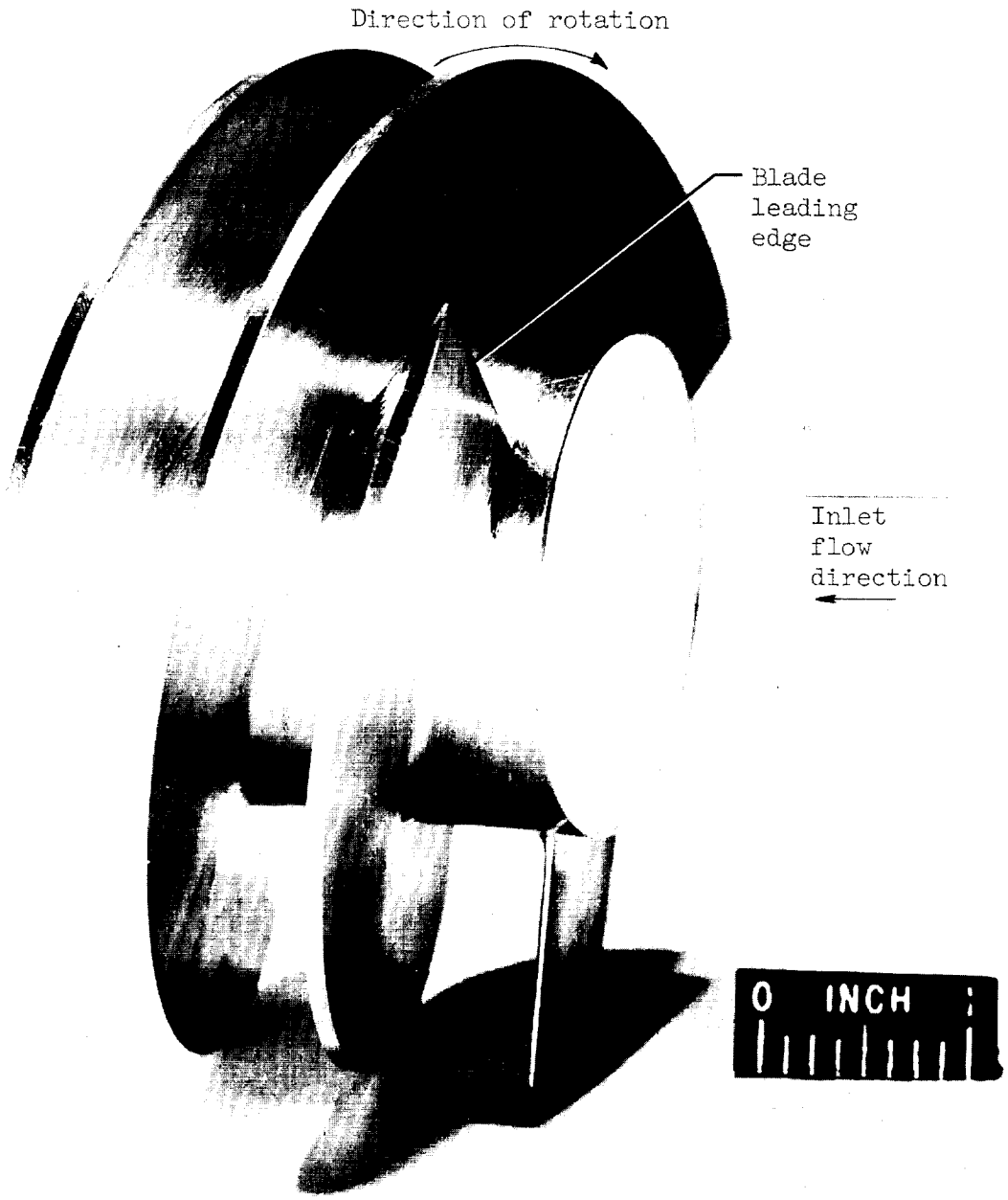

C-58616

Figure 5. - Orientation of flow direction and rotation of rotor.

(a) High flow.

(b) Low flow.

Figure 6. - Flow on various average flow coefficients and - smallest net positive suction heads, 750 Hz.

Normalized net positive suction head: 160 ft
Average flow coefficient: 0.100

65 ft
0.101

60 ft
0.100

Figure 7. - Flow at various inlet (H_{sv}) pressures and average flow coefficients. Rotative speed, 15,000 rpm.

Figure 9. - Flow of vortons average flow, centerline velocities. Normalized net positive suction head, 0 foot.

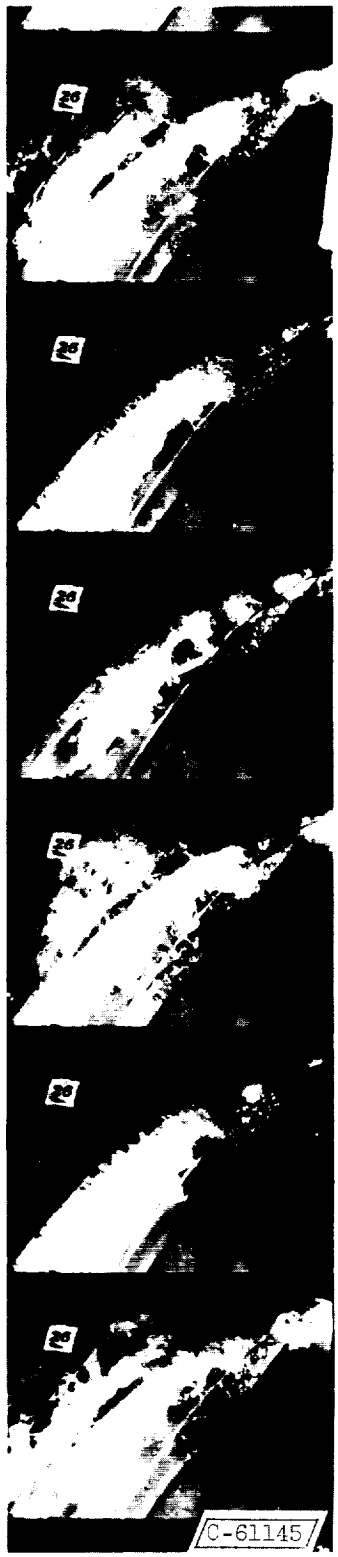

Figure 10. - Flow with unsteady cavitation.
Average flow coefficient, 0.124.

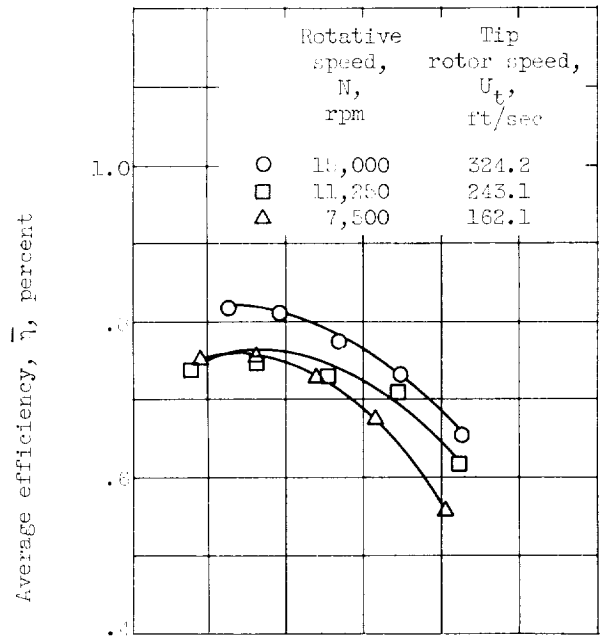

(a) Average efficiency.

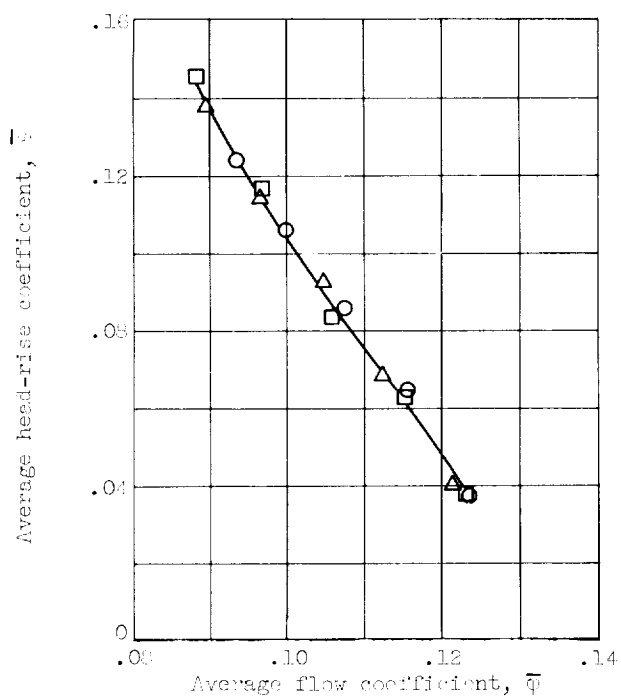

(b) Average head-rise coefficient.

Figure 11. - Overall performance (non-cavitating). Normalized net positive suction head, 180 feet.

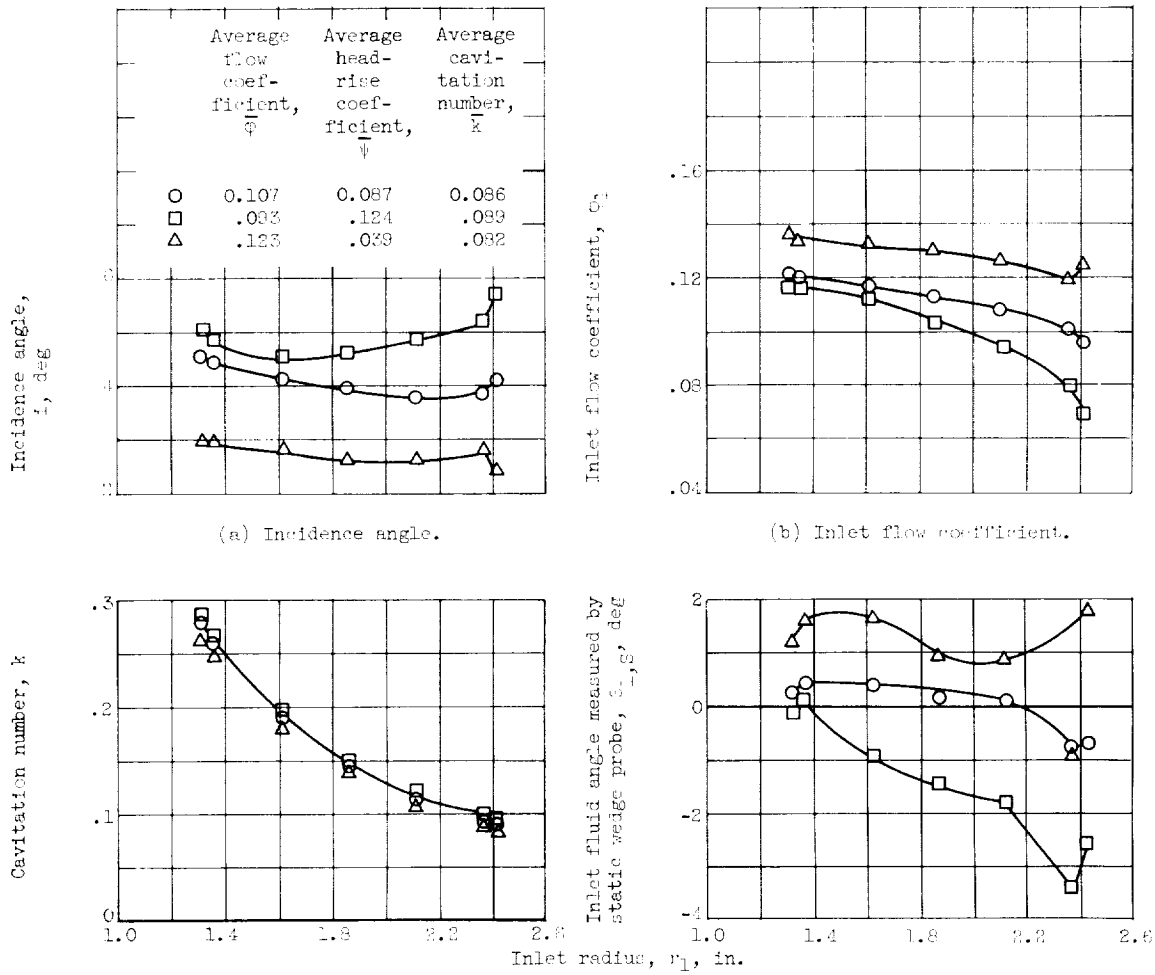

(a) Incidence angle.

(b) Inlet flow coefficient.

(c) Cavitation number.

(d) Inlet flow angle.

Figure 12. - Blade-element performance. Rotative speed, 15,000 rpm; normalized net positive suction head, 100 feet.

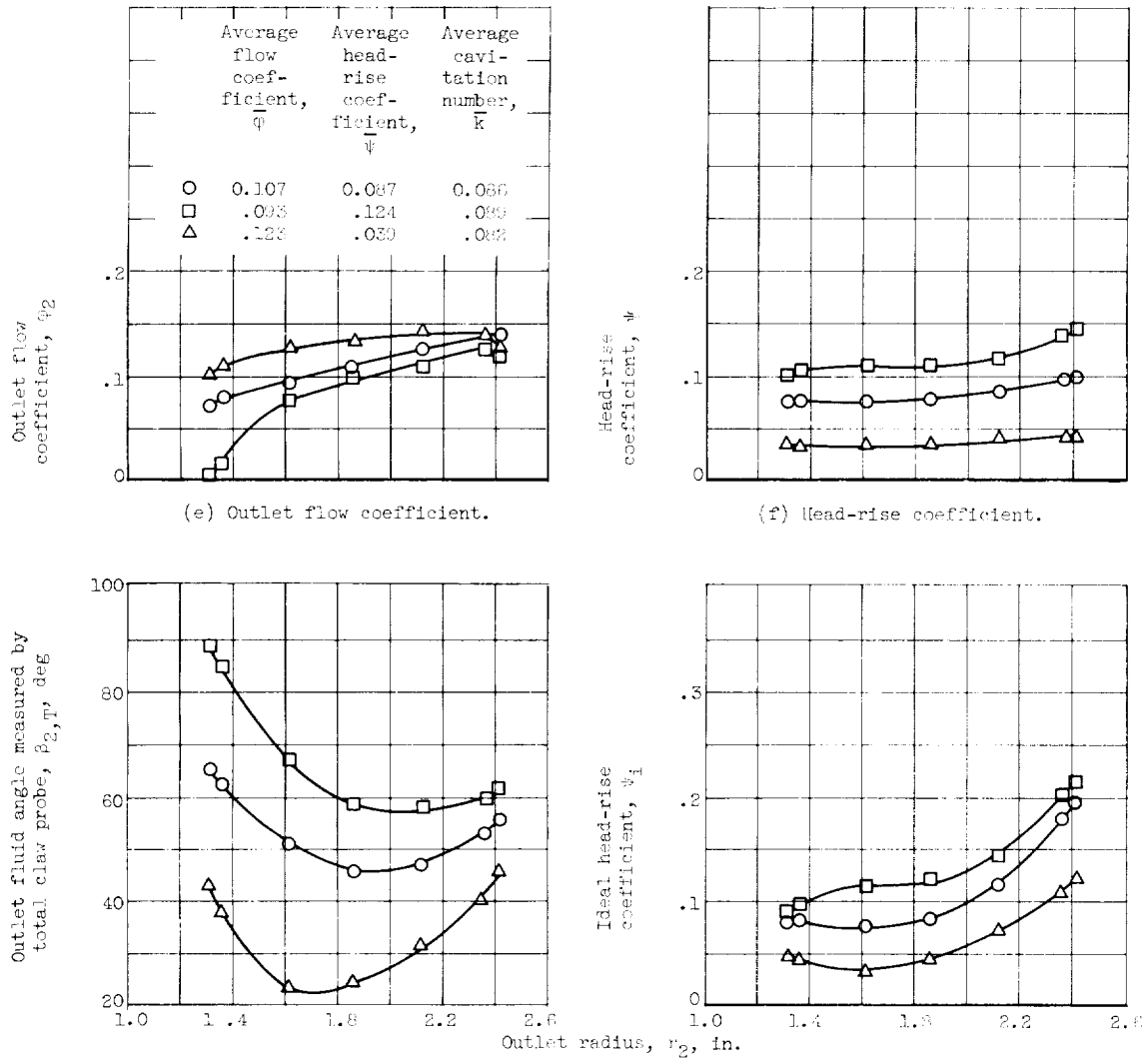

(e) Outlet flow coefficient.

(f) Head-rise coefficient.

(g) Outlet flow angle.

(h) Ideal head-rise coefficient.

Figure 12. - Continued. Blade-element performance. Rotative speed, 15,000 rpm; normalized net positive suction head, 160 feet.

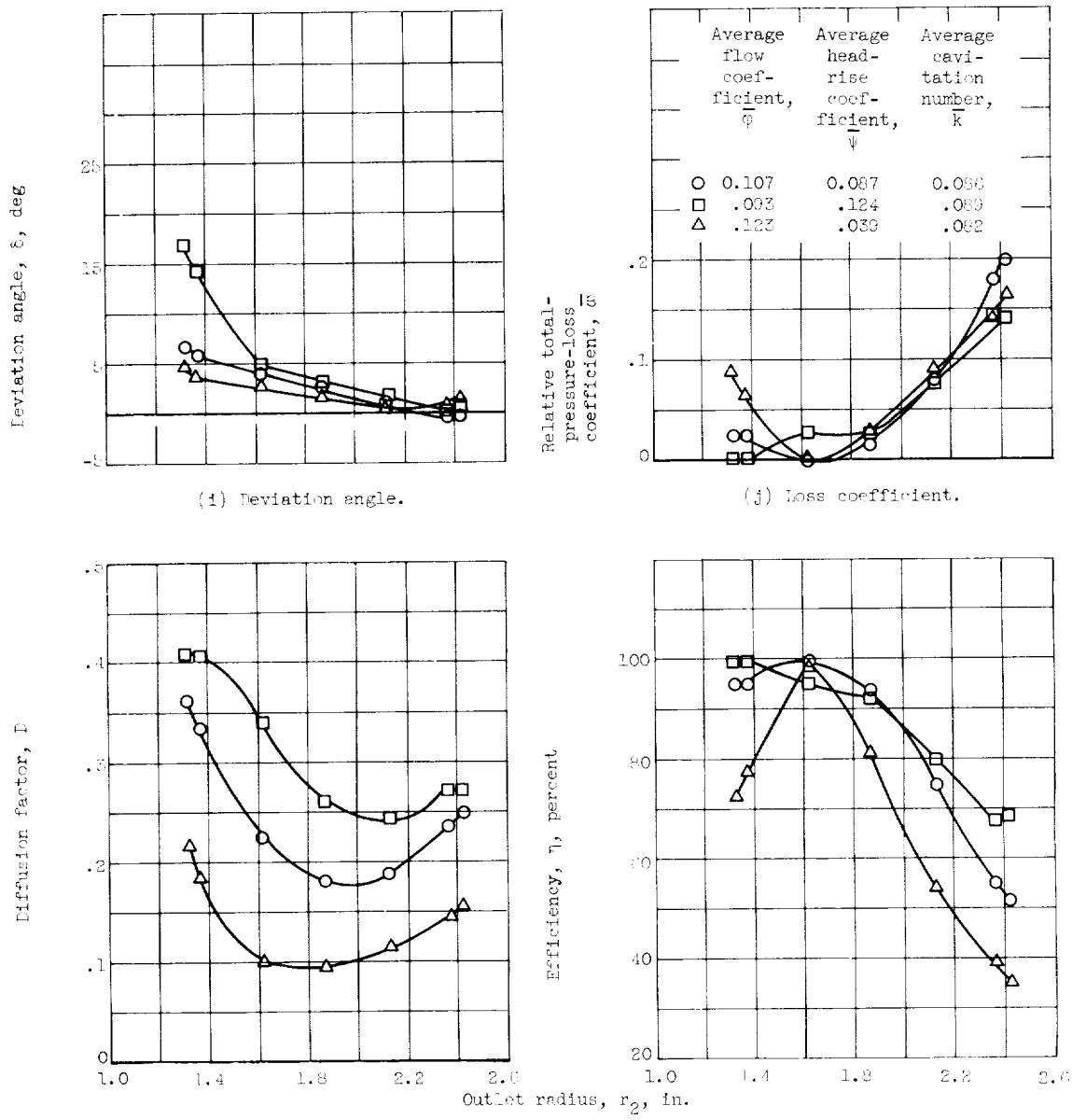

(i) Deviation angle.

(j) Loss coefficient.

(k) Diffusion factor.

(l) Efficiency.

Figure 12. - Concluded. Blade-element performance. Rotative speed, 15,000 rpm; normalized net positive suction head, 160 feet.

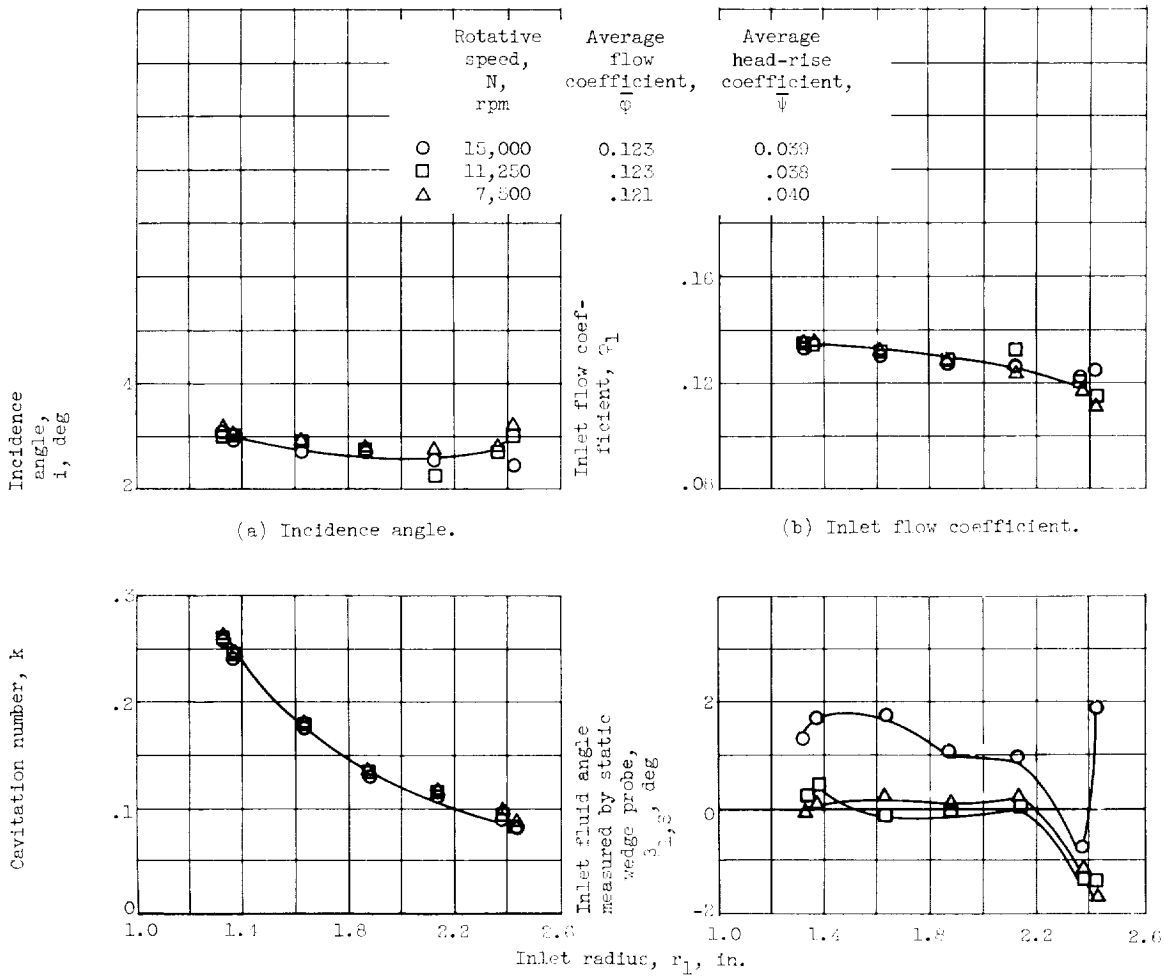

(a) Incidence angle.

(b) Inlet flow coefficient.

(c) Cavitation number.

(d) Inlet flow angle.

Figure 13. - Effect of rotor speed on blade-element performance in high flow operating region. Average flow coefficient, 0.122; normalized net positive suction head, 100 feet; average cavitation number, 0.082.

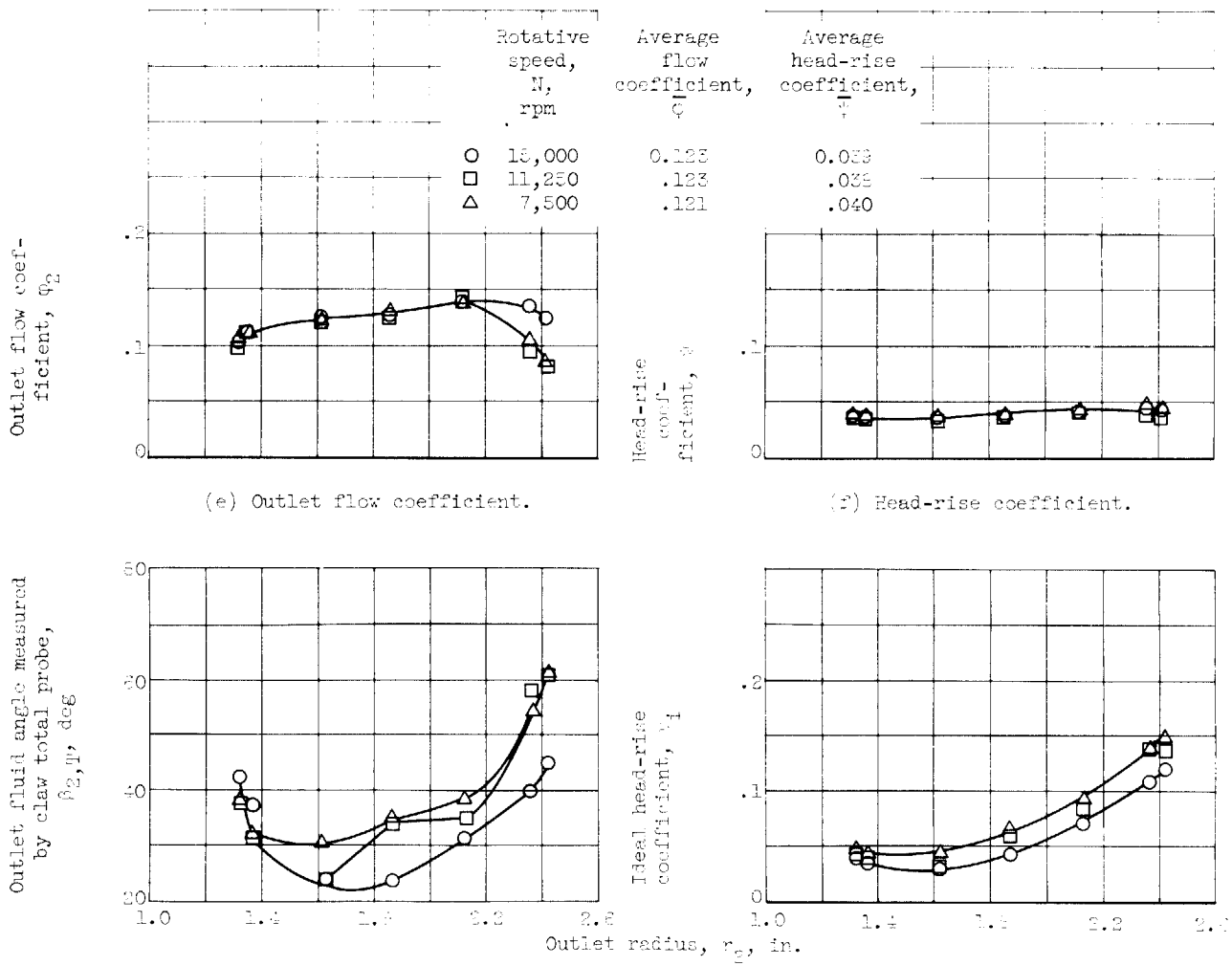

(e) Outlet flow coefficient.

(f) Head-rise coefficient.

(g) Outlet flow angle.

(h) Ideal head-rise coefficient.

Figure 15. - Continued. Effect of rotor speed on blade-element performance in high flow operating region. Average flow coefficient, 0.122; normalized net positive suction head, 160 feet; average cavitation number, 0.082.

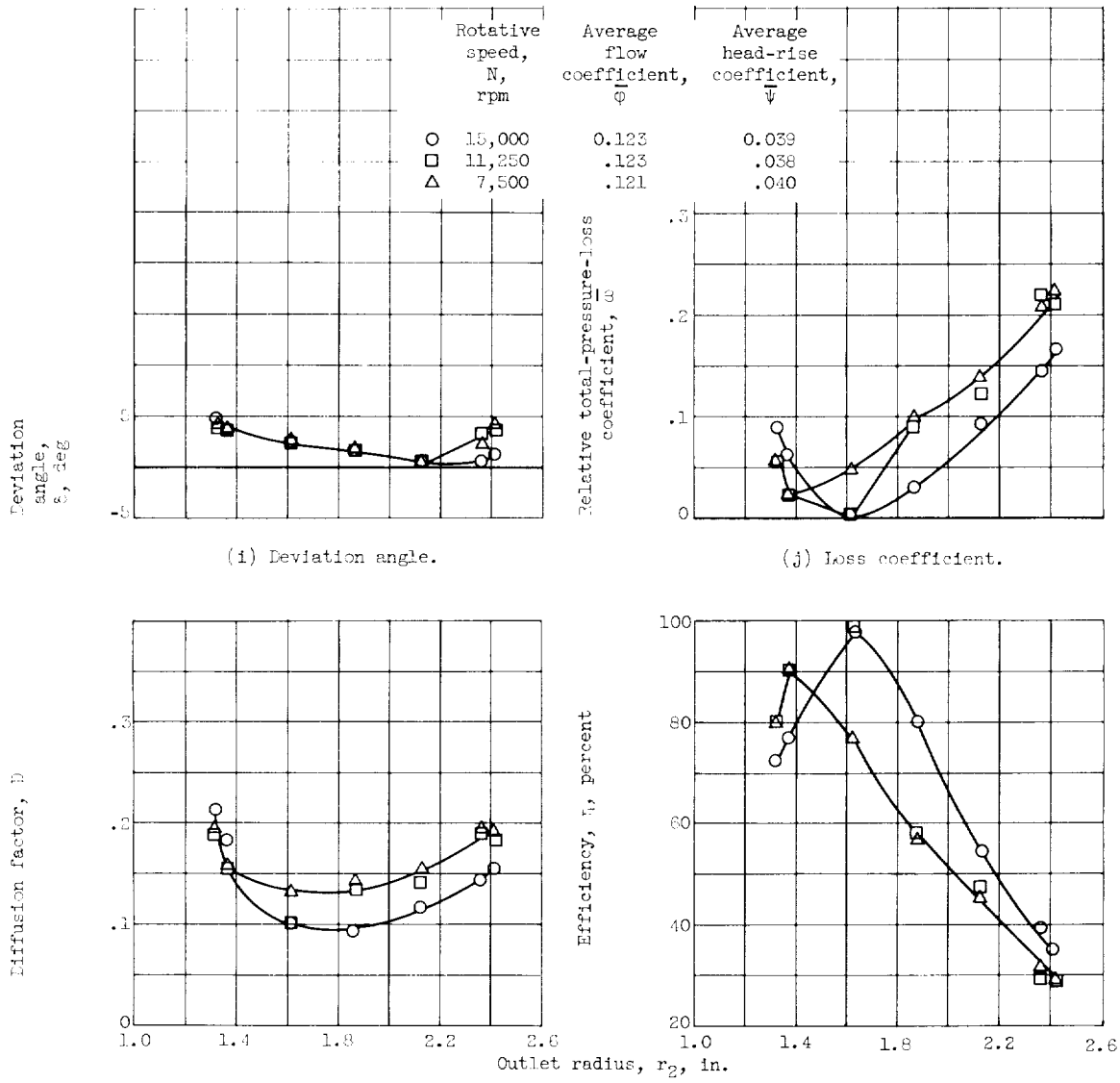

(i) Deviation angle.

(j) Loss coefficient.

(k) Diffusion factor.

(l) Efficiency.

Figure 15. - Concluded. Effect of rotor speed on blade-element performance in high flow operating region. Average flow coefficient, 0.122; normalized net positive suction head, 180 feet; average cavitation number, 0.082.

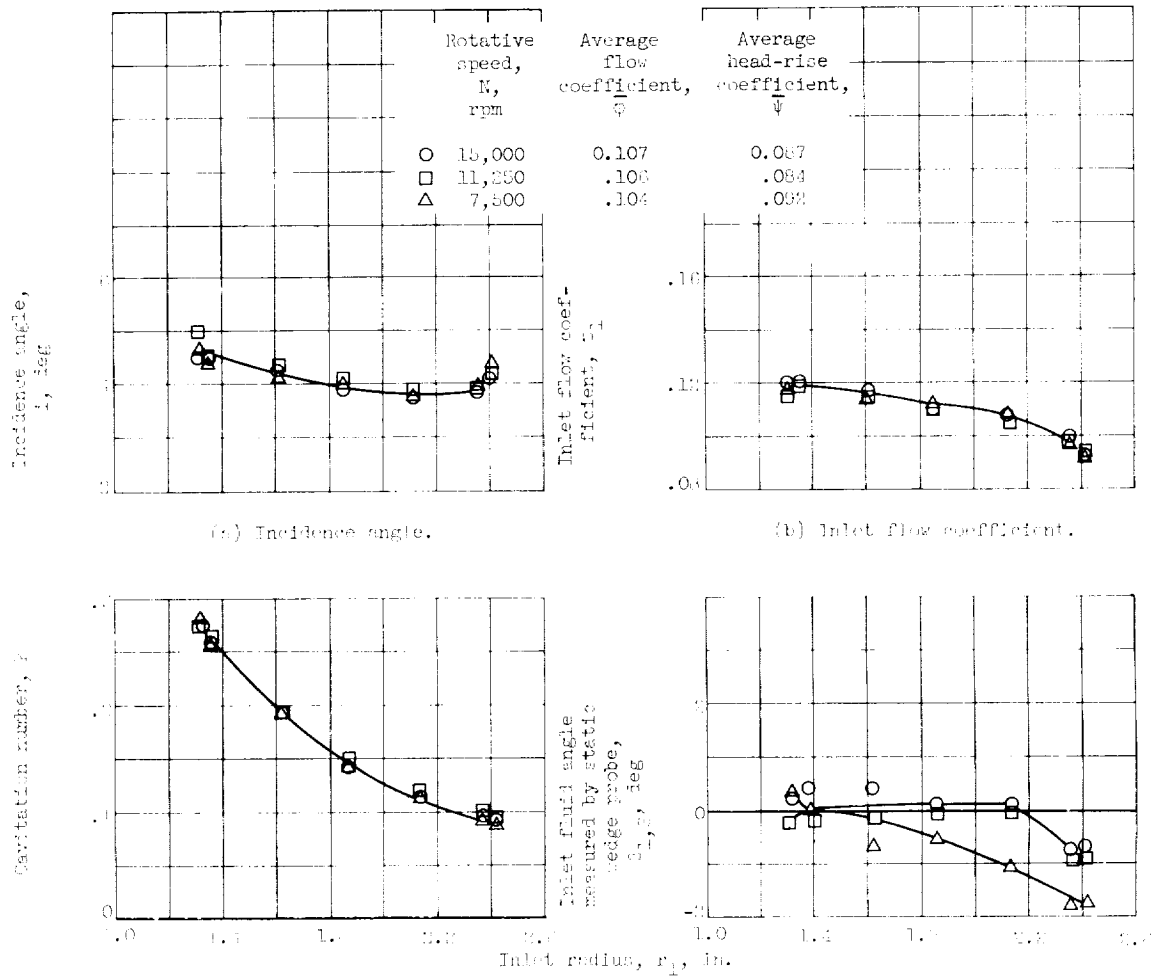

Figure 14. - Effect of rotor speed on blade-element performance in mean flow operating region. Average flow coefficient, 0.106; normalized net positive suction head, 160 feet; average cavitation number, 0.080.

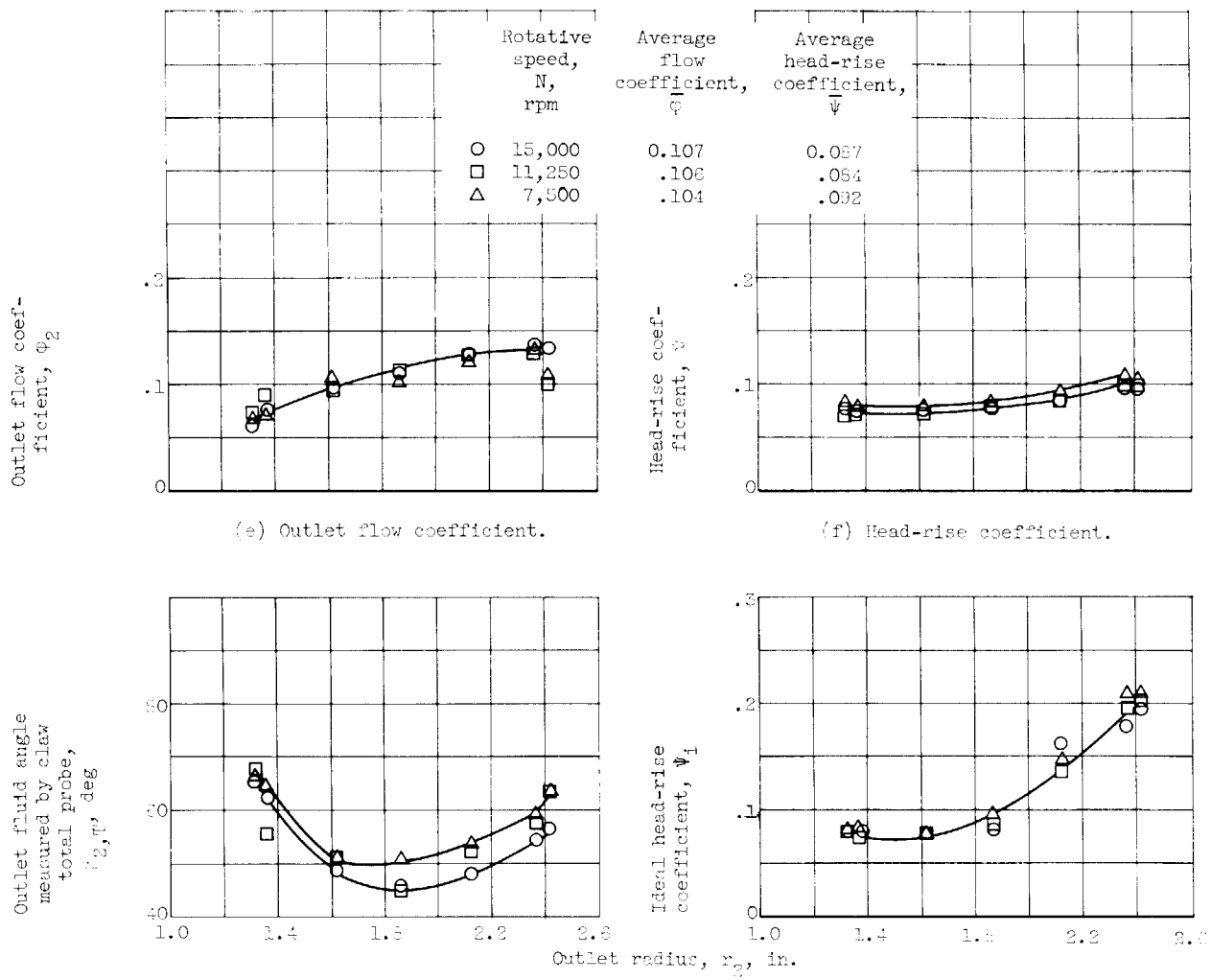

(e) Outlet flow coefficient.

(f) Head-rise coefficient.

(g) Outlet flow angle.

(h) Ideal head-rise coefficient.

Figure 14. - Continued. Effect of rotor speed on blade-element performance in mean flow operating region. Average flow coefficient, 0.108; normalized net positive suction head, 140 feet; average cavitation number, 0.030.

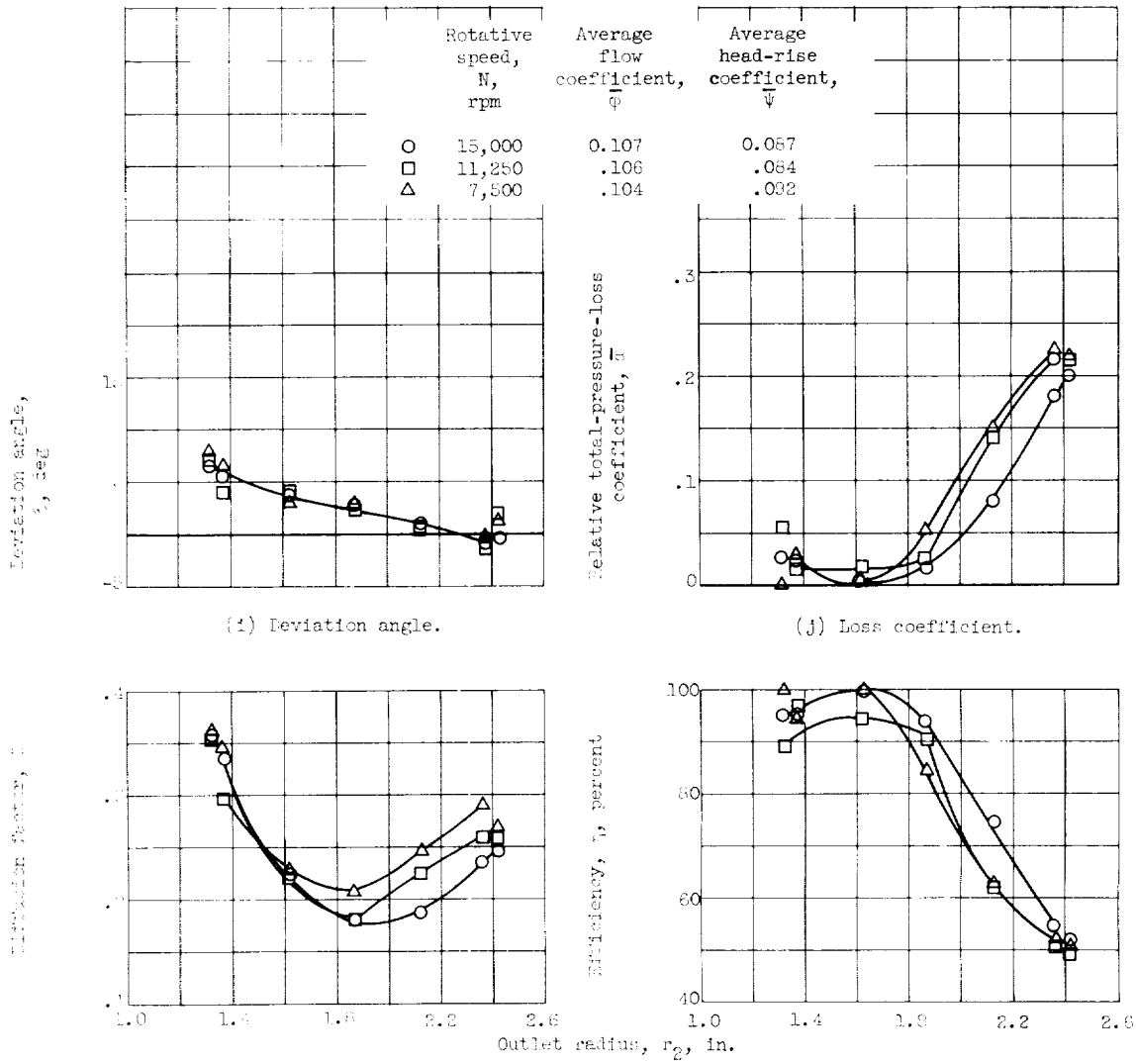

(i) Deviation angle.

(j) Loss coefficient.

(k) Diffusion factor.

(l) Efficiency.

Figure 14. - Concluded. Effect of rotor speed on blade-element performance in mean flow operating region. Average flow coefficient, 0.100; normalized net positive suction head, 100 feet; average cavitation number, 0.086.

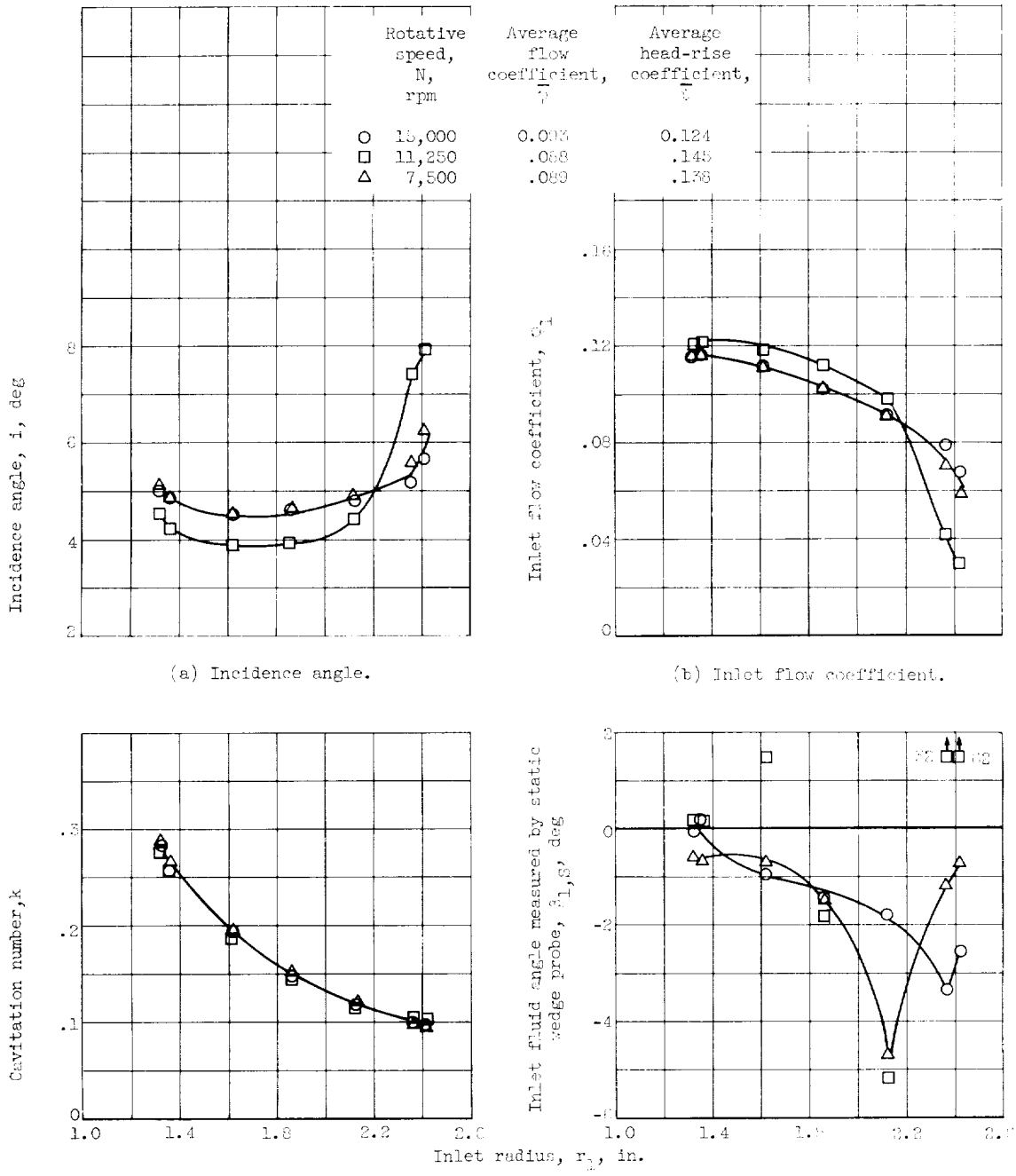

(a) Incidence angle.

(b) Inlet flow coefficient.

(c) Cavitation number.

(d) Inlet flow angle.

Figure 15. - Effect of rotor speed on blade-element performance in low flow operating region. Average flow coefficient, 0.090; normalized net positive suction head, 100 feet; average cavitation number, 0.083.

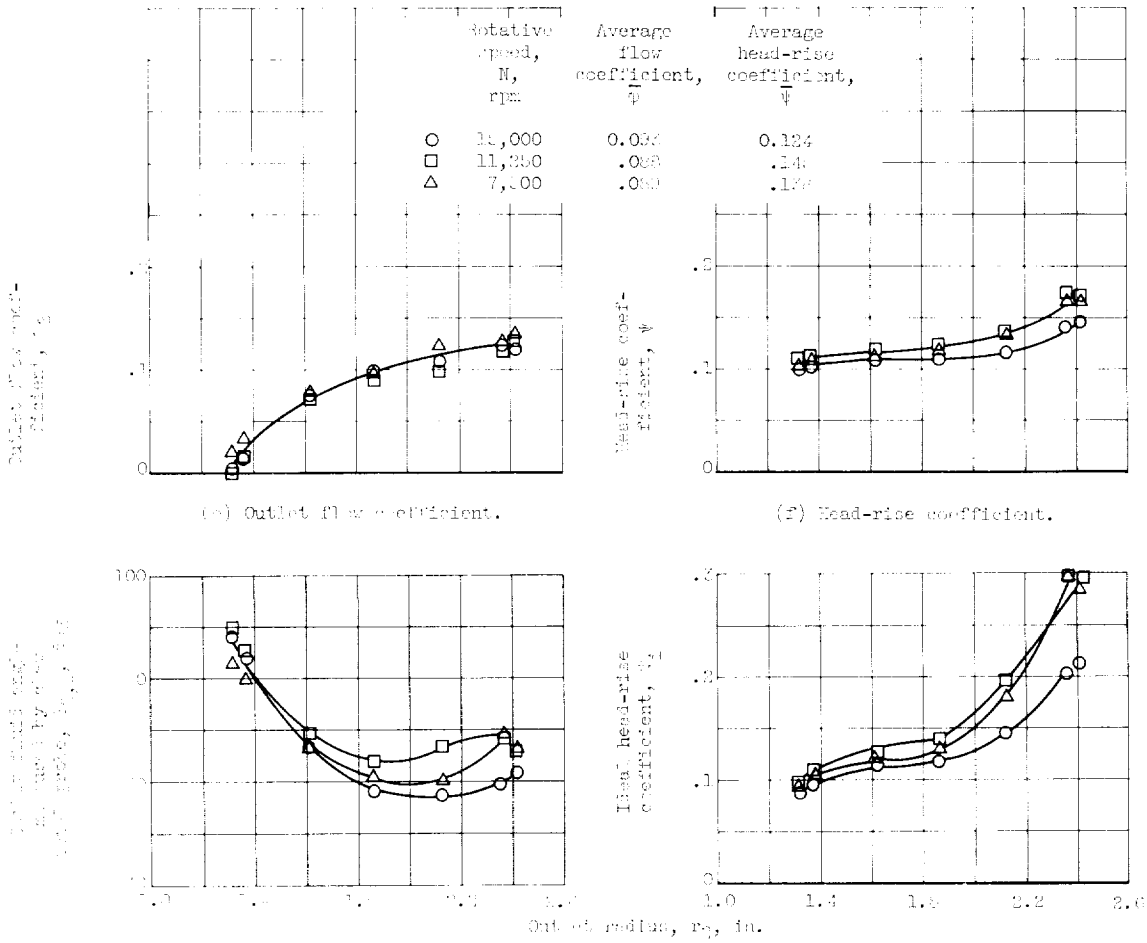

(e) Outlet flow coefficient.

(f) Head-rise coefficient.

(g) Outlet flow angle.

(h) Ideal head-rise coefficient.

Figure 1. - Continued. Effect of rotor speed on blade-element performance in low flow operating region. Average flow coefficient, 0.030; normalized net positive suction head, 150 feet; average cavitation number, 0.080.

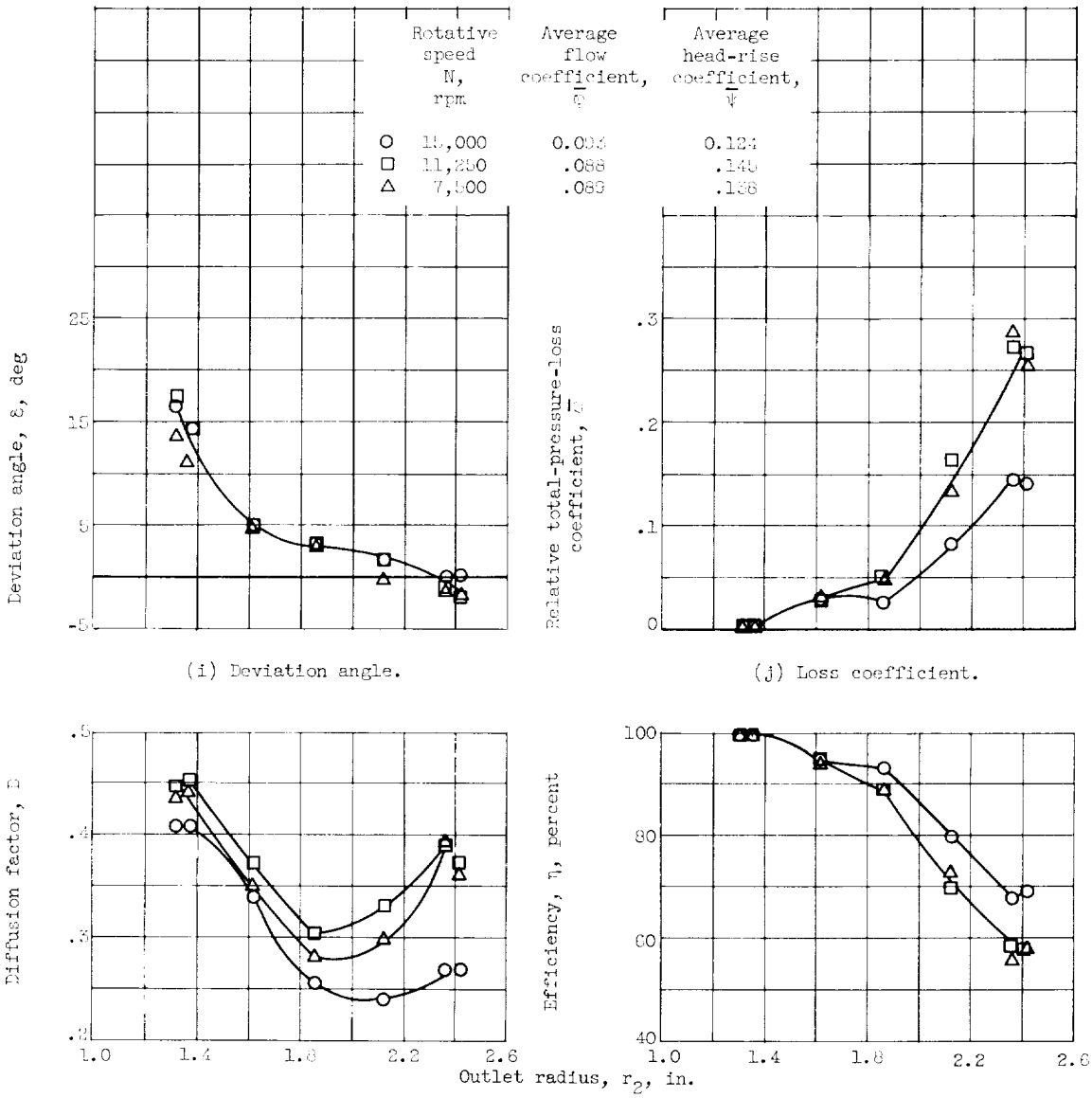

(i) Deviation angle.

(j) Loss coefficient.

(k) Diffusion factor.

(l) Efficiency.

Figure 15. - Concluded. Effect of rotor speed on blade-element performance in low flow operating region. Average flow coefficient, 0.090; normalized net positive suction head, 160 feet; average cavitation number, 0.088.

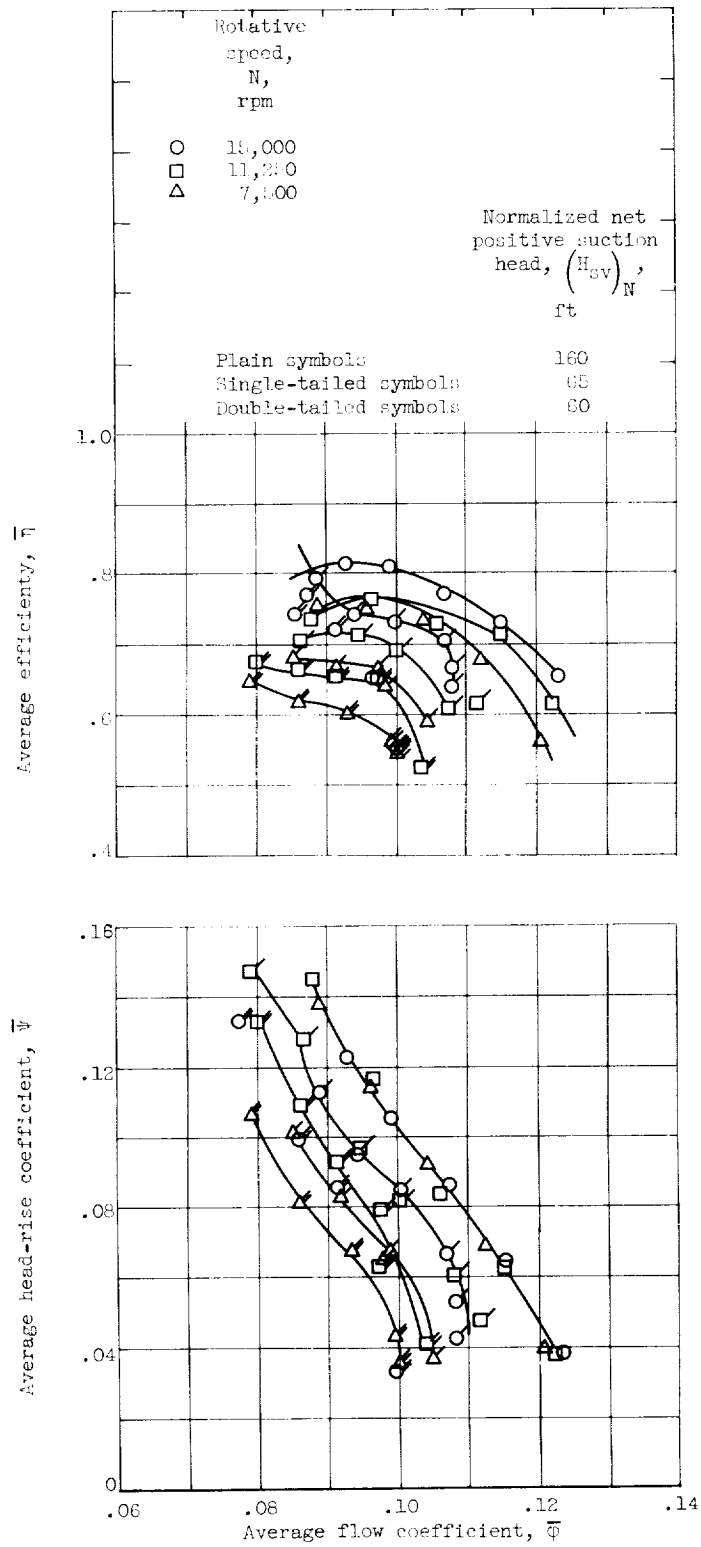

Figure 16. - Overall performance at three blade speeds (cavitating and noncavitating).

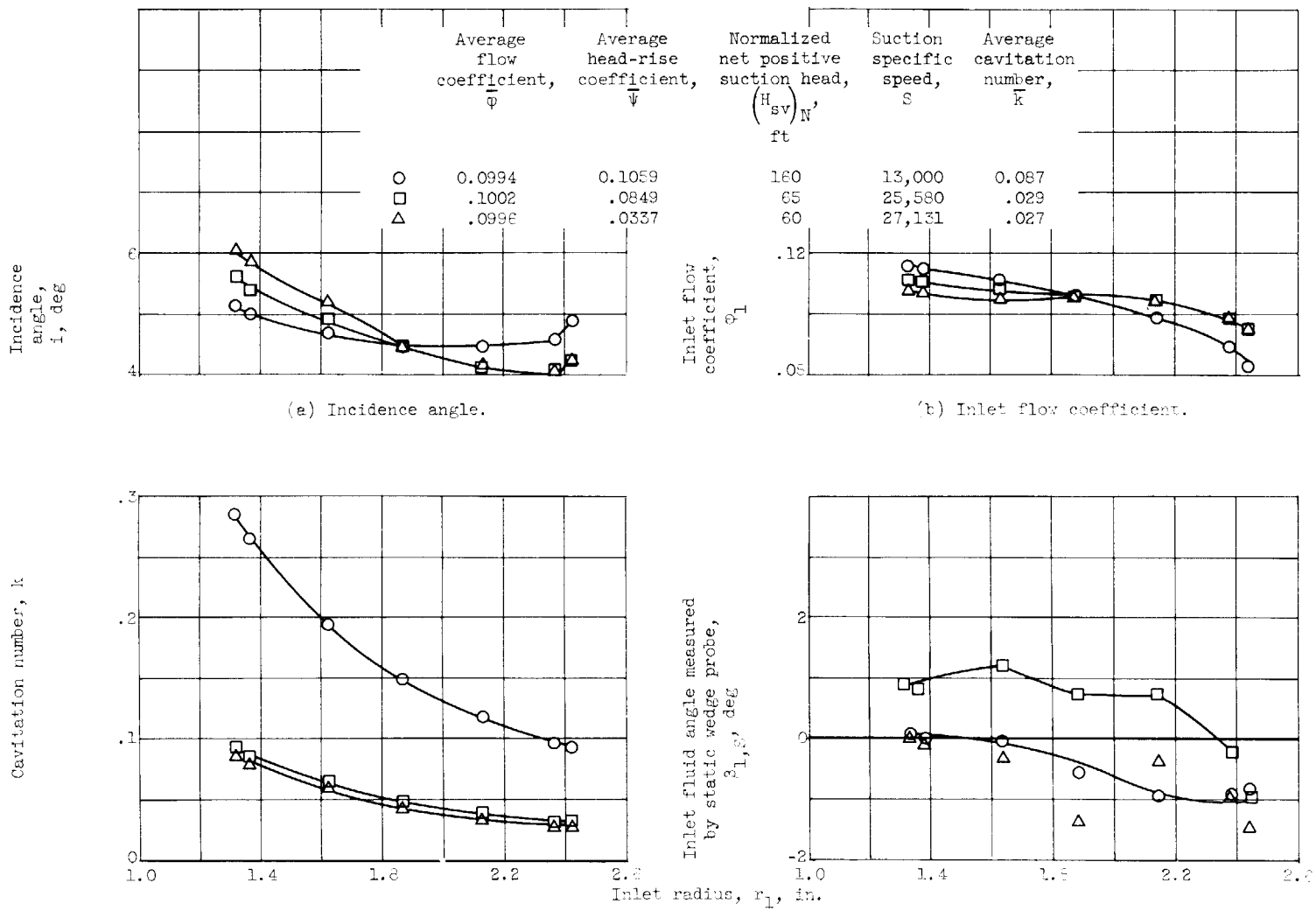

(a) Incidence angle.

(b) Inlet flow coefficient.

(c) Cavitation number.

(d) Inlet flow angle.

Figure 17. - Effect of normalized net positive suction head on blade-element performance. Rotative speed, 15,000 rpm.

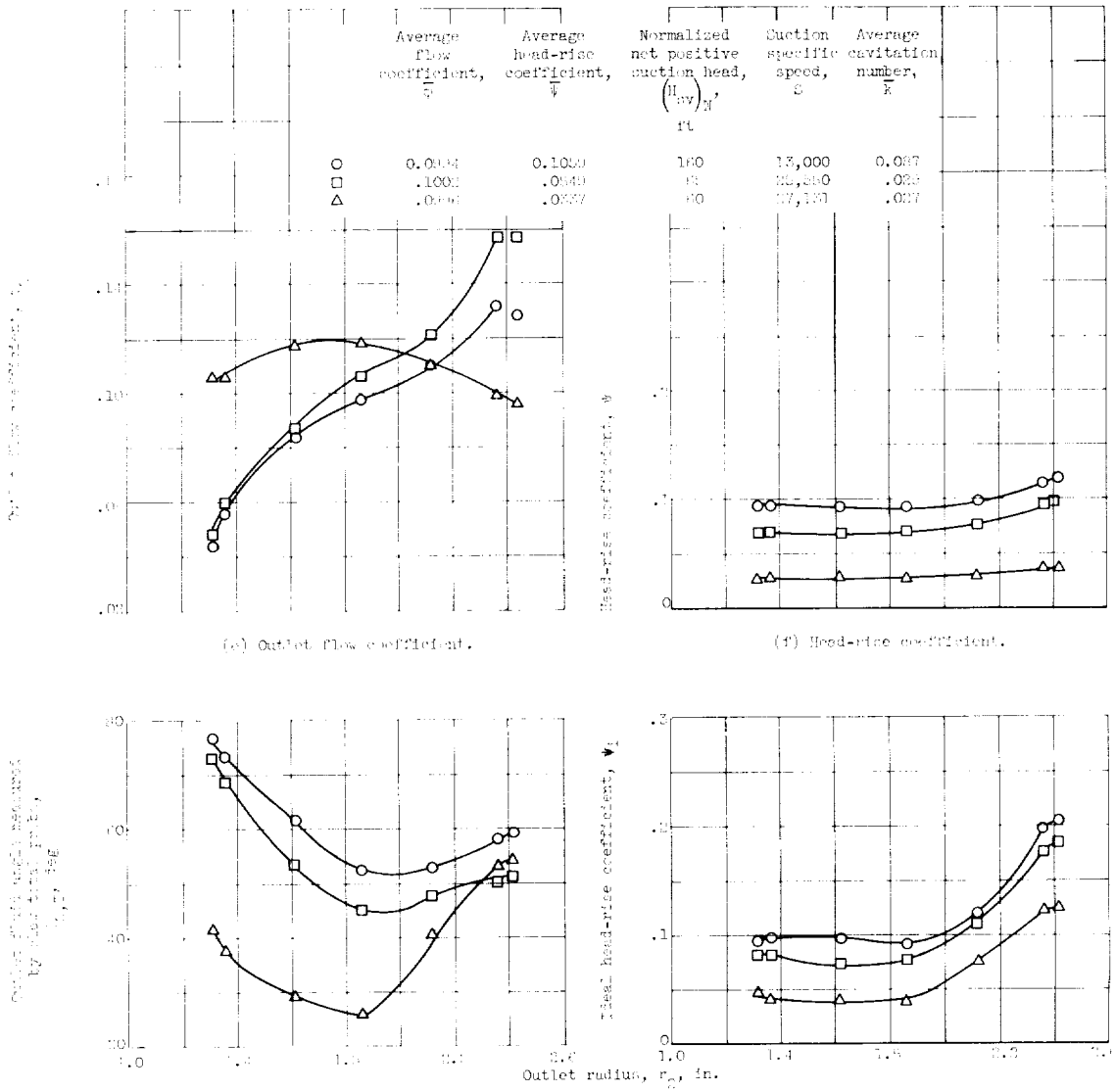

(e) Outlet flow coefficient.

(f) Head-rise coefficient.

(g) Outlet flow angle.

(h) Ideal head-rise coefficient.

Figure 7. - Continued. Effect of normalized net positive suction head on blade-element performance. Rotative speed, 15,000 rpm.

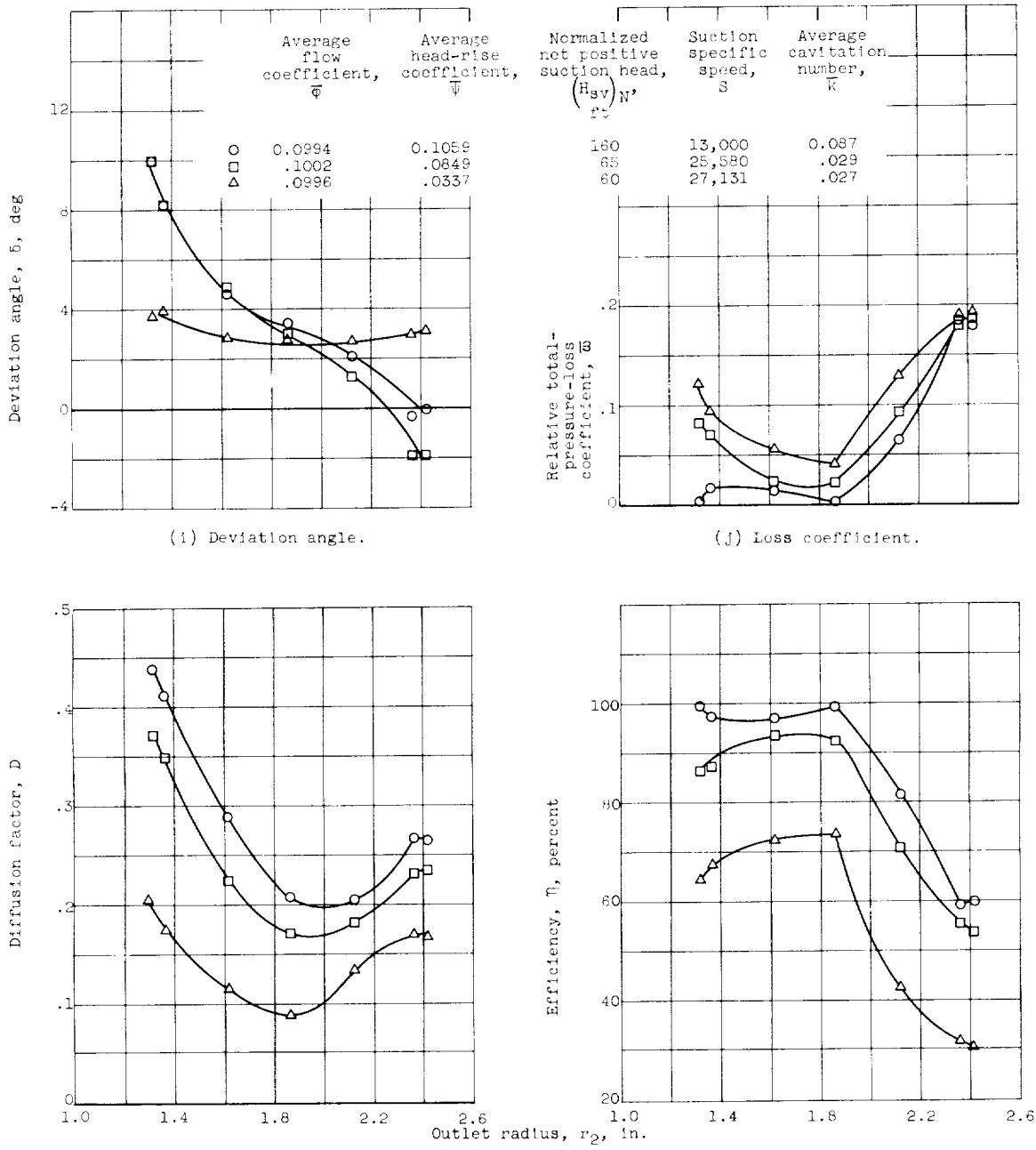

(i) Deviation angle.

(j) Loss coefficient.

(k) Diffusion factor.

(l) Efficiency.

Figure 17. - Concluded. Effect of normalized net positive suction head on blade-element performance. Rotative speed, 15,000 rpm.

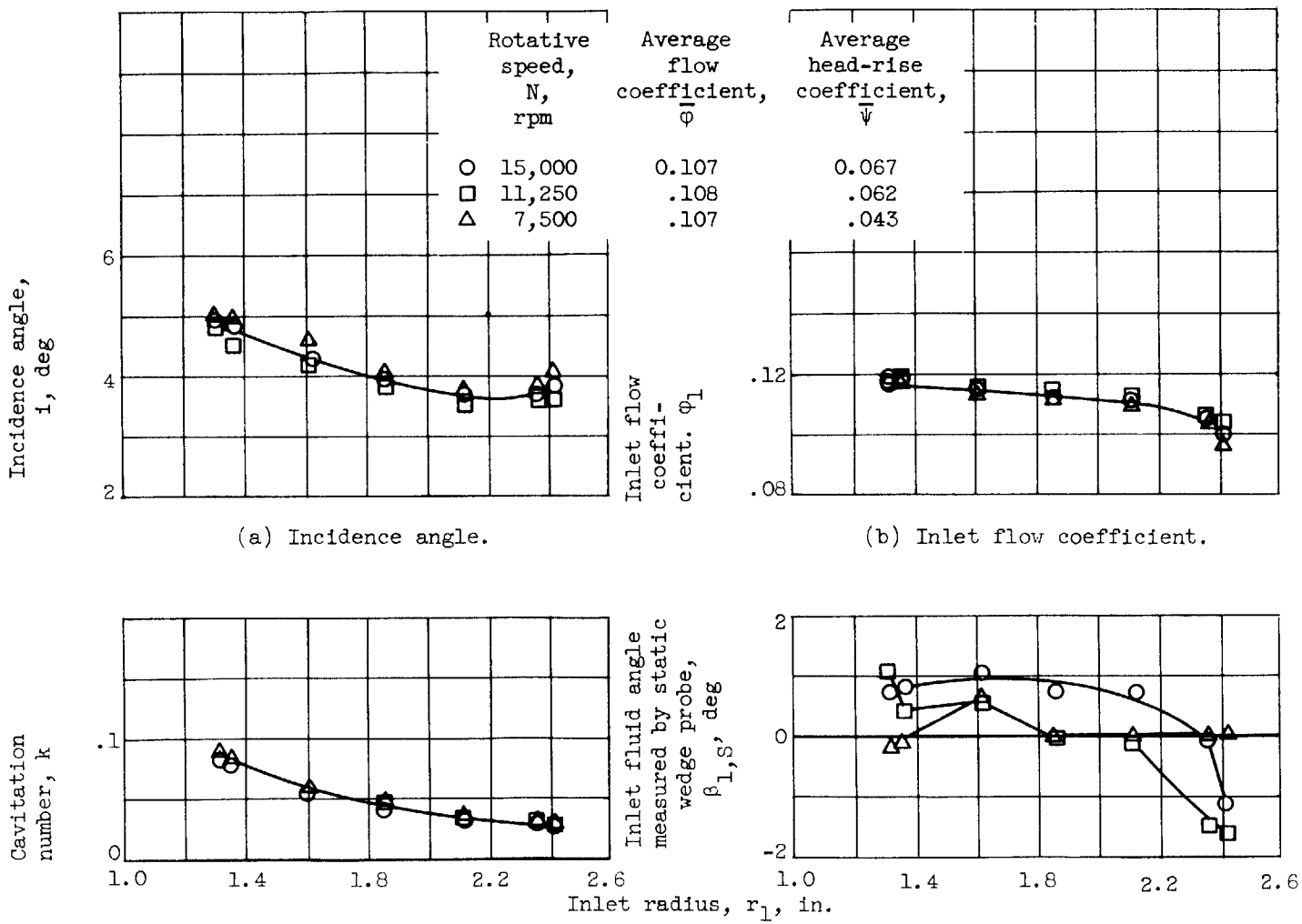

(a) Incidence angle.

(b) Inlet flow coefficient.

(c) Cavitation number.

(d) Inlet flow angle.

Figure 18. - Effect of rotor speed on blade-element performance. Average flow coefficient, 0.11; normalized net positive suction head, 65 feet; average cavitation number, 0.028.

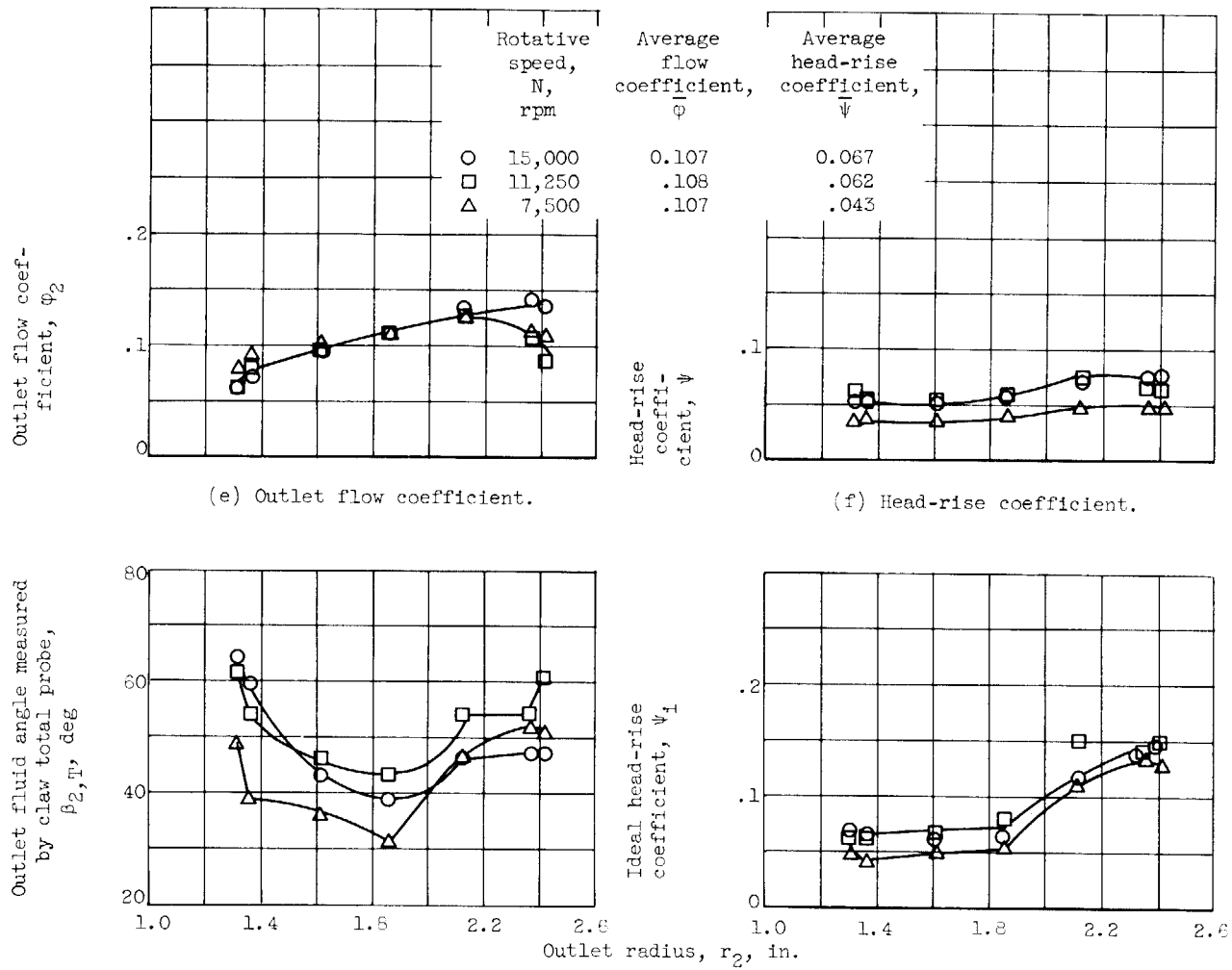

(e) Outlet flow coefficient.

(f) Head-rise coefficient.

(g) Outlet flow angle.

(h) Ideal head-rise coefficient.

Figure 18. - Continued. Effect of rotor speed on blade-element performance. Average flow coefficient, 0.11; normalized net positive suction head, 65 feet; average cavitation number, 0.028.

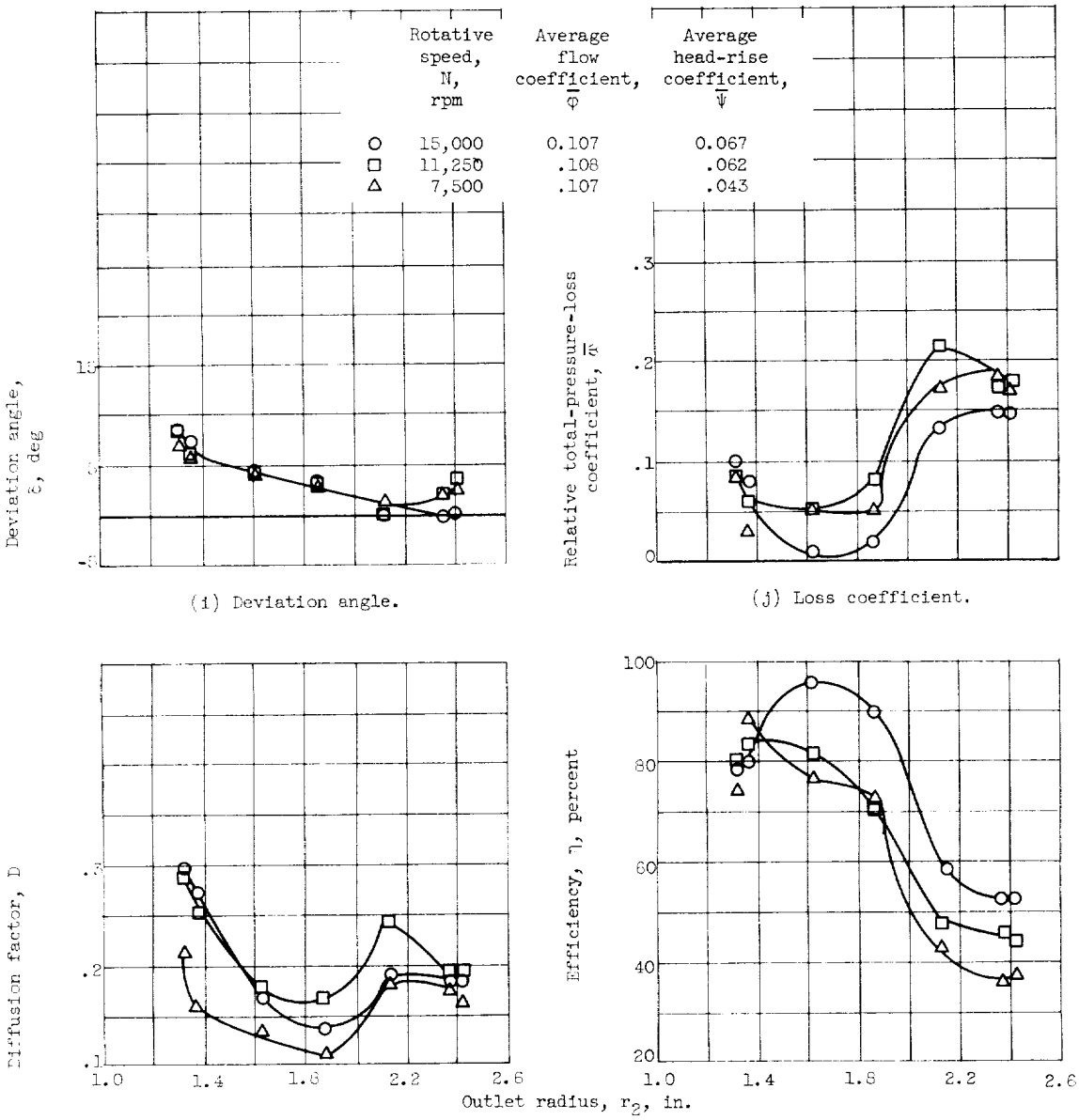

(i) Deviation angle.

(j) Loss coefficient.

(k) Diffusion factor.

(l) Efficiency.

Figure 18. - Concluded. Effect of rotor speed on blade-element performance. Average flow coefficient, 0.11; normalized net positive suction head, 65 feet; average cavitation number, 0.028.

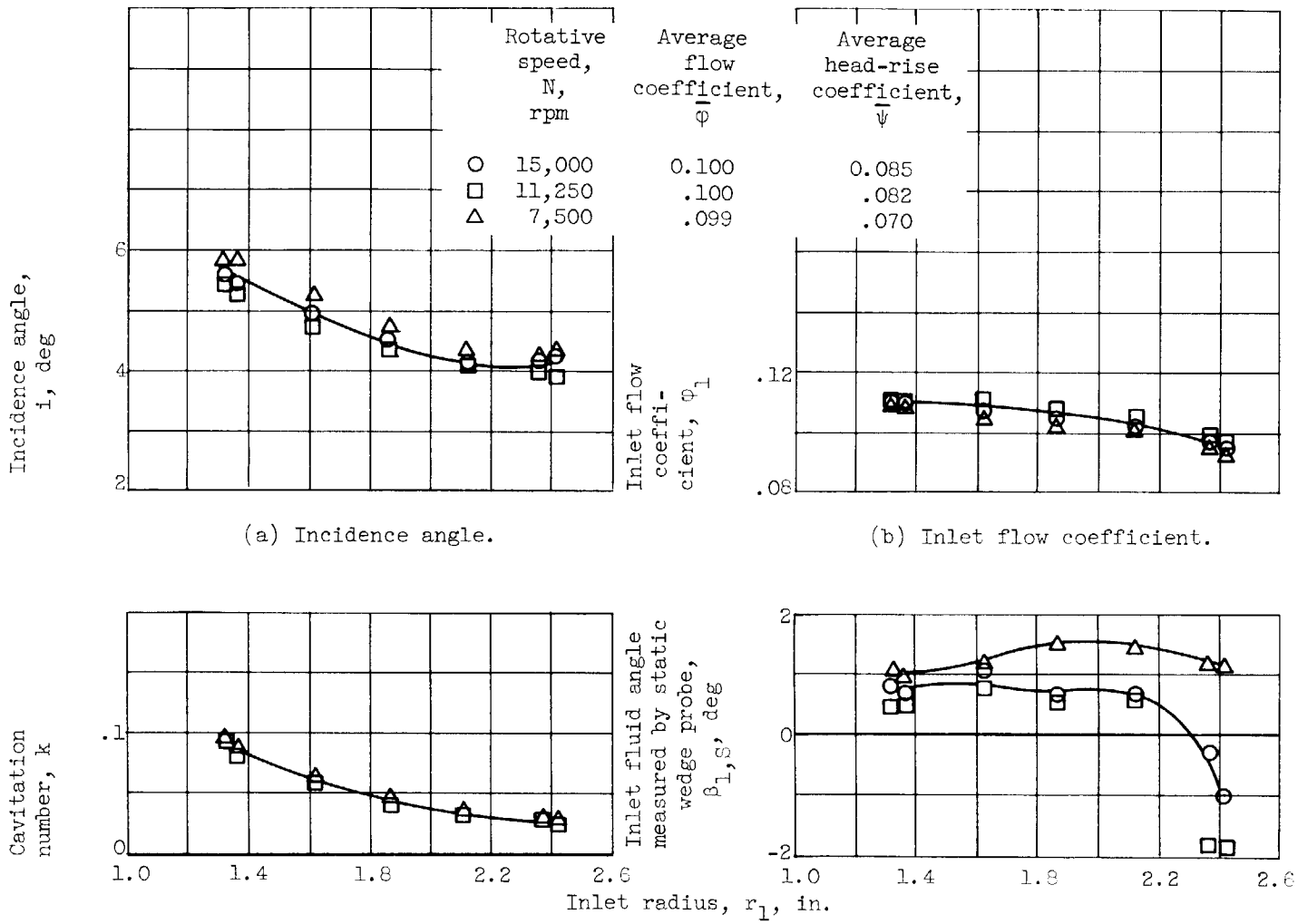

(a) Incidence angle.

(b) Inlet flow coefficient.

(c) Cavitation number.

(d) Inlet flow angle.

Figure 19. - Effect of rotor speed on blade-element performance. Average flow coefficient, 0.10; normalized net positive suction head, 65 feet; average cavitation number, 0.029.

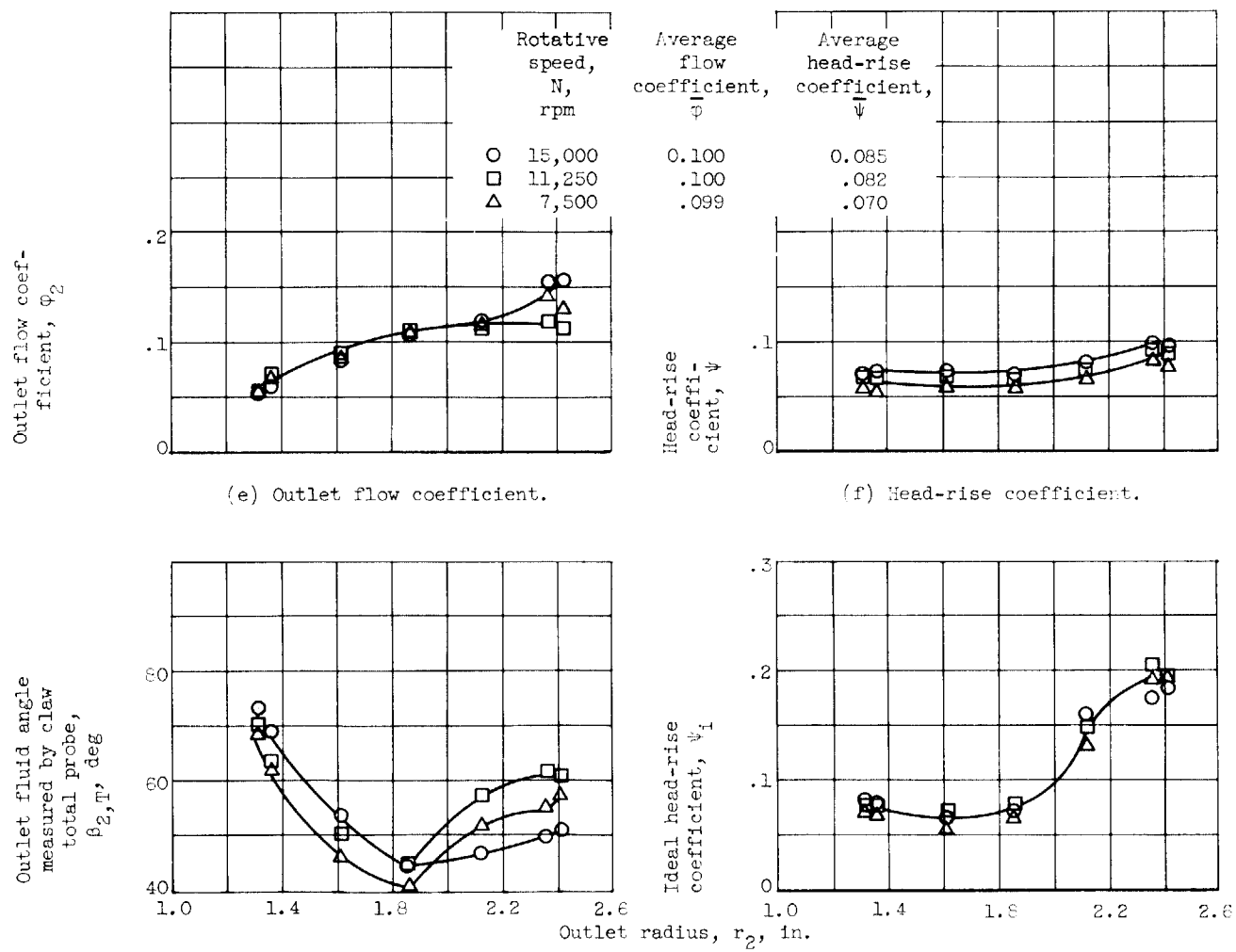

(e) Outlet flow coefficient.

(f) Head-rise coefficient.

(g) Outlet flow angle.

(h) Ideal head-rise coefficient.

Figure 19. - Continued. Effect of rotor speed on blade-element performance. Average flow coefficient, 0.10; normalized net positive suction head, 65 feet; average cavitation number, 0.029.

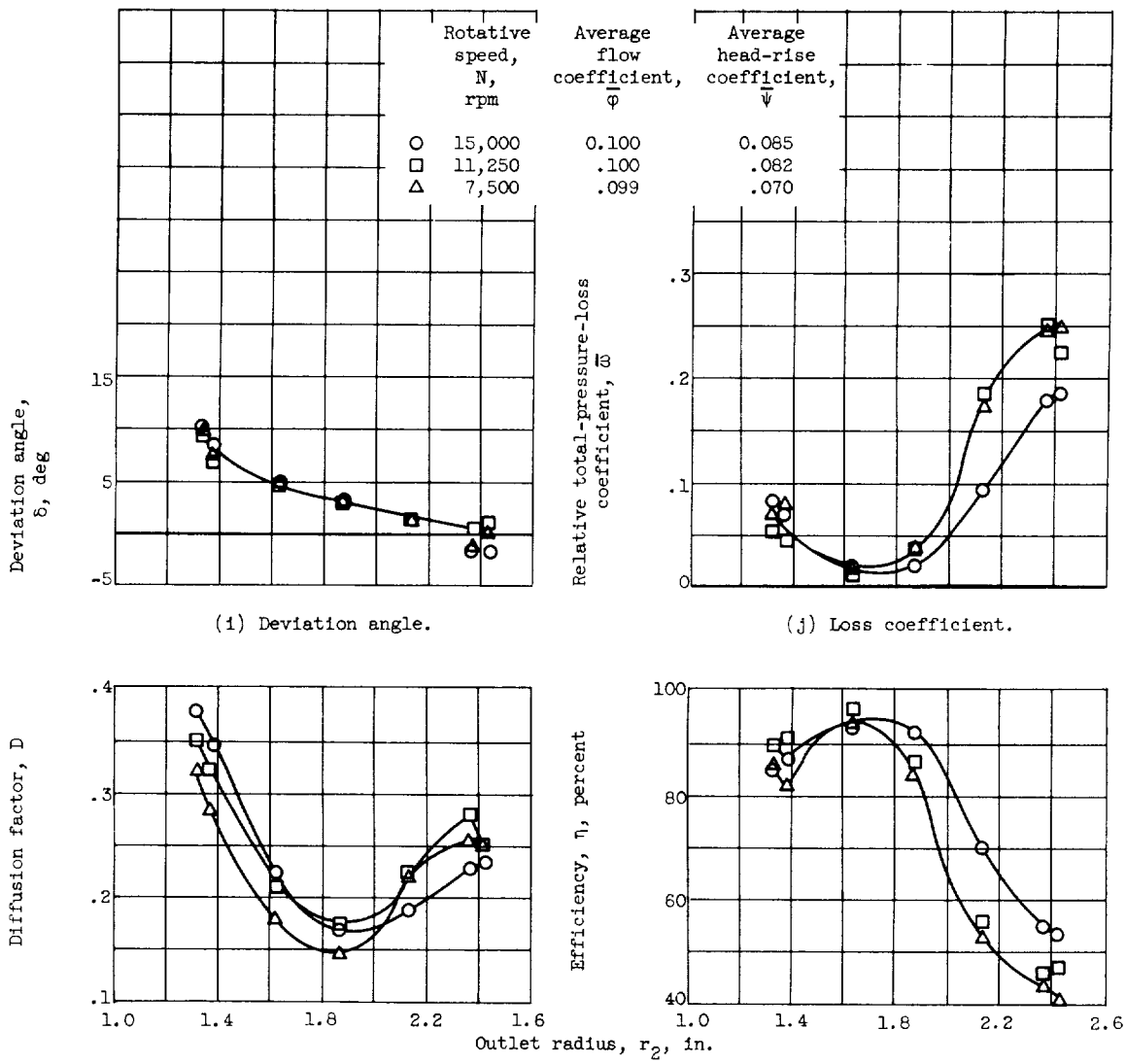

(i) Deviation angle.

(j) Loss coefficient.

(k) Diffusion factor.

(l) Efficiency.

Figure 19. - Concluded. Effect of rotor speed on blade-element performance. Average flow coefficient, 0.10; normalized net positive suction head, 65 feet; average cavitation number, 0.029.

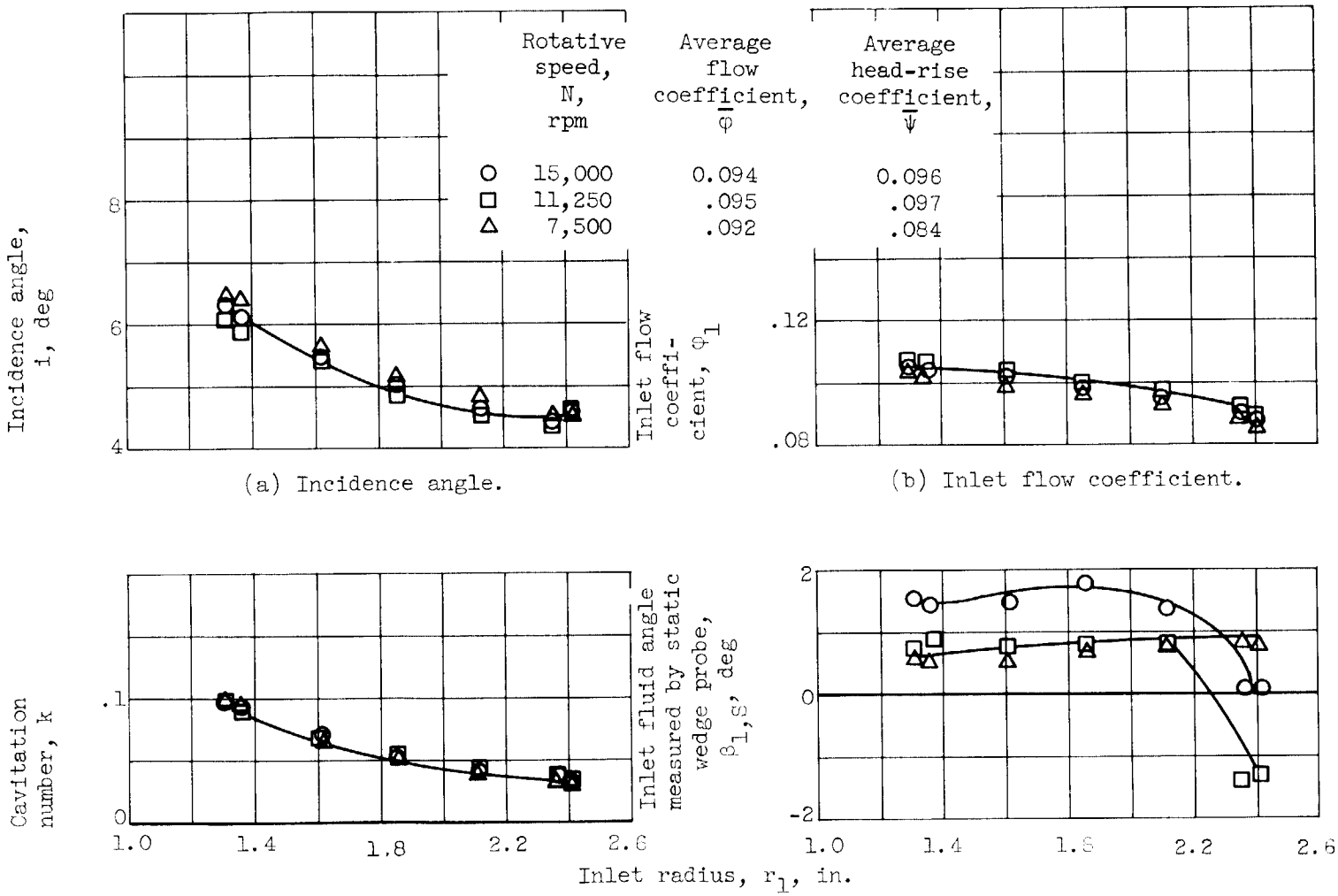

(a) Incidence angle.

(b) Inlet flow coefficient.

(c) Cavitation number.

(d) Inlet flow angle.

Figure 20. - Effect of rotor speed on blade-element performance. Average flow coefficient, 0.095; normalized net positive suction head, 85 feet; average cavitation number, 0.030.

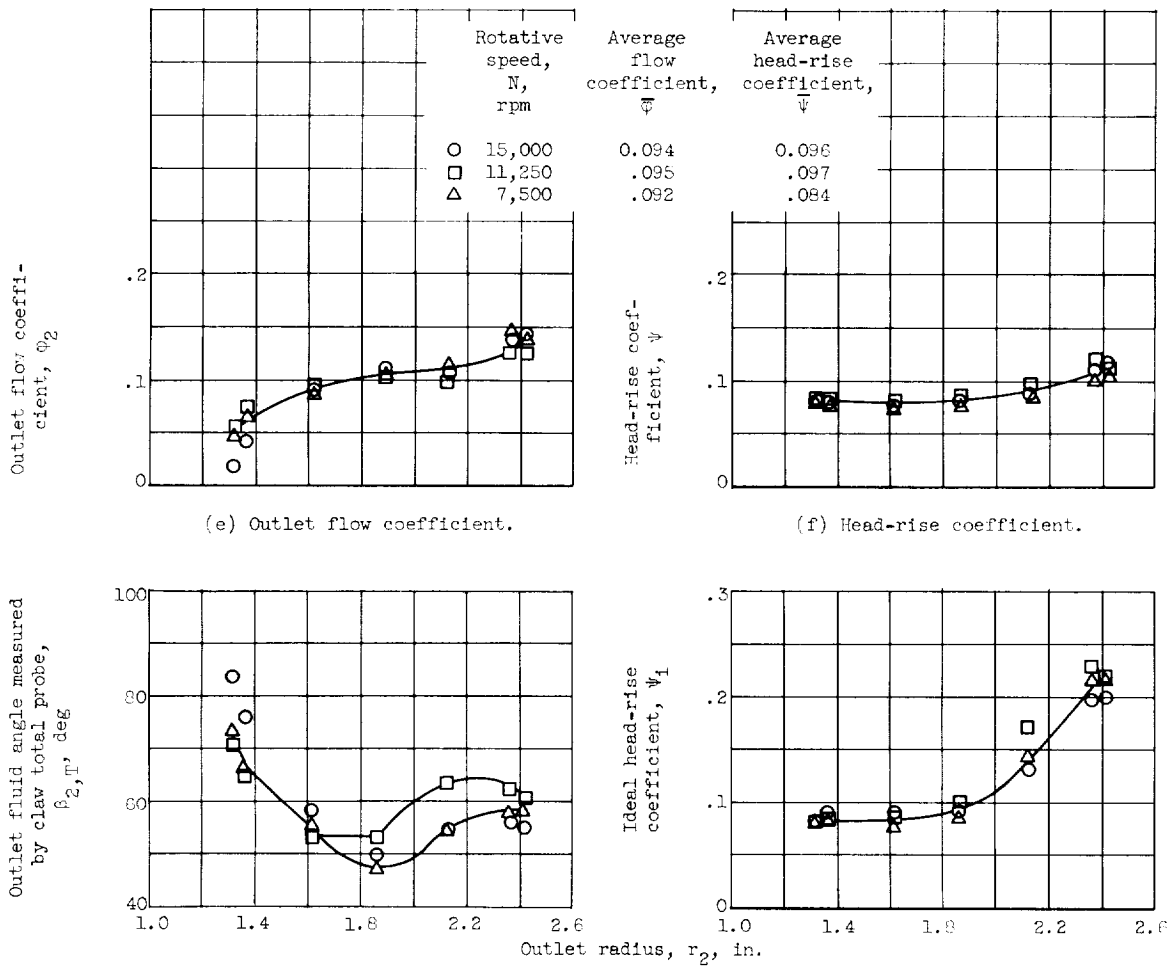

(e) Outlet flow coefficient.

(f) Head-rise coefficient.

(g) Outlet flow angle.

(h) Ideal head-rise coefficient.

Figure 20. - Continued. Effect of rotor speed on blade-element performance. Average flow coefficient, 0.095; normalized net positive suction head, 65 feet; average cavitation number, 0.030.

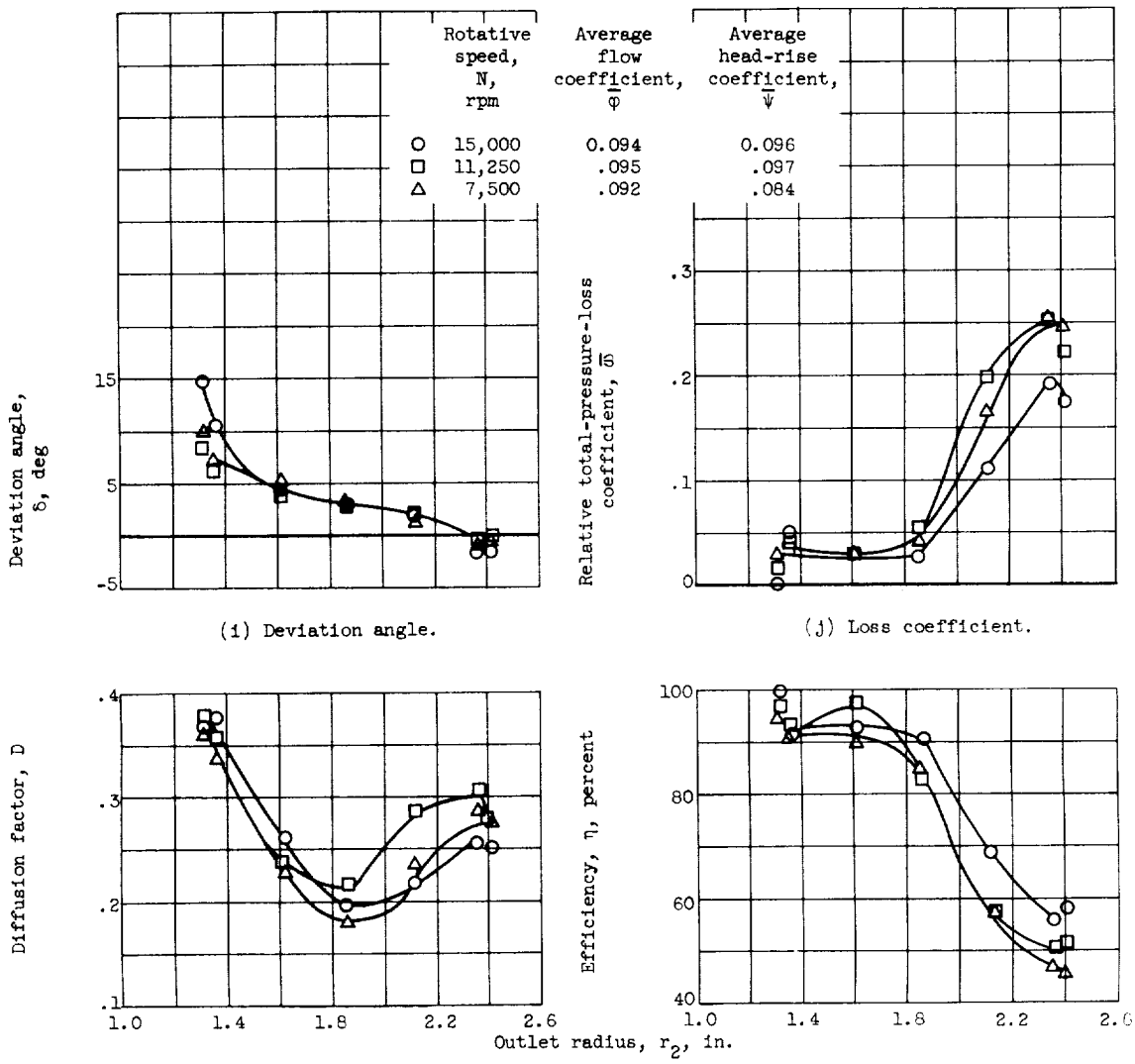

(i) Deviation angle.

(j) Loss coefficient.

(k) Diffusion factor.

(l) Efficiency.

Figure 20. - Concluded. Effect of rotor speed on blade-element performance. Average flow coefficient, 0.095; normalized net positive suction head, 65 feet; average cavitation number, 0.030.

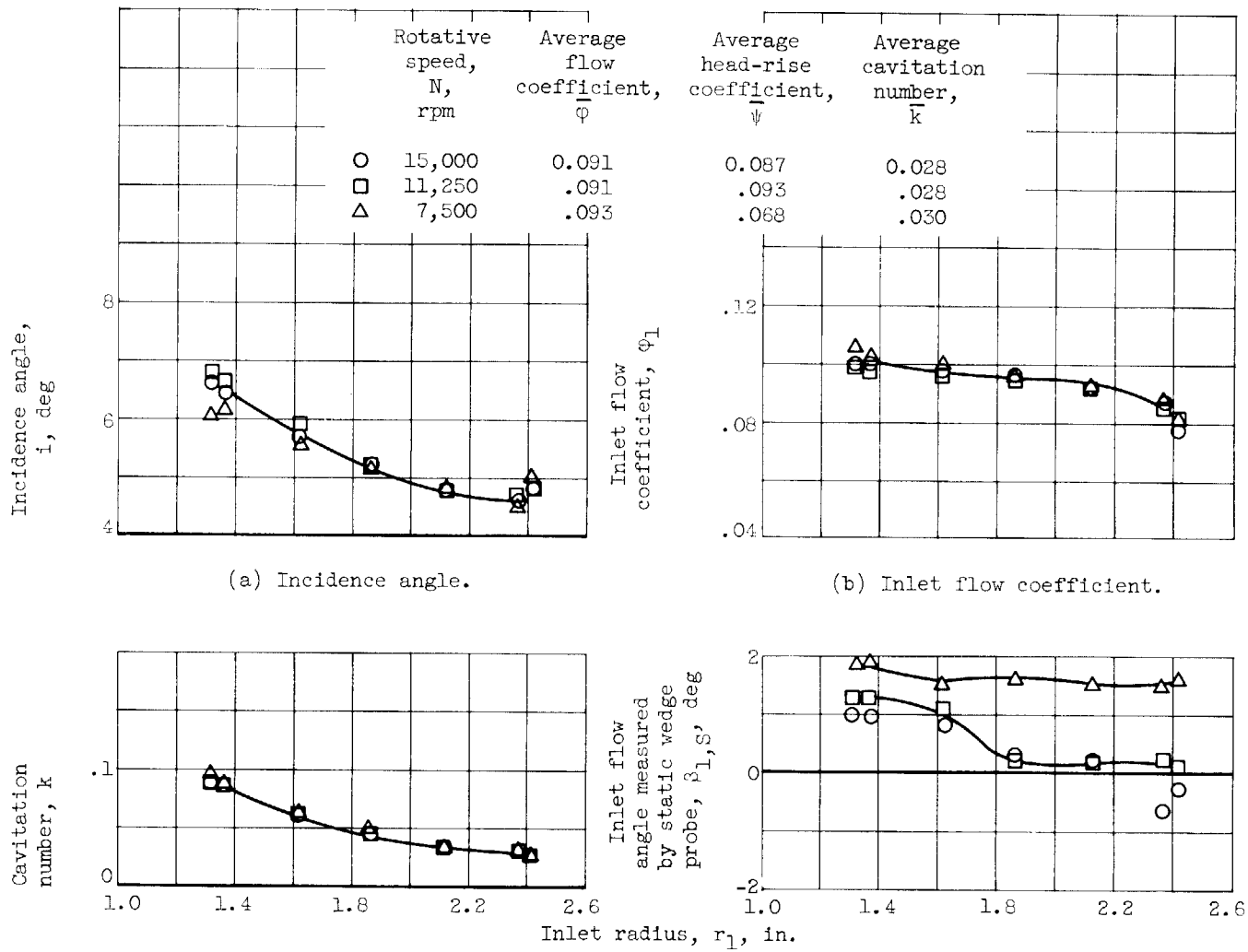

(a) Incidence angle.

(b) Inlet flow coefficient.

(c) Cavitation number.

(d) Inlet flow angle.

Figure 21. - Effect of speed on blade-element performance. Average flow coefficient, 0.090; normalized net positive suction head, 60 feet.

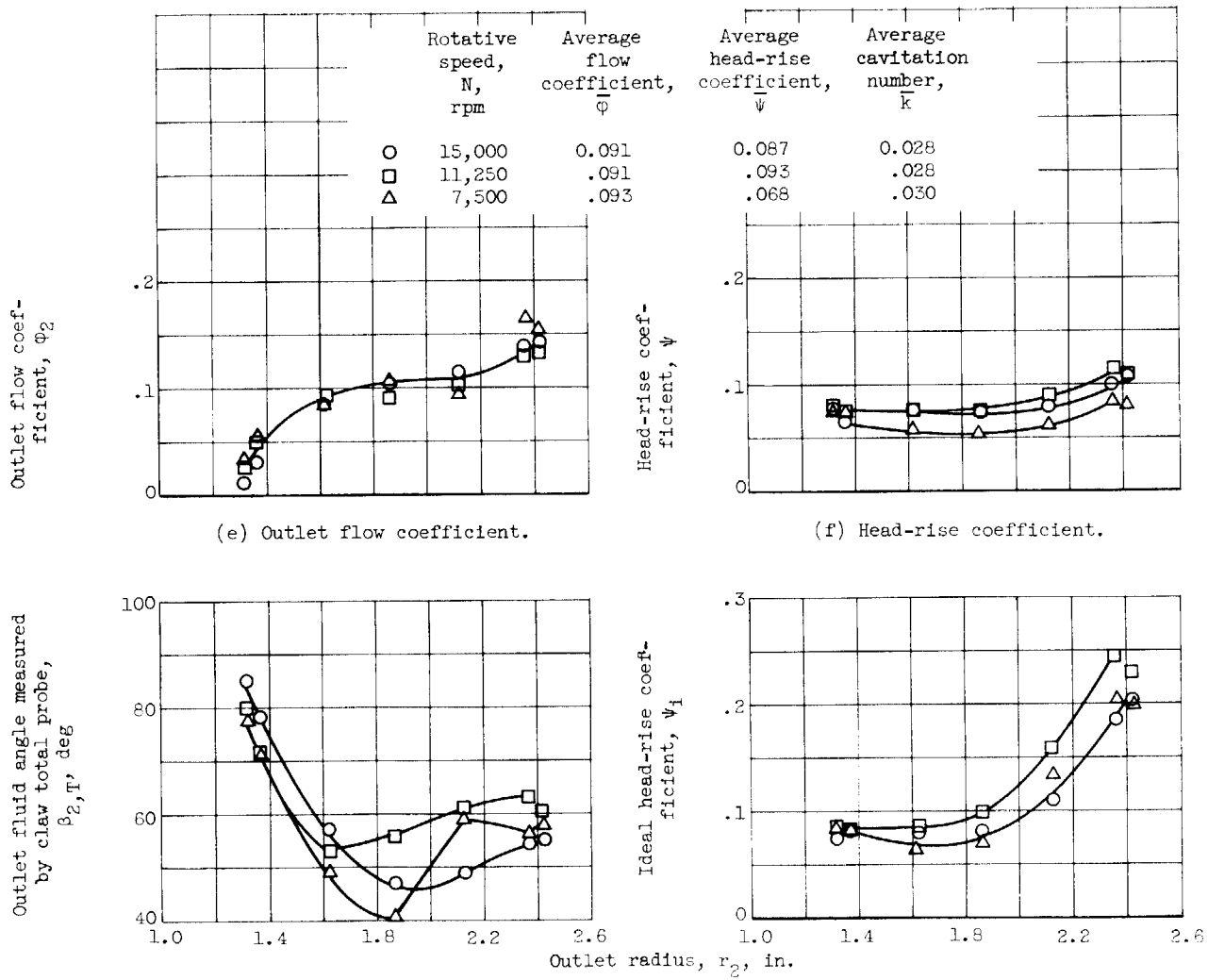

(e) Outlet flow coefficient.

(f) Head-rise coefficient.

(g) Outlet flow angle.

(h) Ideal head-rise coefficient.

Figure 21. - Continued. Effect of speed on blade-element performance. Average flow coefficient, 0.090; normalized net positive suction head, 60 feet.

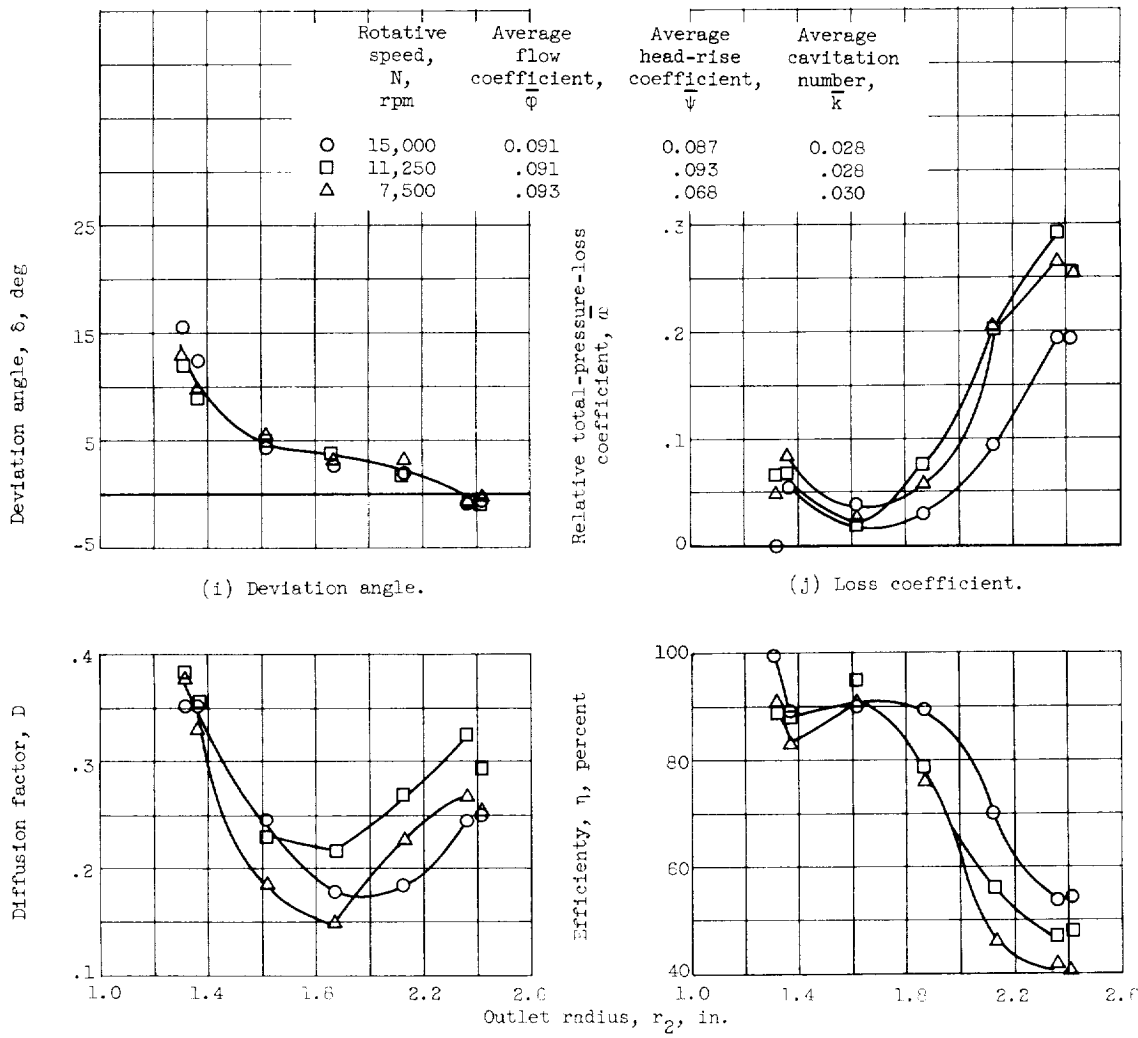

(i) Deviation angle.

(j) Loss coefficient.

(k) Diffusion factor.

(l) Efficiency.

Figure 21. - Concluded. Effect of speed on blade-element performance. Average flow coefficient, 0.090; normalized net positive suction head, 60 feet.

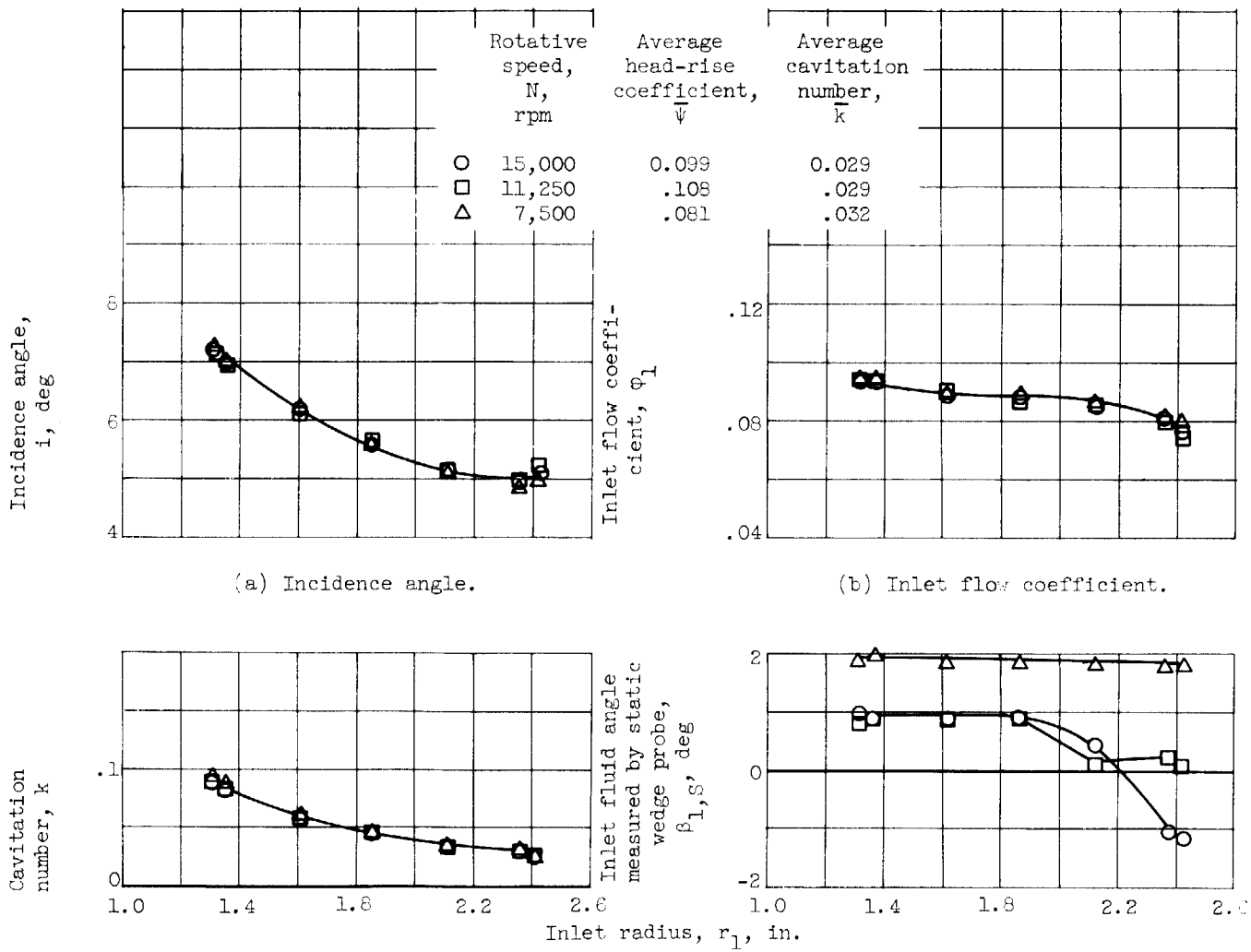

(a) Incidence angle.

(b) Inlet flow coefficient.

(c) Cavitation number.

(d) Inlet flow angle.

Figure 22. - Effect of rotor blade speed on blade-element performance. Average flow coefficient, 0.086; normalized net positive suction head, 60 feet.

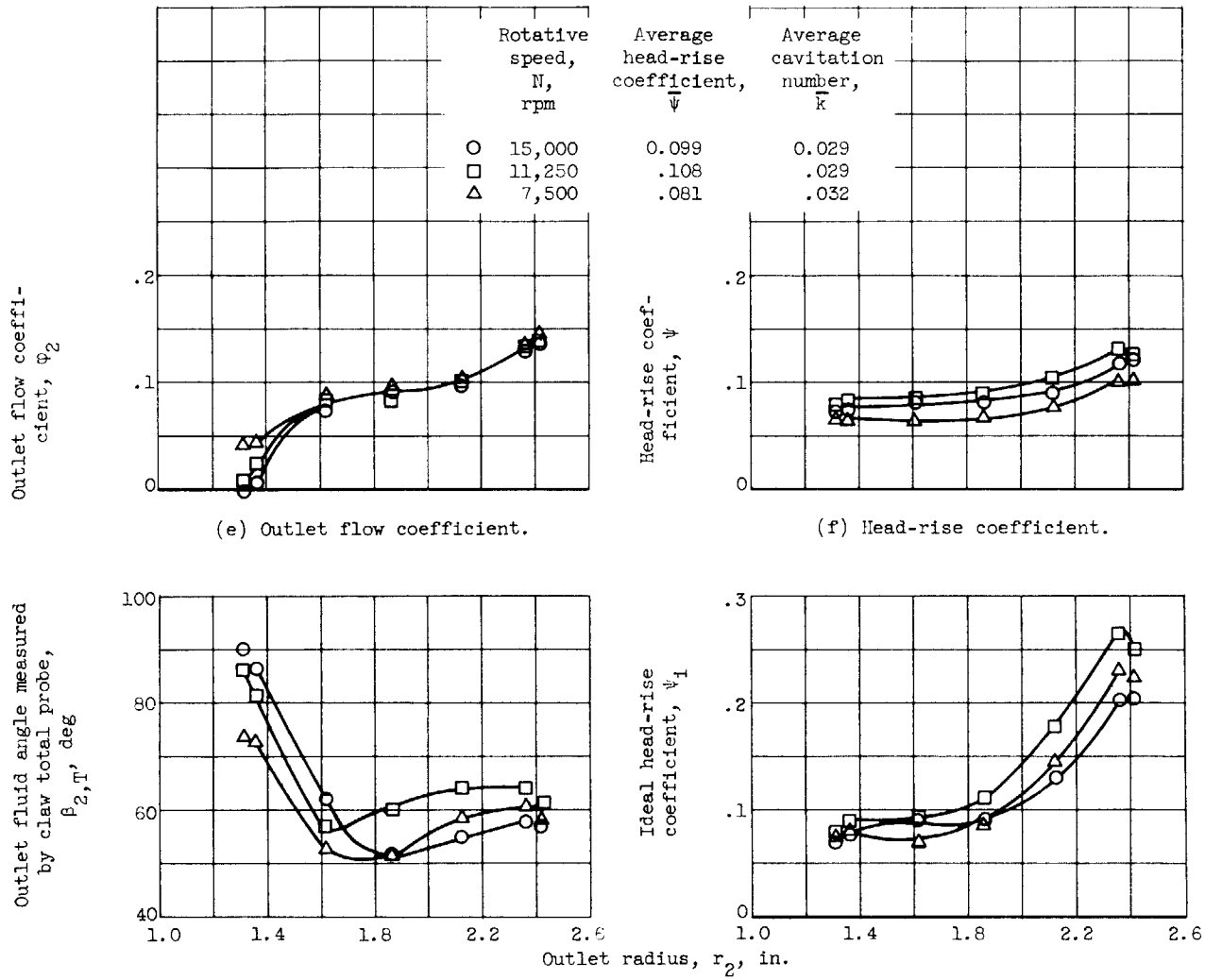

(e) Outlet flow coefficient.

(f) Head-rise coefficient.

(g) Outlet flow angle.

(h) Ideal head-rise coefficient.

Figure 22. - Continued. Effect of rotor blade speed on blade-element performance. Average flow coefficient, 0.086; normalized net positive suction head, 60 feet.

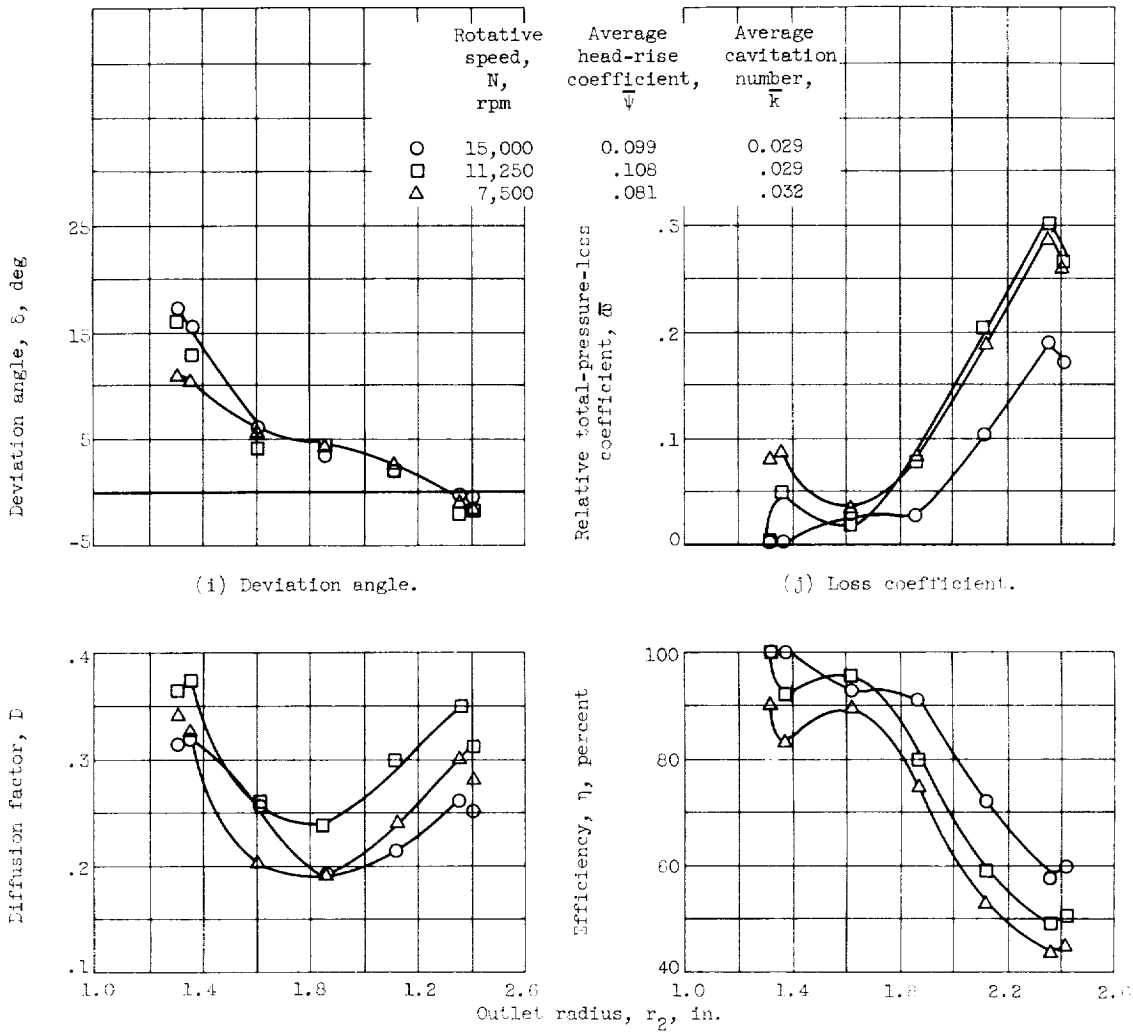

(i) Deviation angle.

(j) Loss coefficient.

(k) Diffusion factor.

(l) Efficiency.

Figure 22. - Concluded. Effect of rotor blade speed on blade-element performance. Average flow coefficient, 0.086; normalized net positive suction head, 60 feet.

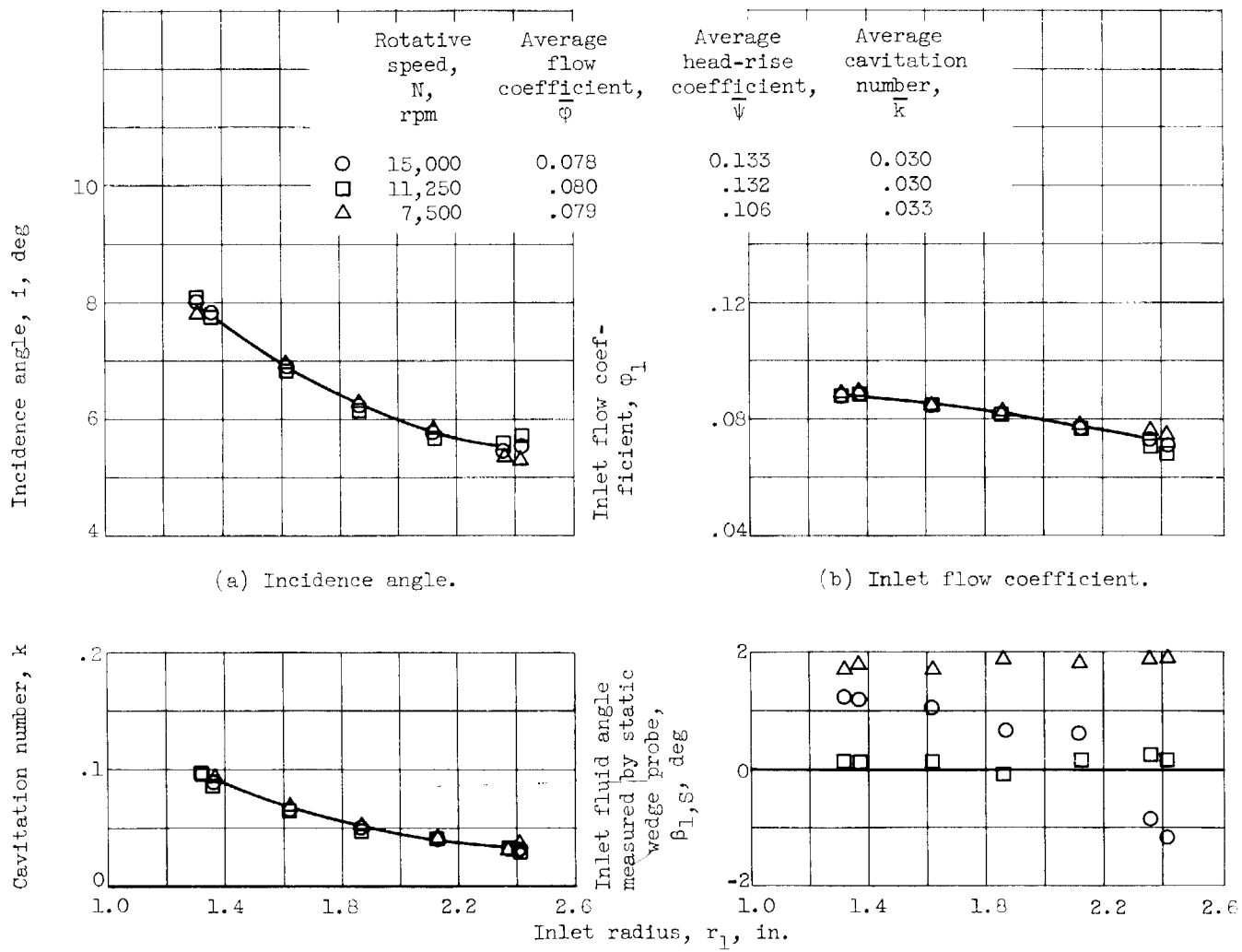

(a) Incidence angle.

(b) Inlet flow coefficient.

(c) Cavitation number.

(d) Inlet flow angle.

Figure 23. - Effect of rotor speed on blade-element performance. Average flow coefficient, 0.080; normalized net positive suction head, 60 feet.

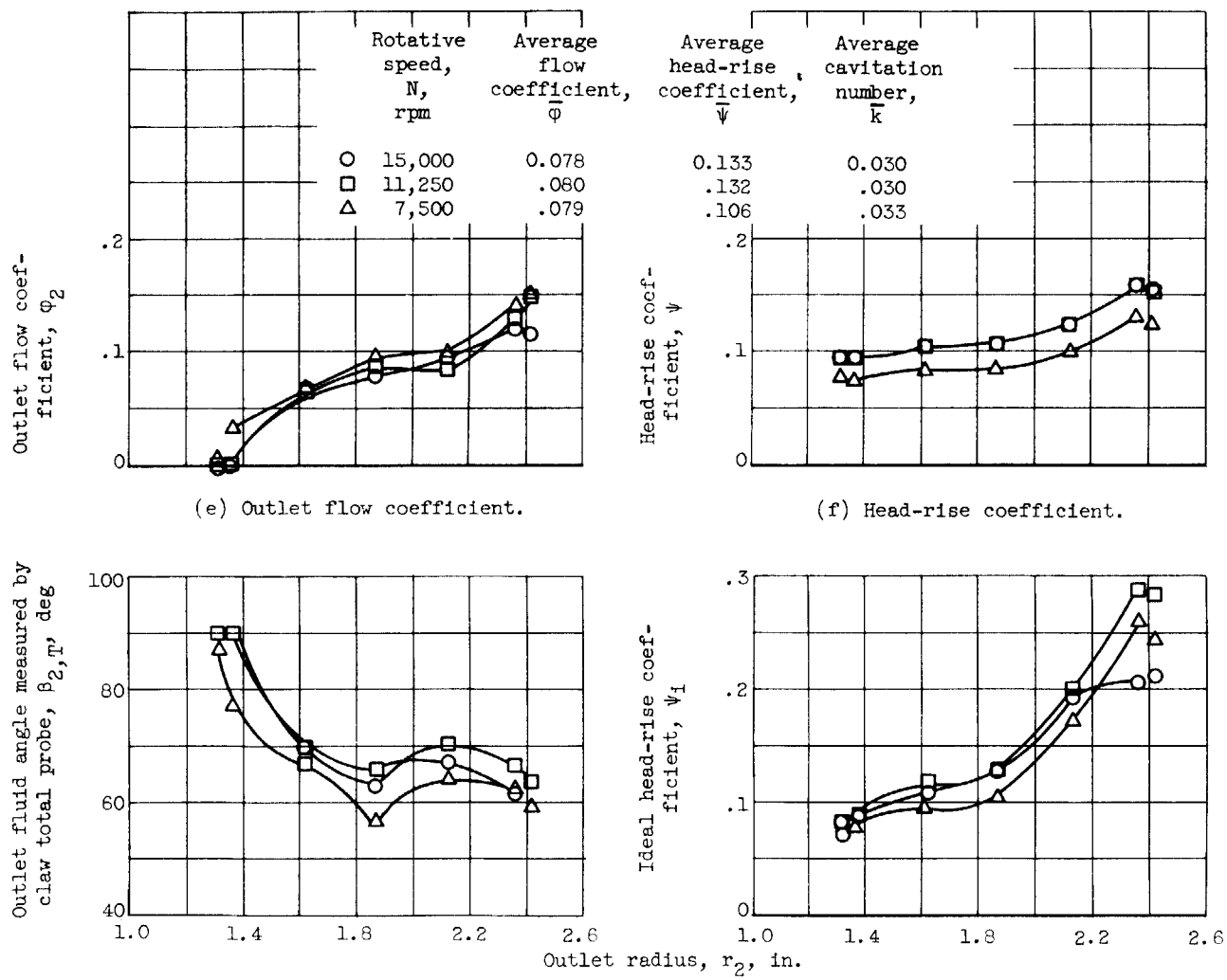

(e) Outlet flow coefficient.

(f) Head-rise coefficient.

(g) Outlet flow angle.

(h) Ideal head-rise coefficient.

Figure 23. - Continued. Effect of rotor speed on blade-element performance. Average flow coefficient, 0.080; normalized net positive suction head, 60 feet.

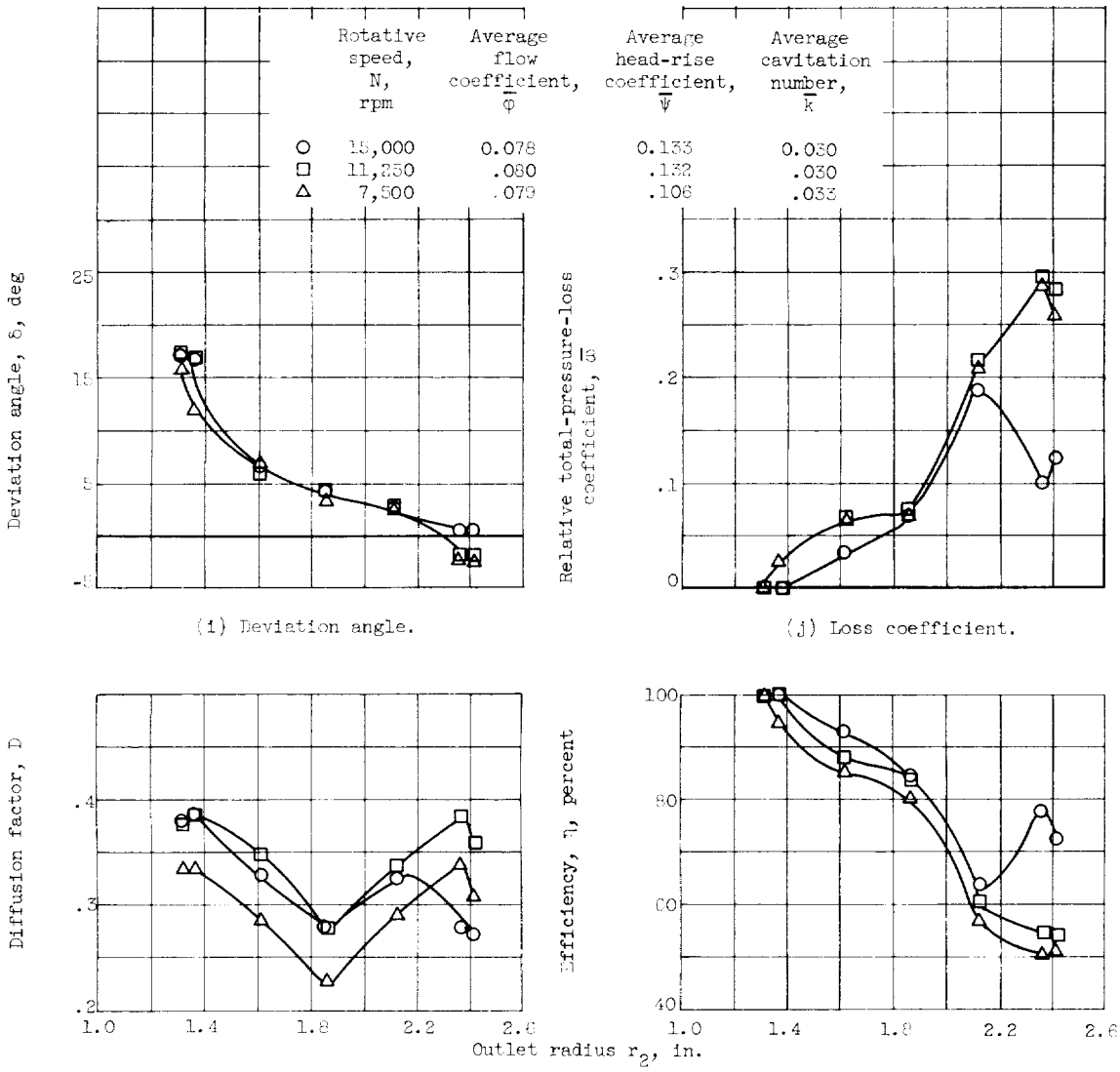

(i) Deviation angle.

(j) Loss coefficient.

(k) Diffusion factor.

(l) Efficiency.

Figure 23. - Concluded. Effect of rotor speed on blade-element performance. Average flow coefficient, 0.080; normalized net positive suction head, 60 feet.

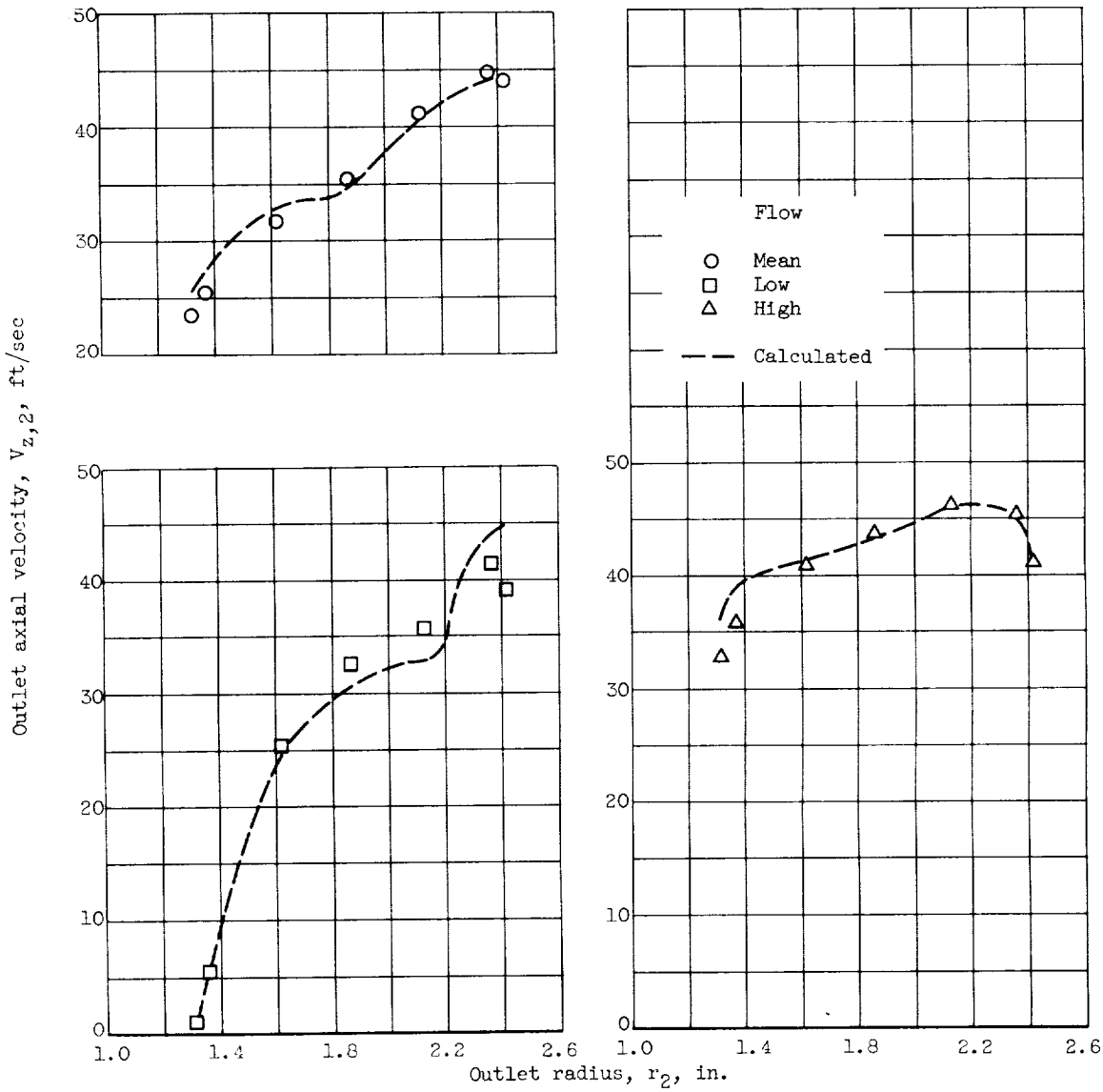

(a) Rotative speed, 15,000 rpm; normalized net positive suction head, 160 feet.

Figure 24. - Comparison between radial distributions of axial velocity as measured and as calculated by means of simple radial equilibrium expression.

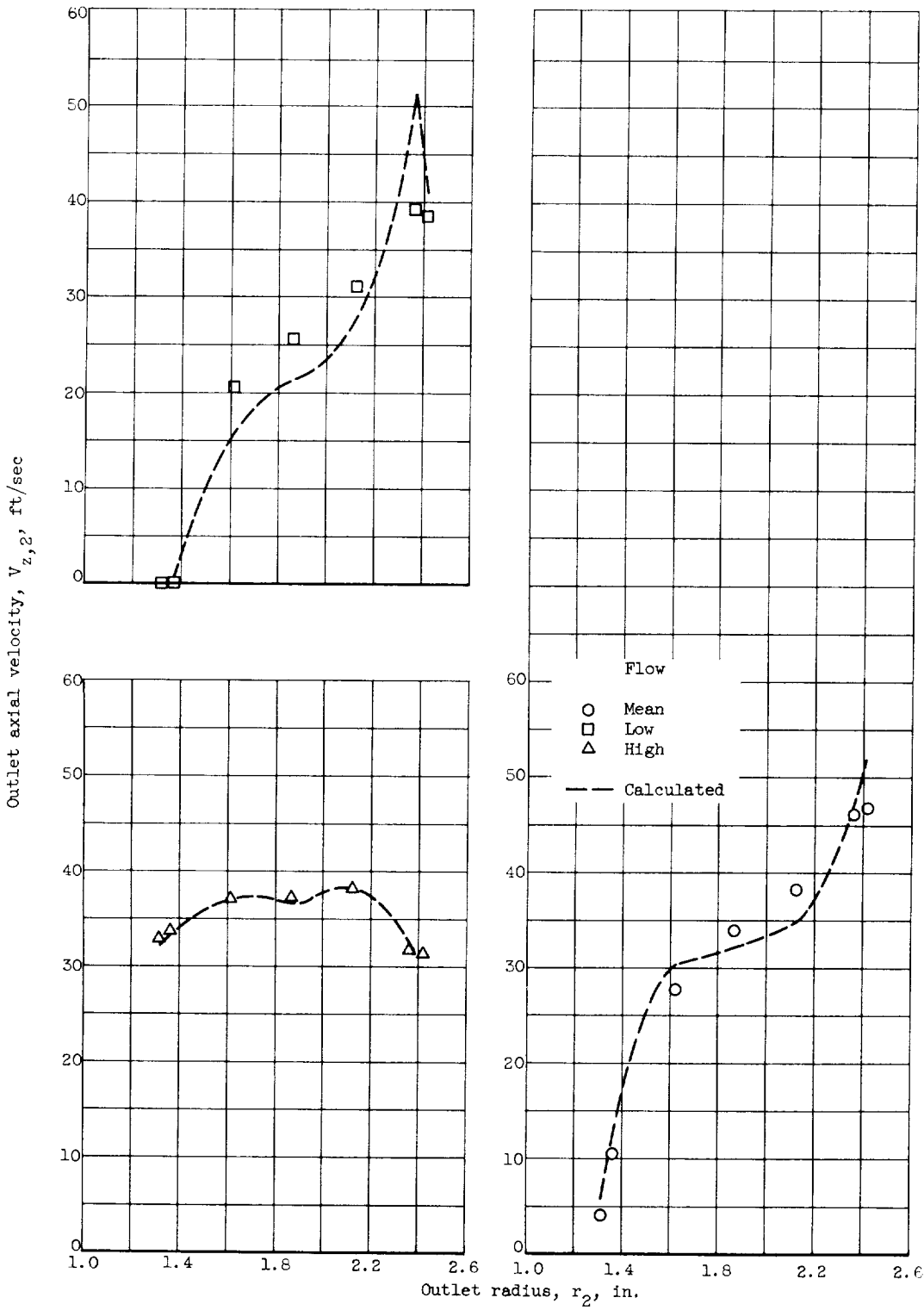

(b) Rotative speed, 15,000 rpm; normalized net positive suction head, 60 feet.

Figure 24. - Continued. Comparison between radial distributions of axial velocity as measured and as calculated by means of simple radial equilibrium expression.

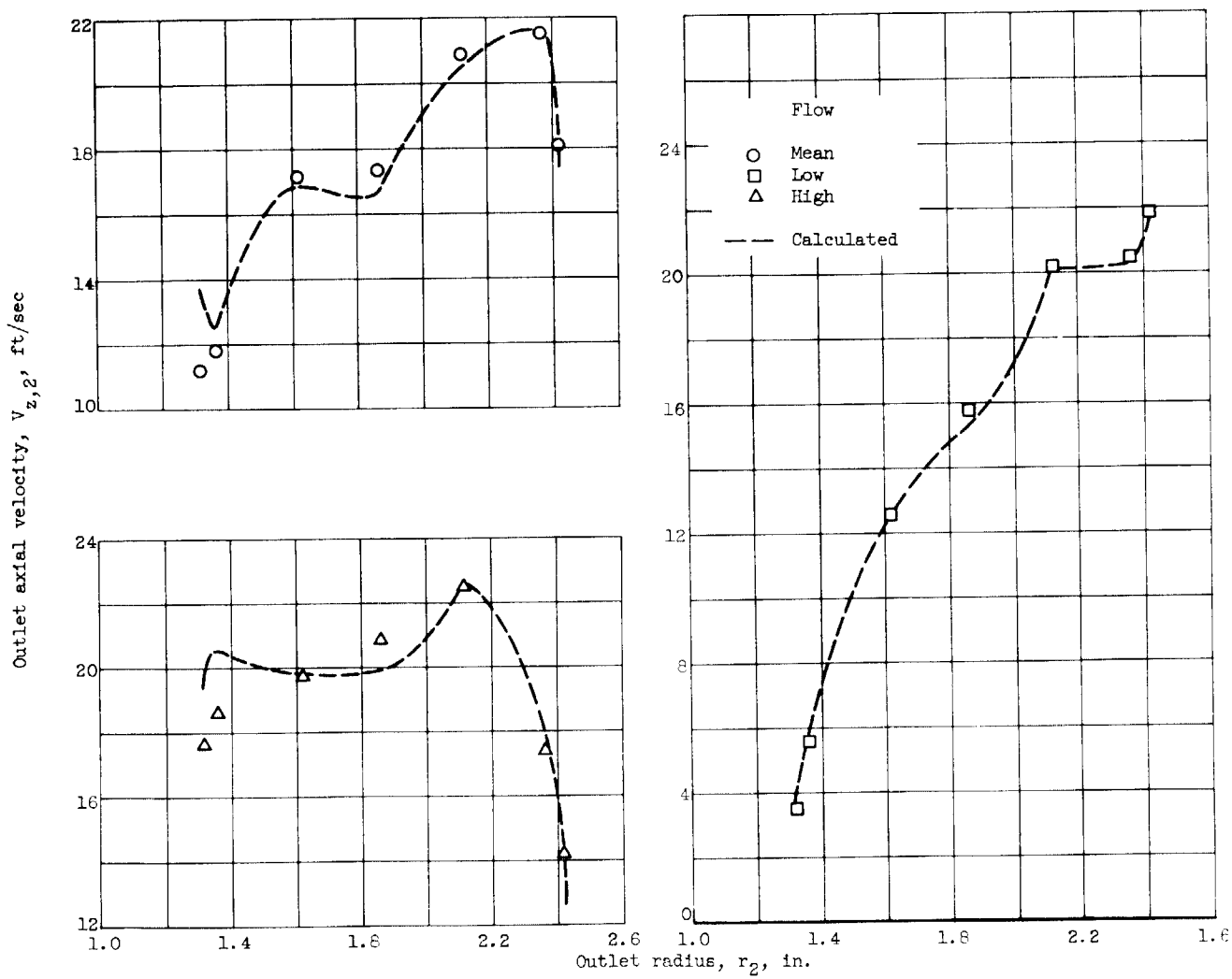

(c) Rotative speed, 7500 rpm; normalized net positive suction heat, 160 feet.

Figure 24. - Continued. Comparison between radial distributions of axial velocity as measured and as calculated by means of simple radial equilibrium expression.

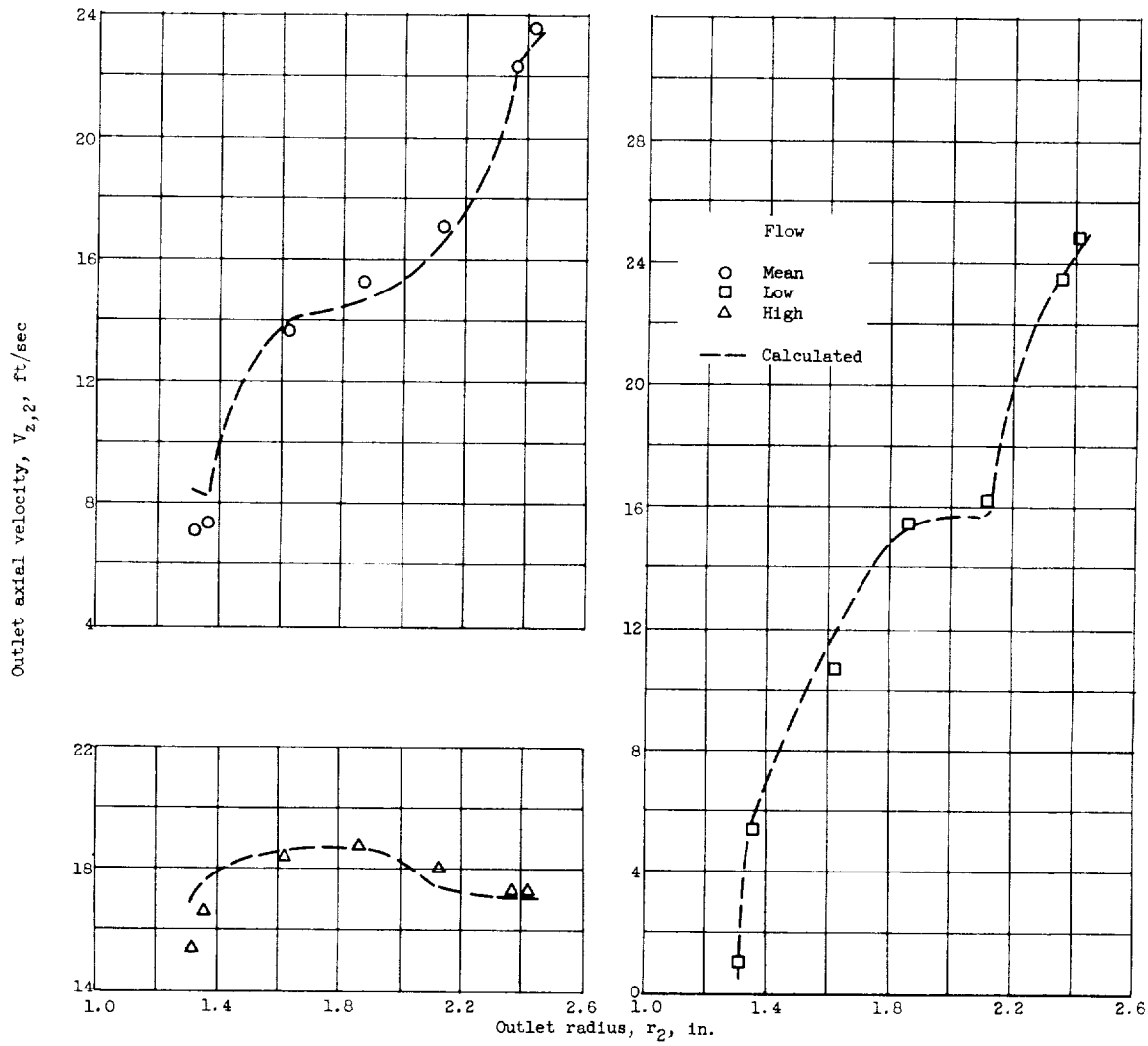

(d) Rotative speed, 7500 rpm; normalized net positive suction head, 60 feet.

Figure 24. - Concluded. Comparison between radial distributions of axial velocity as measured and as calculated by means of simple radial equilibrium expression.

NASA-Langley, 1962 E-1489